Laser-Activated Nanomaterials

for Tissue Repair

by

Russell Ricks Urie

A Dissertation Presented in Partial Fulfillment
of the Requirements for the Degree
Doctor of Philosophy

Approved October 2019 by the
Graduate Supervisory Committee:

Kaushal Rege, Chair
Abhinav Acharya
Dale DeNardo
Julianne Holloway
Mary Laura Lind Thomas

ARIZONA STATE UNIVERSITY

December 2019

ABSTRACT

Tissue approximation and repair have been performed with sutures and staples for centuries, but these means are inherently traumatic. Tissue repair using laser-responsive nanomaterials can lead to rapid tissue sealing and repair and is an attractive alternative to existing clinical methods. Laser tissue welding is a sutureless technique for sealing incised or wounded tissue, where chromophores convert laser light to heat to induce in tissue sealing. Introducing chromophores that absorb near-infrared light creates differential laser absorption and allows for laser wavelengths that minimizes tissue damage.

In this work, plasmonic nanocomposites have been synthesized and used in laser tissue welding for ruptured porcine intestine *ex vivo* and incised murine skin *in vivo*. These laser-responsive nanocomposites improved tissue strength and healing, respectively. Additionally, a spatiotemporal model has been developed for laser tissue welding of porcine and mouse cadaver intestine sections using near-infrared laser irradiation. This mathematical model can be employed to identify optimal conditions for minimizing healthy cell death while still achieving a strong seal of the ruptured tissue using laser welding. Finally, in a model of surgical site infection, laser-responsive nanomaterials were shown to be efficacious in inhibiting bacterial growth. By incorporating an anti-microbial functionality to laser-responsive nanocomposites, these materials will serve as a treatment modality in sealing tissue, healing tissue, and protecting tissue in surgery.

i

DEDICATION

I would like to dedicate this work to my wife Jade and daughter Maude, who have remained consummately supportive and patient of me through the highs and lows of research.

ACKNOWLEDGMENTS

TABLE OF CONTENTS

LIST OF FIGURES

INTRODUCTION TO INORGANIC NANOMATERIALS IN MEDICINE AND LASER TISSUE REPAIR

Tissue Repair and Current Treatment Methods

Soft tissue repair has undergone dramatic changes in the past century. Gauzes, sutures, staples, hemostats, and wound dressings have progressed from animal- or plant-derived products to synthetic materials that elicit less inflammation and can, in some cases, be absorbed by the body(Dennis et al., 2016). In tissue and organ repair, however, functionality can be lost at length scales of 150 μm or less. Conventional repair demonstrates suboptimal performance in recovery of tissue functionality at even moderate surgical length scales.

Inorganic nanomaterials have the potential to overcome limitations of conventional materials in soft tissue repair, leading to novel treatment modalities. Conventional tissue repair involves removal of damaged tissue and a material fill or mechanically approximate tissue discontinuity(Annabi et al., 2014). Recent approaches using inorganic nanomaterials aim to actively promote or stimulate repair and regeneration. Potential advantages of inorganic nanoparticles in tissue repair include ease of application, consistency, versatility, speed, effectiveness, functionality, minimal invasiveness, and viable alternatives for difficult-to-obtain grafts and transplantations that may elicit significant inflammation(Annabi et al., 2014; Fleischer & Dvir, 2013). I specifically highlight recent advances in tissue adhesives, surgical sealants, alternatives to sutures and staples, hemostats, wound dressings, stem cell targeting, and tissue engineering scaffolds, focusing on preclinical findings in animal models.

tissue repair phases. Tissue repair is a highly-orchestrated interplay of hemostasis, inflammation, and cell migration and proliferation, resulting in wound contraction and remodeling(Rittie, 2016) (Figure 1) in response to injury. Skin repair is perhaps the best-understood model of tissue repair and is discussed briefly here as a model.

Hemostasis involves a cascade of soluble mediators, parenchymal cell migration, and extracellular matrix (ECM) formation(Gurtner, Werner, Barrandon, & Longaker, 2008). A provisional ECM provides for further cell migration(Akbik, Ghadiri, Chrzanowski, & Rohanizadeh, 2014; Rittie, 2016) and healing via vasoconstriction, platelet aggregation, and fibrin deposition(Rittie, 2016).
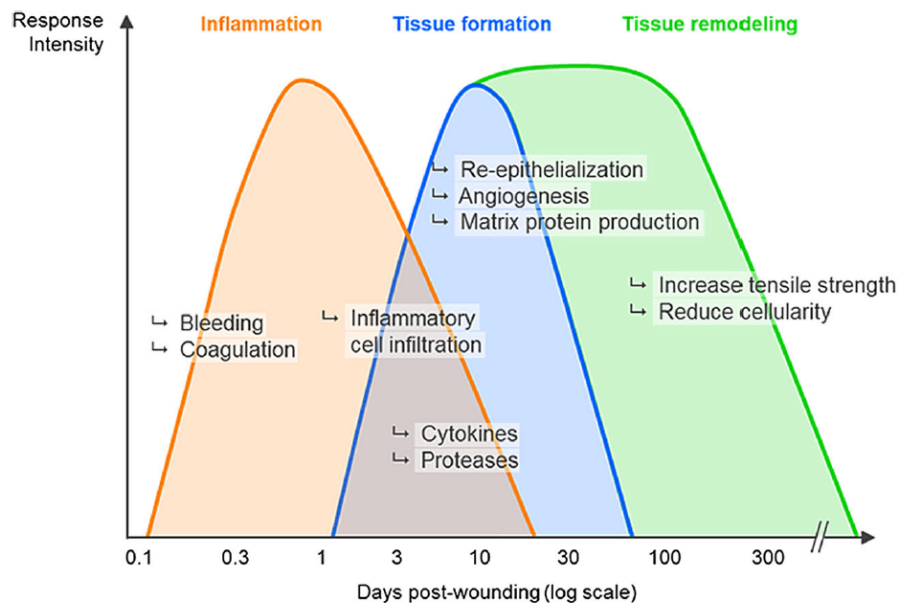
Figure 1. Representation of the phases of wound healing. Modified with permission(Rittie, 2016).

Inflammation facilitates the recruitment of phagocytic neutrophils and macrophages, monocytes, and lymphocytes(Zaja-Milatovic & Richmond, 2008) at the wound(Akbik et al., 2014; Enoch, Grey, & Harding, 2006) through increased capillary permeability(M. S. Hu et al., 2014; Rittie, 2016). Delayed inflammation can occur due to

absence or deficiency of these cells. Prolonged activation of the immune cells results in dysfunction, fibrosis, and scarring.

Proliferation is defined by keratinocyte migration, angiogenesis, reepithelialization, fibroplasia(Zaja-Milatovic & Richmond, 2008), and synthesis of ECM collagen(Akbik et al., 2014; Rittie, 2016). New blood vessels facilitate keratinocyte migration(Gurtner et al., 2008). Fibroblasts and macrophages replace the clotted fibrin matrix with granulation tissue and ECM components(Rittie, 2016). Growth factors modulate keratinocyte migration and endothelial cell proliferation, and angiogenesis(Gurtner et al., 2008; Rittie, 2016).

Wound contraction begins after reepithelialization, lasting until 2 weeks postinjury(Rittie, 2016). Fibroblasts transform to a myofibroblast phenotype, with strong contractile force(Rittie, 2016), and replace the provisional ECM with tissue similar to the native tissue. This phase can last over a year(Gurtner et al., 2008). Endothelial cells, macrophages, and myofibroblasts are removed by apoptosis(Gurtner et al., 2008). Through secretion of matrix metalloproteinases by fibroblasts, macrophages, and neutrophils, type I collagen replaces type III collagen(Rittie, 2016). Collagen fibers are realigned along tension lines and accumulate(Gurtner et al., 2008; Rittie, 2016), creating scar tissue(Reinke & Sorg, 2012). Unresolved injury sites demonstrate excess scarring due to the delay of the remodeling phase.

These phases depend on the unique conditions of each injury, and vary by tissue type and the extent and kind of injury(M. S. Hu et al., 2014). Some soft tissue types have limited regenerative capacity. A paradigm shift that streamlines the modulation of these

processes for therapeutic benefit rather than attempting to avoid them may serve to enhance the efficacy of tissue repair.

primary intention tissue repair in the clinic and limitations. Tissue discontinuities are healed by means of primary, secondary, or tertiary intention. Primary intention mechanically approximates tissue edges, for injuries with disruption in tissue continuity but minimal tissue loss or necrosis. Secondary intention heals injuries in which tissue edges cannot be joined mechanically due to tissue loss or limiting geometry. Secondary intention promotes granulation tissue to fill negative space from the injury or debridement of necrotic tissue. Tertiary intention, often referred to as delayed primary intention, intentionally leaves injuries open for subsequent approximation. Laser tissue welding is largely intended for primary intention, and thus secondary and tertiary intention will not be discussed.

Precise disruption of soft tissues with minimal damage to surrounding tissue and the basal membrane is observed in cases of surgical incisions, anastomoses, and ligations. In incisions, repair method depends on site accessibility(Armitage & Lockwood, 2011), but generally occurs via primary intention. Tissue approximation is conventionally accomplished by sutures, staples, adhesives, and/or sealants(Coulthard et al., 2010) to reduce infection and facilitate satisfactory cosmesis(Cirocchi et al., 2014).

Sutures have been used for thousands of years to close wounds and surgical incisions, with documented use as early as ancient Egypt and India. Synthetic sutures are the most common means of approximation(Armitage & Lockwood, 2011) because of the inflammatory response to biologically-derived materials(Armitage & Lockwood, 2011; Cirocchi et al., 2014; Lloyd, Marque, & Kacprowicz, 2007). Absorbable sutures must

retain mechanical strength and yet be resorbed as tissue heals(Armitage & Lockwood, 2011). Suture breakdown occurs through enzymatic degradation or hydrolysis for natural or synthetic sutures, respectively(Armitage & Lockwood, 2011). Nonabsorbable sutures retain mechanical integrity for more than 6 months(Lloyd et al., 2007) and are eventually encapsulated by fibroblasts(Armitage & Lockwood, 2011). Despite their extensive use and simplicity, sutures have a number of limitations, including wound dehiscence after surgery(Cirocchi et al., 2014). Monofilament sutures have memory, limiting surgeon dexterity, while braided sutures are susceptible to bacterial colonization(Armitage & Lockwood, 2011). Nonabsorbable sutures have high stress concentration, leading to granuloma formation after extended residence in the body. Suturing is not feasible in many surgeries. Fluid leakage (blood, bowel content, bile, cerebrospinal fluid, etc.) across the suture line causes complications such as failure followed by intra-abdominal abscesses, fistula, peritonitis, and mortality(Bouten et al., 2014; Lloyd et al., 2007).

Absorbable and nonabsorbable staples(Cirocchi et al., 2014) are also widely used for wound closure(Lloyd et al., 2007). Nonabsorbable stainless steel staples demonstrate high tensile strength(Tajirian & Goldberg, 2010a), while absorbable poly(lactic-*co*-glycolic acid) staples are resorbed completely in months(Tajirian & Goldberg, 2010a). Clinical studies show no significant difference in cosmetic appearance, mechanical strength, complications and infection, dehiscence, or inflammation among stapled or sutured wounds(Krishnan, MacNeil, & Malvankar-Mehta, 2016; Slade Shantz, Vernon, Morshed, Leiter, & Stranges, 2013). Staple removal can be more painful than suture removal(Krishnan et al., 2016; Lloyd et al., 2007). However, for a number of procedures,

including anastomoses, staples are the faster method compared with sutures(Coolman, Ehrhart, Pijanowski, Ehrhart, & Coolman, 2000).

Adhesive tapes can be used for wounds with well-approximated margins. They can be relatively inexpensive and are easy to apply and remove, with minimal reactivity(Tajirian & Goldberg, 2010a). Their clinical use is limited to superficial wounds that are not under tension(Lloyd et al., 2007; Tajirian & Goldberg, 2010a).

Adhesive sealants can be applied easily and with little pain(Coulthard et al., 2010; Lloyd et al., 2007). Cyanoacrylate glues are common but limited to surface wounds because of the toxic degradation products of some formulations(Singer, Quinn, & Hollander, 2008). Poly(ethylene glycol) (PEG)-based adhesives find limited use because of low mechanical strength and high swelling(Schnueriger et al., 2011). Natural adhesives (e.g., fibrin glue) also face significant drawbacks, including low mechanical strength, stiffness, low adhesion(Annabi, Yue, Tamayol, & Khademhosseini, 2015) and/or high immunogenicity(Bouten et al., 2014). Although commercial adhesives are available, many do not meet the demands of the dynamic tissue repair environment(Annabi et al., 2015; Bouten et al., 2014).

Despite the nearly ubiquitous use of sutures, suturing holds numerous shortcomings. The tissue is handled extensively during suturing, and fluid and bacterial leakage can occur across sutured tissue during the initial period of healing(Cilesiz, 1999; Schalow & Kirsch, 2003). Surgical staples and clamps have been investigated for overcoming some of the limitations of suturing; yet, sutures, clips, and staples cannot safely repair or functionally rehabilitate many tissue types(Lauto, Mawad, & Foster, 2008a), including gastrointestinal (GI) tract(Pecha et al., 1998), nerves(Millesi, 1981), dura repair

in spinal surgery(Hida et al., 2006), urethroplasties(Cimador, Castagnetti, & Milazzo, 2004), laparoscopic mesh fixation in hernia repair(Chelala et al., 2007), lung(K. Murray & Ho, 2002), vasculature(Lumsden & Heyman, 2006), cataract surgery(Garcia et al., 2009a), traumatic injuries(Sheffy, Mintz, Rivkind, & Shapira, 2006), lens capsule bag(Ratto et al., 2009a; Francesca Rossi et al., 2011), and others(Thomsen, 1991). Additionally, their use is not advised in a number of friable tissue types(Lauto, Mawad, & Foster, 2008b).

These foreign materials may be permanent, removable, or absorbable but often elicit an inflammatory response and scar formation. Tissue repair using these materials is often skill-intensive and invasive. Inorganic nanomaterials are being evaluated to overcome these limitations to improve or replace current treatment modalities and offer solutions where no modalities exist.

Inorganic Nanomaterials

Nanoscale particles (1–100 nm) demonstrate properties that are not observed at the macroscopic scale(Farrell, Ptak, Panaro, & Grodzinski, 2011; Morigi et al., 2012). Metal-based, carbon allotrope, or ceramic nanoparticles (NPs) are commonly used in biomedical applications. Metal/metal oxide–based NPs include those based on gold, silver, zinc, magnesium, iron, and titanium. Carbon allotrope NPs include graphene nanosheets and carbon nanotubes (CNTs). Ceramic NPs include clay, silica, calcium, and bioglass NPs. Inorganic NPs demonstrate a diversity of tunable properties, which make them attractive for tissue repair applications(Kojima, Aubel, & Fussenegger, 2015; Koutsopoulos, 2012).

Silver NPs are widely used for their antimicrobial properties in implant devices, food packaging materials, topical creams and ointments, and other applications. Gold NPs can be easily tuned to various sizes and shapes, including spheres, rods, cages, and shells;

are easy to modify; and demonstrate size-dependent optical properties(Kharlamov & Gabinsky, 2012). For these reasons, gold NPs have been widely studied in drug delivery and tumor thermal ablation, including in clinical trials for cancer (see https://clinicaltrials.gov/show/NCT02761525 NLM). Iron oxide NP formulations, including Venofer[®], Ferrlecit[®], INFed[®], Dexferrum[®] and Feraheme[®], have been approved by the US Food and Drug Administration (FDA) for treating anemia related to chronic kidney disease(Patent No. US Patent WO 2010034219 A1, 2010; Thiesen & Jordan, 2008). Additionally, ferumoxytol (i.e., Feraheme[®]) is being investigated in imaging(Bashir, Bhatti, Marin, & Nelson, 2015) (clinicaltrials.gov/show/NCT01663090), but similar superparamagnetic iron oxide NPs have been discontinued(Y.-X. J. Wang, 2015).

Graphene oxide nanosheets are single layers of graphite in a hexagonal lattice(Novoselov et al., 2004). Graphene oxide nanosheets have high surface area and adsorption capacity and demonstrate optical, electronic, and quantum properties(Mattei & Rehman, 2014), including absorption of UV and near-infrared light. Graphene has been investigated for cell culture applications(Sahni et al., 2013), including stem cell differentiation(Menaa, Abdelghani, & Menaa, 2015). CNTs can be regarded as sheets of graphene rolled into a cylinder, in either single-walled or multiwalled configurations, and are often capped at least one end by fullerene(Hopley, Salmasi, Kalaskar, & Seifalian, 2014). CNTs are among the strongest and stiffest materials known. CNTs exhibit structural similarities to collagen fibers(Voge & Stegemann, 2011) and influence cell adhesion, proliferation, and differentiation(Ross, Jiang, Bastmeyer, & Lahann, 2012).

Silica nanomaterials have also been used extensively in bone and dental engineering(S. Wang et al., 2014). Clay NPs are layered sheets of silicate and have

extremely high surface areas. Common clay NPs include laponite, montmorillonite, sepiolite, and hectorite(Ghadiri, Chrzanowski, & Rohanizadeh, 2015). Other inorganic NPs, including those derived from aluminum, magnesium, calcium, and zinc, have not found extensive use in soft tissue repair and regeneration, although many are similar to those of the NPs listed above(Dewi, Ana, Wolke, & Jansen, 2015; Shen et al., 2015; Zeng, Dietzel, Witte, Hort, & Blawert, 2008).

Despite these interesting properties, inorganic NPs often are not directly employed in tissue repair and regeneration because of a number of limitations. Solid NP powders or dispersions can be brittle and unsuitable for load-bearing soft tissues. Additionally, although some dissociation products can be beneficial, they can elicit strong inflammatory responses when released in high concentrations. The reader is directed to a number of reviews discussing NP toxicity in greater detail(R. Liu et al., 2015; Matusiewicz, 2014; Sharifi et al., 2012; Soenen et al., 2011). More commonly, inorganic nanomaterials used in tissue repair typically interface these NPs and their hybrids with synthetic and/or biological materials, including hydrogel-based materials(Butcher, Offeddu, & Oyen, 2014; Utech & Boccaccini, 2016), electrospun matrices(Braghirolli, Steffens, & Pranke, 2014), and viscous gels(Rose et al., 2014a), among others.

Incorporation of NPs imparts different functionalities to the resulting nanomaterials (Figure 2). First, NPs' stimulus-responsive properties allow for modulation of real-time analysis of material integration, degradation, and fate(Shevach, Maoz, Feiner, Shapira, & Dvir, 2013). Stimulus responsiveness can be an inherent property of NPs, and inorganic NPs can respond to a variety of external stimuli including pH, light, magnetism, and ultrasound. For example, the inherent plasmonic properties of gold nanostructures make

them responsive to visible and NIR light. NPs can also be made stimuli-responsive through functionalization with moieties that respond to pH, redox changes, and/or temperature. Second, NPs embedded within a matrix enhance the integrity of the resulting nanomaterial. In particular, material strength and degradation behavior can be tuned by NP fillers or linkers(Utech & Boccaccini, 2016). Third, the alignment, structure, or surface morphology of NPs can be modulated for specific applications. Fourth, inorganic NPs can facilitate increased loading of drugs, genes, growth factors, and/or biologically active species, because of the high surface area–to–volume ratio at the nanoscale(D. Guo, Xie, & Luo, 2014; T. Kim & Hyeon, 2014). Release mechanisms and kinetics from these NPs can be tailored through modulation of their size, shape, and surface chemistry. Furthermore, inorganic NPs are often inert and can provide greater stability to loaded therapeutic molecules, enhancing their efficacy. Fifth, NPs increase sites for cell adhesion within a scaffold, creating greater cell migration, proliferation, and differentiation. Inorganic NPs can facilitate high adsorption of proteins, including ECM glycoproteins, which are common sites for cell adhesion. A number of inorganic NPs, including those made from silver, calcium phosphate, and silica, release ions as they disassociate, and these ions may affect cell viability, differentiation, or morphogenesis in unique ways. The following sections highlight key advances in the use of inorganic nanomaterials for tissue repair and regeneration.
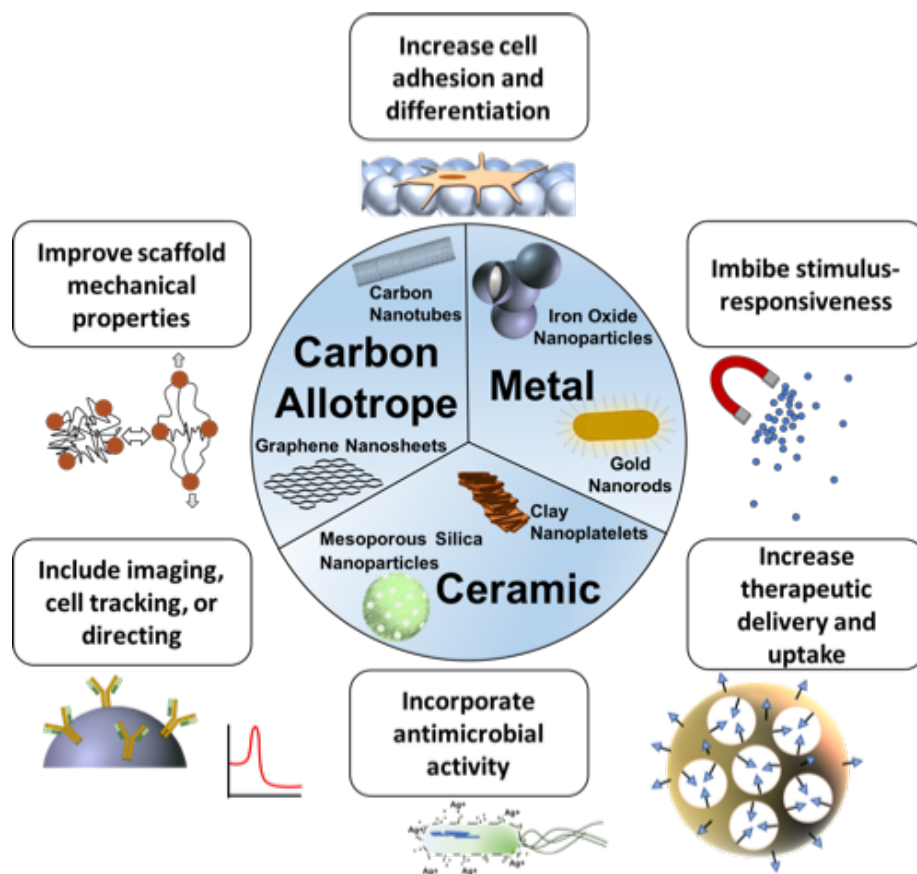
Figure 2. Inorganic nanoparticles and their properties. Inorganic nanoparticles containing carbon allotrope nanoparticles (e.g., carbon nanotubes, graphene oxide nanosheets), metal/metal oxide–based nanoparticles (e.g., superparamagnetic iron oxide nanoparticle, gold nanoparticles), or ceramic nanoparticles (e.g., clay, mesoporous silica nanoparticles) are shown. Incorporation of inorganic nanoparticles into biologically relevant materials can increase cell adhesion and differentiation; impart the material with the ability to respond to external stimuli; increase the delivery or cellular uptake of molecular therapeutics; add antimicrobial activity to the material; facilitate the imaging, tracking, or directed proliferation of cells; and improve the mechanical properties or degradation characteristics of the nanomaterial.

Inorganic Nanomaterials in Tissue Repair

tissue adhesives and sealants. Polymer-based adhesives are the most employed adhesives for approximating tissue; they typically rely on chemical reactions, pH changes, thermal modulation, or photopolymerization(Annabi et al., 2014). NPs within a polymer matrix increase adhesive strength, stiffness, or strength. Chitosan-based nanocomposite adhesives in which gold NPs were generated in situ(Sun et al., 2014) exhibited a 3.5-fold increase in adhesive strength compared with their pristine chitosan counterpart. The NPs' size and concentration could be adjusted to tune the viscosity of the nanocomposite adhesives. The incorporation of 2% laponite in four-armed PEG modified with dopamine resulted in significantly lower cure times, increased adhesion, and unchanged cytocompatibility(Y. Liu et al., 2014). Subcutaneous implantation of these nanocomposites increased cell infiltration, likely due to the increased number of cell adhesion sites and interrupted polymer network that may occur from laponite inclusion. It is likely that NPs provide an alternative to cell-binding proteins, resulting in increased adhesive bioactivity. A strategy that does not involve the approximation of tissues using NP dispersions has also been demonstrated (Figure 3). In this approach, a few drops of a colloidal dispersion of silica NPs were placed between two rectangular ribbons of calf liver(Rose et al., 2014a). The pieces were then gently pressed together for 30 s, causing adhesion of the tissue. This study demonstrated that NP-based adhesives may not need common polymer-based mechanisms for tissue adhesion in some applications.
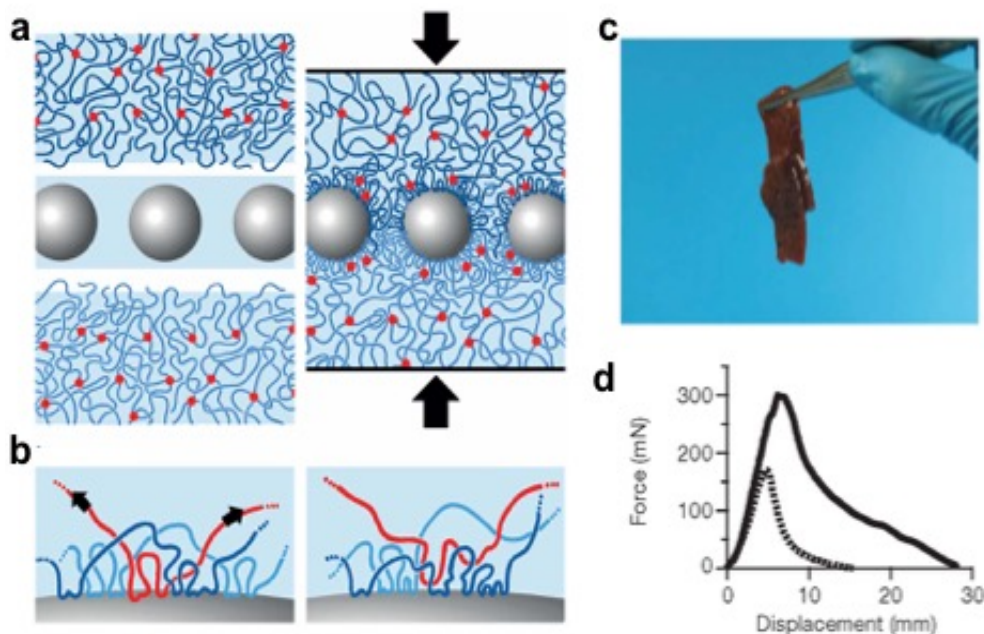
Figure 3. Nanoparticle-based tissue adhesive. (*a,b*) Schematic representation of the mechanism of nanoparticles anchoring two polymer networks (e.g., in tissues) together. The black arrows indicate the pressure applied to squeeze the gel layers together. (*c*) Two rectangular sections of calf liver glued together by spreading a nanoparticle dispersion between them and pressing them together for 30 s. (*d*) Normalized force–displacement relationship for the lap joints of two sets of calf liver glued by spreading TM-50 silica solution between them and then pressing ribbons with a finger for 30 s. Modified with permission(Rose et al., 2014a).

Laser-activated sealing (also known as laser tissue welding) is a sutureless approach in which chromophores, including plasmonic NPs (e.g., gold), are irradiated with external light. Irradiation with NIR light results in a photothermal response due to the presence of chromophores in these sealants. The resulting elevated local temperature can reconfigure tissue proteins and help interdigitize the exogenous nanomaterial with the tissue. Different photothermal solders, including proteins, can be interfaced with small-molecule and NP

13

chromophores to seal ruptured tissues. I developed laser-responsive elastin-like polypeptide-(H.-C. Huang, Walker, Nanda, & Rege, 2013a) and collagen(Urie, Quraishi, Jaffe, & Rege, 2015a) gold nanorod (GNR) nanomaterials tuned to a maximum absorbance wavelength of ~800 nm. I demonstrated the laser-activated sealing of porcine intestine *ex vivo* leading to prevention of fluid and bacterial leakage, which indicated a promising sutureless technique for sealing ruptured tissue. A more detailed description of laser tissue sealing will be given later in this chapter.

infection control and wound dressings. Antibacterial NPs can improve clinical outcomes in tissue repair. Generally, approaches rely on the production of metal ions and/or reactive oxygen species. Silver, including silver NPs(Prabhu & Poulose, 2012), has well-known antimicrobial properties. Various formulations of silver nanomaterials, including Acticoat® (Smith & Nephew, Inc.) wound dressing and SilvaGard® (AcryMed, Inc.), have been approved by the FDA(Hayman, 2009). The mechanism of bacterial inhibition for silver NPs is not completely understood, but the most accepted mechanism is that Ag^+ ions bind strongly to thiol groups in cell surface proteins in bacteria, breaking down the cell membrane and subsequently ATP synthesis(Duran et al., 2010; Hajipour et al., 2012). Silver NPs are therefore being investigated extensively for use in coatings for catheters and implantable devices (clinicaltrials.gov/show/NCT01950546, clinicaltrials.gov/show/NCT01975545, and clinicaltrials.gov/show/NCT02400957), and several clinical trials for topical or wound dressing applications are in progress (clinicaltrials.gov/show/NCT02761525, clinicaltrials.gov/show/NCT01243320, clinicaltrials.gov/show/NCT01405794, and clinicaltrials.gov/show/NCT00659204).

One concern with tissue adhesives is that although they are intended to create a barrier to bacteria, they may actually trap bacteria already contained at the site of closure. To address this issue, 2-octyl cyanoacrylate adhesive (DERMABOND®, Ethicon US, LLC) was doped with silver NPs. Bacterial growth was reduced by an order of magnitude; tensile breaking strength and adhesive strength were significantly increased in excised porcine sclera(Yee, Seluaduray, & Hawkins, 2016). The biocompatibility of polyethylene terephthalate meshes, which are widely used in hernia repair, was improved via conjugation with 20-nm gold NPs(Whelove et al., 2011). These nanocomposite scaffolds enhanced the cellularity of L929 fibroblasts and repelled *Pseudomonas aeruginosa* bacteria at the surface compared with conventional polyethylene terephthalate meshes. Additionally, low concentrations of gold led to lower production of reactive oxygen species in L929 cells compared with cells exposed to pristine polyethylene terephthalate. Commercial poly(glycolic acid) sutures were coated with silver NPs and compared with antibacterial-coated sutures in a mouse intestinal anastomosis model(S. Zhang, Liu, Wang, Peng, & Wong, 2014). Three days following the procedure, immunohistochemistry showed significantly lower macrophage and neutrophil infiltration as well as greater collagen deposition at the anastomotic site for the silver NP–coated sutures compared with both the antibacterial-coated sutures and the sutures alone. Additionally, mechanical testing of the tissue showed a greater return in strength with the silver NP–coated sutures than with the other treatments. Incorporation of silver NPs reduced the inflammatory response and improved the quality of healing.

wound and burn dressings. Inorganic nanomaterials have also been investigated as potential interventions in cases of chronic wounds and burns. Silver chloride NPs (42

nm), stabilized by chitosan oligomers, were formulated as an ointment and used for the treatment of second-degree burn wounds in rats(Kang et al., 2016). Compared with untreated burns and those treated by vasoline or chitosan ointments, the chitosan–silver chloride NP ointment yielded the highest percent of survival and greater regenerated collagen density. Regenerated cellulose–nanosilver composite sponges were investigated in full-thickness cutaneous wounds infected with *Staphylococcus aureus* in rabbits(Ye et al., 2016). The infection was combated and wound closure occurred much more rapidly than with gauze or no treatment (Figure 4). In another study, silver NPs were embedded within a chitosan scaffold, and stearic acid was applied to one surface of the scaffolds to improve the wetting on the surface in contact with the wound(Liang, Lu, Yang, Gao, & Chen, 2016). In a partial-thickness skin wound model, mice were treated with chitosan– nanosilver scaffolds, chitosan scaffolds, or the commercially available Acasin® Acasin® (AGT Pharm Co. Ltd., Shenzhen) nanosilver gauze on their backs. Complete wound closure was observed on day 8 for the silver nanocomposite and on day 10 for the other materials. Whereas the Acasin® treatment group found levels of silver widely distributed in the blood, liver, spleen, and kidney, the silver nanocomposite group exhibited negligible levels of silver in the liver, spleen, or kidney and only one-fourth as much silver in the blood. Poly(vinyl alcohol) (PVA) hydrogels loaded with chitosan-stabilized silver NPs showed enhanced wound contraction by day 8 with minimal inflammatory response and displayed higher (~49%) reepithelization on the surface and in the wound scar tissue compared with pristine PVA hydrogels (~29%) in full-thickness skin wounds in a rat model(Jaiswal, Koul, & Dinda, 2016).
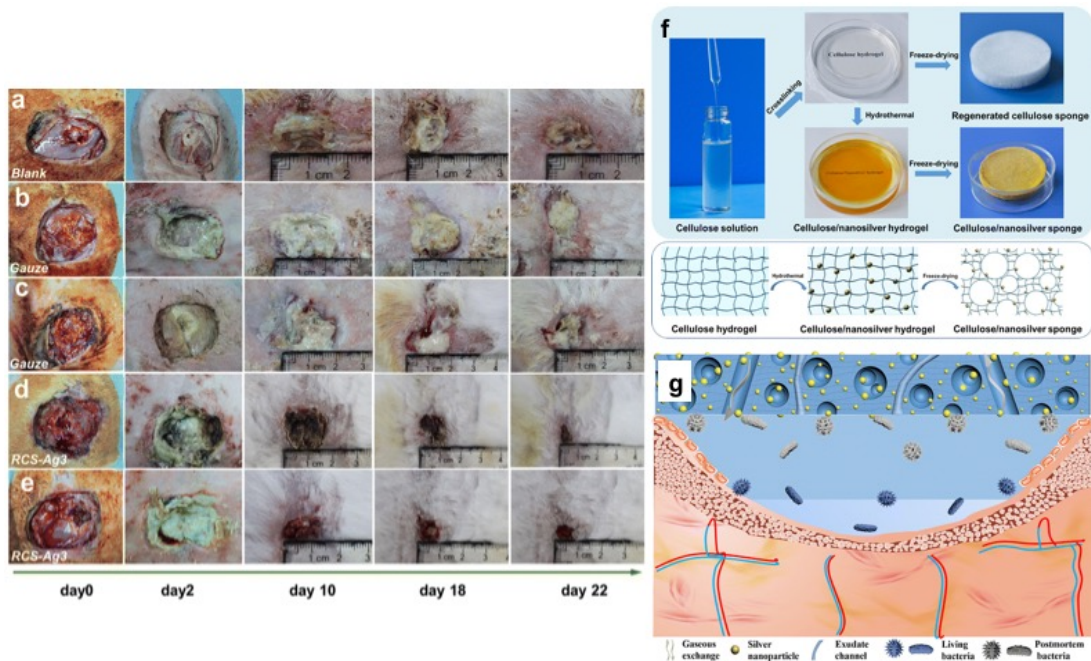
Figure 4. Cellulose–nanosilver composite sponges repair infected wounds. (*a–e*) Images of the healing of infected wounds at specific days for representative rabbits from each treatment group. (*a*) Blank, or untreated, wounds, (*b,c*) wounds treated with sterile gauze, and (*d,e*) wounds treated with regenerated cellulose–silver nanoparticle (RC-Ag3) sponges at 0, 2, 10, 18, and 22 days following wounding and infection. (*f*) Synthesis procedure of RC-Ag3 nanocomposite sponges and schematic representation of sponge architecture. (*g*) Possible mechanism of RC-Ag3 sponges in healing infected wounds. Modified with permission(Ye et al., 2016).

Chitosan wound dressings with hexagonal silver NPs were tested for their ability to assist healing in concert with mild hyperthermia and small-molecule delivery(Levi-Polyachenko, Jacob, Day, & Kuthirummal, 2016, p.). Cell viability of peripheral blood mononuclear immune cells grown on chitosan films increased significantly with hexagonal silver NPs compared with pristine chitosan. These silver nanomaterials were irradiated

with 1,064-nm NIR light, causing a temperature increase of 6.1°C from 37°C to 43.1°C. The result was a 56% increase in fluorescence intensity due to intracellular levels of 20-kDa fluorescein isothiocynate–labeled dextran compared with cells not irradiated with NIR light.

Chitosan–poly(vinyl pyrrolidone)–silver oxide NP films were investigated as wound dressings in open subcutaneous wounds in rats(Archana, Singh, Dutta, & Dutta, 2015). These silver nanocomposite films exhibited greater antimicrobial potential than pristine chitosan films or nanosilver scaffolds. Rats treated with the silver nanocomposites showed nearly complete wound healing on day 14, with improved tissue quality and less scarring than the control groups. Scaffolds of aminosilane-functionalized silver NPs cross-linked with succinylated collagen were compared with succinylated collagen scaffolds for healing an open wound in rats(Mandal, Sekar, Chandrasekaran, Mukherjee, & Sastry, 2015). The silver nanocomposites showed higher cell viability and increased fibroblast proliferation compared with pristine collagen. Complete epithelialization occurred at 16 days with the nanocomposites, 18 days with the collagen scaffolds, and 24 days with the gauze control, with increased levels of collagen, protein, and DNA in the granulation tissue for the nanocomposite-treated group.

Inorganic NPs other than silver have also been investigated in wound dressings, for example, nanoscale zinc oxide–doped electrospun gelatin scaffolds with poly(methyl vinyl ether-alt-maleic anhydride), an FDA-approved bioadhesive. The zinc-doped scaffold demonstrated antibacterial activity and resulted in enhanced proliferation of endothelial progenitor cells, which facilitated the healing of skin in a full-thickness wound model in mice(Chhabra et al., 2016). The zinc scaffolds exhibited significant wound healing only 2

days after wounding and complete closure by day 6—significantly more effective than scaffolds without zinc, which demonstrated efficacy only on day 10. Histopathology analyses confirmed more extensive and faster wound healing with zinc-doped scaffolds compared with scaffolds without zinc. In addition to zinc, cross-linked collagen scaffolds incorporating gold NPs were compared with collagen sponges and commercially available MatriDerm® (MedSkin Solutions) for healing full-thickness skin wounds in adult rats(Akturk et al., 2016). Compared with collagen scaffolds or MatriDerm, the dermal healing was accelerated in the case of gold NP–doped scaffolds, which demonstrated improved tensile strength and neovascularization activity.

Introduction to Laser Tissue Welding

A 1979 report first described the joining of small blood vessels together by laser light to avoid the use of sutures, a technique designated laser tissue welding(Jain & Gorisch, 1979). Laser tissue welding involves the rapid bonding of tissues or tissue edges through the conversion of laser light to heat and uses either an endogenous or exogenous chromophore. A chromophore is a molecule or part of a molecule or particle that can absorb light. In the context of laser tissue welding, the chromophore absorbs laser energy and converts this energy to heat. This heat increases local tissue temperature and induces local changes in the tissue, which can be used to create tissue sealing.

Following the introduction of laser tissue welding (LTW), lasers began to be used in the early 1980s(Abergel & Meeker, 1984) to improve and hasten scar healing(Rabi & Katzir, 2010). Since this time, laser tissue welding has been researched in various tissue types(Gobin, O'Neal, et al., 2005a; Wolf -de Jonge, Beek, & Balm, 2004a), including hypospadias repair(A. Kirsch, Duckett, & Snyder, 1997), urinary tract reconstruction(A. J.

Kirsch et al., 1995), blood vessels(O'Neill et al., 2007; Xie, Bendre, Burke, Gregory, & Furnary, 2004), GI tract(Libutti, Oz, Forde, & Auteri, 1990; Spector et al., 2009), cartilage(Züger et al., 2001), skin(Simhon et al., 2004; P. Yang, Yao, DeMartelaere, Redmond, & Kochevar, 2012), bladder(Lobik, Ravid, & NISSENKORN, 1999), urethra(Shumalinsky & Lobik, 2004), cornea(Paolo Matteini, Rossi, Menabuoni, & Pini, 2007a), liver(Wadia, Xie, & Kajitani, 2000), nerve(Ngeow, 2010; Solhpour, Weldon, Foster, & Anderson, 1994), aorta(Gayen & Katz, 2003), and small intestine(H.-C. Huang, Walker, Nanda, & Rege, 2013b; Mercer, Minich, & Pauli, 1987; Urie, Quraishi, Jaffe, & Rege, 2015b). LTW has potential benefits compared to suturing including shortened procedure times(Capon et al., 2001; Lauto et al., 2008a), scar reduction and prevention(Alster & Zaulyanov-Scanlon, 2007a; Atalay et al., 2009a; Lauto et al., 2008a; Ngeow, 2010), greater procedural ease and minimal tissue handling(Bilici, 2010a; Paolo Matteini, Ratto, Rossi, & Pini, 2012a), improved wound strength in the early postoperative period(L. Hu et al., 2011; Tabakoğlu & Gülsoy, 2010), immediate fluid-tight seal(H.-C. Huang et al., 2013b; Urie et al., 2015b), and reduced healing times(P. Matteini, Ratto, Rossi, & Pini, 2010). Due to these potential benefits and the possibility of wide application, laser tissue welding is an exciting approach with the potential to improve patient outcomes in surgery.

Endogenous LTW relies on naturally occurring chromophores within the tissue and is advantageous(Garcia et al., 2009a; Howard E. Savage et al., 2004; Sriramoju & Alfano, 2012a) because no foreign material is required, limiting scar formation and inflammatory response(L. Hu et al., 2011). However, endogenous LTW is often limited to very thin, transparent, and homogenous tissue (such as the ocular lens), employing laser wavelengths

in the mid and far infrared regions at laser fluences which can cause significant thermal damage to tissue(F Rossi & Pini, 2005). LTW has been investigated extensively for eye surgeries because the tissue has little vasculature, pigment, or pathological changes, while thicker, less homogeneous tissues have been largely unstudied. To address this shortcoming, many studies have relied on water as an endogenous chromophore because it is the major component in tissue, using wavelengths with high absorption by water including CO2 lasers at 10.6 μm, diode lasers at 1900 nm, and erbium:YAG lasers at 2900 nm. Another common natural chromophore is hemoglobin with a maximum absorbance at 488-514 nm(H. E. Savage et al., 2004). Due to limited penetration of laser light at these wavelengths, the outer layer of tissue, exposed to the laser, suffers from heat damage while the lower layers are only weakly heated, indicating possibilities for robustly welding only thin tissues(F Rossi & Pini, 2005). Skin has also been repaired in endogenous LTW studies because it is easily accessible and more robust than many internal tissues.

Optical properties and the composition of endogenous chromophores are vastly different across tissue types, and this variation results in different temperature fields and thermal damage(Li, Protsenko, Zemek, Chae, & Wong, 2007). Tissues such as vasculature, nerves, and intestine, which either possess low content of endogenous chromophores or are significantly heterogeneous in their composition may not be ideal candidates for endogenous LTW.

Exogenous LTW, on the other hand, relies on introducing a chromophore to induce differential laser absorption from the tissue and is effective because these chromophores can convert laser light to heat with much greater efficiency than endogenous chromophores such as water, melanin, hemoglobin, and others(Paolo Matteini, Ratto, et al., 2012a).

Because of this, exogenous LTW can minimize thermal damage, limit the area of exposure, and generate heat more deeply into tissue, but may result in a foreign body response due to the introduced chromophores.

This introductory section discusses recent research progress in exogenous laser tissue welding as well as other noteworthy progress towards advancing laser tissue welding to the clinic. A brief summary of the theory and mechanism underlying laser tissue welding and advancements in chromophores are discussed, with emphasis on the use of nanoparticle-based materials. Additionally, a brief comparison is made with other sutureless wound healing techniques.

exogenous laser tissue welding: mechanisms. Laser tissue welding utilizes a wavelength-specific chromophore to generate sufficient heat, which restructures the extracellular matrix and disorganizes proteins at tissue edges. Upon cooling, this reorganization of native tissue proteins results in collagen interdigitation and noncovalent bonding of laminin and entactin(B. Bleier, Palmer, Sparano, & Cohen, 2007). Laser tissue welding is an appropriate term for this technique because there are many parallels to conventional welding in the proposed mechanism of LTW. The most agreed mechanism is composed of two parts; first, thermal denaturation of the tissue constituents and, second, bond formation as the tissue cools. The exact bonding mechanism is not precisely known due to a number of factors including variation in laser wavelength and power density (power per unit volume or cross-sectional area), length of treatment, spot size and number of spots, variation in tissue-specific factors such as laser absorption, and differences in chromophore and solder types, compositions, and dimensions.

In conventional metal welding, a solder is a low-melting alloy that is capable of fusing metals that are less fusible. Similarly, in the context of tissue approximation and repair, a solder is an exogenous material that facilitates the bonding of tissues or tissue edges. Two distinct approaches, direct and indirect laser welding, are employed in exogenous laser tissue welding. In direct laser welding, an exogenous chromophore is used to stain the wound edges to be bonded. The tissue is irradiated directly. Direct laser tissue welding is sometimes referred to as stained laser tissue welding. Indirect laser tissue welding, sometimes referred to as laser tissue soldering (LTS), employs an exogenous chromophore within a liquid or solid "solder". The solder is placed or applied over the wound edges and irradiated to generate heat and seal the underlying tissue. This method is advantageous because the tissue is not directly irradiated; the wavelength of light can be tuned to minimize absorption by the natural chromophores in the tissue, and the exogenous chromophores can greatly increase photothermal conversion compared to endogenous chromophores. The tissue "therapeutic optical window" is the region from 700–1,300 nm in which little to no laser radiation is directly absorbed(B. S. Bleier, Palmer, Sparano, & Cohen, 2007a) by the tissue.

The theory and mechanism of action of LTW have mainly been derived from the heating of rat tails(J. Cezo, Kramer, Taylor, Ferguson, & Rentschler, 2013) and other highly collagenous tissues such as cornea(Garcia et al., 2009a) and arteries(Esposito et al., 2013b; Dara R. Pabittei, Heger, van Tuijl, et al., 2013). Laser light converted to heat denatures and fuses tissue proteins(Constantinescu et al., 2007a; L. W. Murray, Su, Kopchok, & White, 1989a). Denaturation of collagenous tissue occurs in three phases, revealed by second-harmonic generation microscopy(Paolo Matteini, Cicchi, et al., 2012b;

23

Paolo Matteini, Ratto, et al., 2009a). First, proteoglycan bridges between fibrils are broken around 45°C. Second, at 60°C collagen starts to collapse due to hydrolysis of intramolecular H-bonds. Third, complete collagen denaturation and tissue homogenization occur above 80-85°C due to hydrolysis of covalent peptide bonds(Small IV, Da Silva, & Matthews, 1998). However, irreversible tissue thermal damage begins at temperatures as low as 40°C. Because of this large difference, it is important to find the minimum temperature necessary to create robust welds and also localize the heat and area of exposure to a feasible extent. Temperature at the wound bed surface in direct exogenous LTW and the solder-tissue interface in LTS is an indirect indication of the status of the wound during laser treatment(Cilesiz, 1999). As detailed by Fourier's law, the heat transferred to the wound bed by conduction is proportional to the temperature gradient of the solder-tissue interface.

An optimal temperature range to produce robust welds of pure type I collagen may occur from approximately 60–66°C. Mouse skin was shown to coagulate *in vitro* above 60°C(SL Jacques & Prahl, 1987). In another study, bovine aortic tissue was welded with dye-albumin solders. Below 66°C at the solder-tissue interface, the tissue was not sealed, but at 66°C the tissue was sealed with maximum tensile strength. Above this temperature, the tensile strength decreased with increasing temperature(Hoffman, Byrd, Soller, Heintzelman, & McNally-Heintzelman, 2003a). This suggests that complete collagen denaturation is not required for patent tissue welds. Because other extracellular matrix components have transition temperatures below 60°C, other tissue types may have an even lower optimal LTW temperature range.

In another study, porcine eyes were stained with ICG and corneal wounds were successfully welded with temperatures in the 55–65°C range. Atomic force microscopy and transmission electron microscopy of the welded corneal wounds revealed that normal fibrillar structure was largely disorganized, but the collagen was not denatured (Figure 5)(P Matteini, Sbrana, Tiribilli, & Pini, 2009). This work suggests that even mild changes in the stroma ultrastructure can facilitate new ocular tissue bonding.
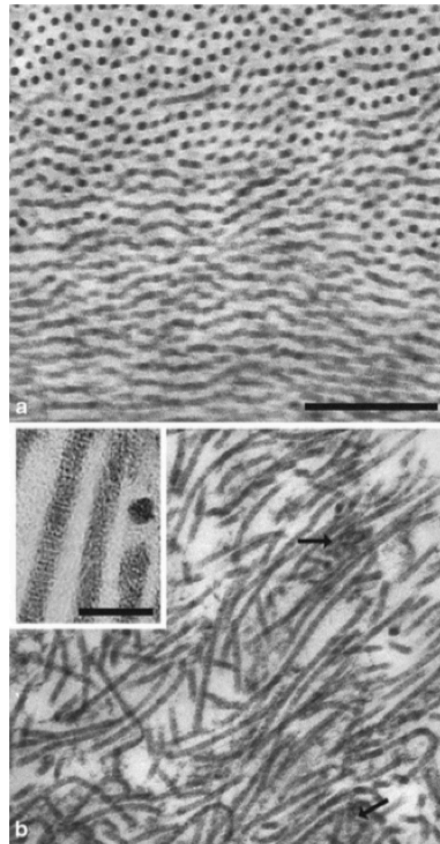
Figure 5. Transmission electron microscopy of corneal stroma. (Top) without laser irradiation and (bottom) at the weld site. Scale bar is 400 nm and the insert scale bar is 100 nm. Reproduced from (P Matteini, Sbrana, Tiribilli, & Pini, 2009.

Cezo et al. demonstrated that water bound to extracellular matrix (ECM) proteins is driven off by laser irradiation, opening sites for bonding(J. Cezo et al., 2013). Elastin(J.

Cezo et al., 2013; Norman, Rabi, Assia, & Katzir, 2009), decorin, cells, and other extracellular matrix components still have yet to be analyzed in detail following laser welding to better understand the effects of heat and laser irradiation. By analyzing these components in greater detail, more in-depth spatiotemporal modeling could be used to predict the optimal temperature range for a wider variety of tissue types.

A number of parameters can be used to assess the effectiveness of LTW treatment. Bond tensile strength is measured by pulling the tissue apart at a fixed rate and can provide a rapid preliminary assessment of the robustness of the welded closure. For laser tissue soldering, the mode of failure - cohesive or adhesive(Dara R Pabittei et al., 2011) - is an important additional observation from tensile strength testing. Often more clinically-relevant, the burst pressure is the most widely used mechanical parameter for determining the patency of welded tissue. The welded tissue is filled with fluid until leakage or bursting, as shown in Figure 6. Other less commonly-reported but valuable treatment outcomes are water loss, histological analysis, scarring, bacterial leakage across the weld, and cell viability and biocompatibility in the case of laser tissue solders. Additionally, the surface temperature of the tissue or solder can be monitored directly to provide valuable information regarding the correct laser parameters (power density and exposure time) to maintain optimal temperature(F Rossi & Pini, 2005; Urie et al., 2015b).
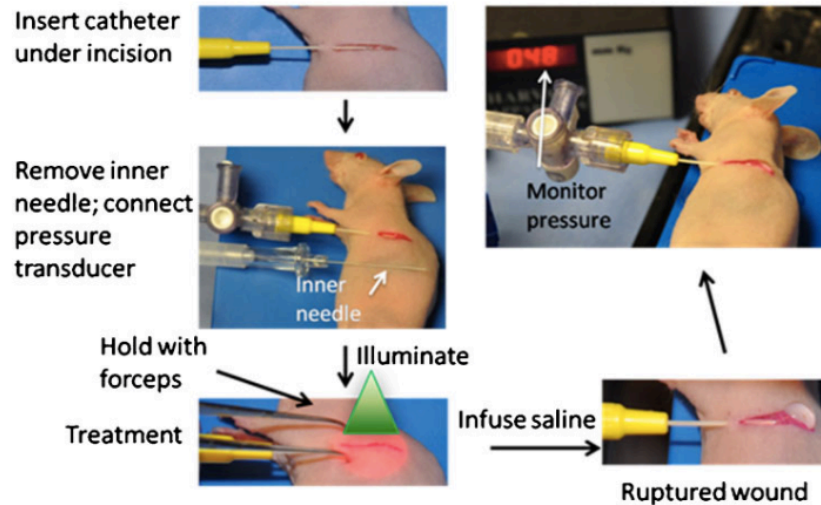
Figure 6. Measurement of weld strength in skin closures of mice. Saline solution is infused and the burst pressure is recorded. Reproduced from Dara R Pabittei et al., 2011.

A number of factors can be cause for concern with regards to LTW, and these factors can hinder further growth and clinical translation. These factors include low weld strength in some cases(Dara R. Pabittei, de Boon, et al., 2013), thermal damage(Dara R. Pabittei, de Boon, et al., 2013), overcoming normative suture use, current application for only very thin transparent tissue(Ratto et al., 2009a), training required(Schalow & Kirsch, 2003), subjectivity and ambiguity regarding endpoint of welding(Hoffman et al., 2003a; Schalow & Kirsch, 2003) and inconsistency in results(Garcia et al., 2009a; Lauto et al., 2008a). These concerns are being improved through technical advances in chromophores and solders(Gobin, O'Neal, et al., 2005a; H.-C. Huang et al., 2013b; Francesca Rossi et al., 2011; Urie et al., 2015b) as discussed in the subsequent sections. Full automation of laser dosimetry may be necessary for more general application(Cilesiz, 1999), and surgical experience and surgeon motor reflexes also contribute significantly to LTW success rates(Cilesiz, 1999). Meticulous hemostasis is likely necessary prior to tissue welding(Schalow & Kirsch, 2003), and potential problems for high stress regions are

possible(Sorg & Welch, 2003). Laser equipment can be costly, however, portable, handheld diode lasers with continuous or pulsed wave NIR light are becoming available at relatively low cost. The equipment used for LTW ranges in size and price. Some groups have incorporated large robots to automate welding(Garcia et al., 2009a), while others use portable handheld laser fiber optic cables that are quite inexpensive(Gobin, O'Neal, et al., 2005a). Additionally, the treatment length compared to that of conventional suturing depends largely on the type of LTW. For endogenous LTW, the powers and wavelengths are so high as to take from 5 to 15 seconds per spot. This is much shorter than suturing times. For thicker tissue and with exogenous LTW, especially with indirect LTW, the times are longer due to the necessary heat transfer through the exogenous solder and the thick tissue. In these cases, the time is on the order of minutes and is generally not spot treated. The time required may be even greater than that for suturing, depending on the laser power used. Additional innovation will be necessary to shorten the length of treatment in these cases. Also, treatment planning varies from study to study. Some spot weld the incision with a varying number of spots and others perform a continuous weld by moving the laser along the incision at varying speeds and with a varying number of passes. Additional work within the field is needed to assess the large parameter space involved in welding and optimize techniques to minimize laser exposure, treatment time, and peripheral thermal damage.

Sutured closures have been reported to elicit a stronger inflammatory response than laser soldered closures, and the inflammatory response has a longer duration with sutured wounds as well(L. S. Bass & Treat, 1995; Sorg & Welch, 2003). Additionally, laser exposure results in local hemostasis which prevents scabbing, excessive blood flow, and

bacterial transfer(D'Arcangelo et al., 2007). The perfusion rates of blood vary greatly by tissue type and body location. At high blood perfusion rates, the convective heat loss will be stronger and will result in less thermal damage. A dual-phase lag model has been developed to evaluate thermal damage of laser irradiation in tissue(K.-C. Liu & Wang, 2014; Zhou, Chen, & Zhang, 2009) based on an assumption that thermal damage can be treated as a chemical reaction with a rate process for three steps: (1) laser deposition in tissue, (2) heat transfer, and (3) protein denaturation(Welch, 1984; Zhou, Zhang, & Chen, 2008). Nonlinear finite-element analysis to simulate the dynamic evolution of coagulation in laser-heated tissue using a prostate model showed that photo-coagulation results in three unique regions of blood flow(B.-M. Kim, Jacques, Rastegar, Thomsen, & Motamedi, 1996). First, a superficial region of coagulation where blood flow is limited or negated due to thermal damage which is typically quite small. Second, a deeper thin ring of increased blood flow around the coagulated region known as the hyperemic region. Third, a deeper region where blood perfusion remains normal, and the tissue remains at 40°C. The hyperemic region acts as a heat sink, preventing an expanded region of coagulation and thermal damage.

advances in laser tissue welding: exogenous chromophores and sealants. Exogenous chromophores for laser tissue welding can be selected or tuned based on a peak absorption wavelength that does not coincide with the natural chromophores in tissue. By using laser irradiation in the near infrared (NIR) therapeutic optical window(Esposito et al., 2013b), heat is localized and peripheral tissue damage is limited(Schalow & Kirsch, 2003). The near infrared region is the region of light with wavelengths longer than visible

light, beginning roughly at the red end of the visible spectrum at 700 nm and extending to 1300 nm.

In the 1980s, solders were introduced to improve the tensile strength of laser-sealed tissue(Schalow & Kirsch, 2003). The first exogenous chromophores introduced for use in laser tissue welding were FDA-approved organic dyes for ocular surgeries. The most widely researched of this group is the FDA-approved dye indocyanine green (ICG) coupled with an 810-nm wavelength NIR laser. ICG has been widely researched due to high biocompatibility compared to other organic dyes. However, ICG and other organic dyes such as methylene blue and fluorescein suffer from a number of serious limitations. The dyes alone bleed into the tissue periphery, which may lead to increased thermal damage. These dyes have been shown to photobleach relatively quickly and are not stable over long periods of time(Hoffman et al., 2003a). Despite these concerns, direct laser tissue welding has shown promising results as discussed below.

Tests that simulated penetrating keratoplasty in four eyes of rabbits showed that ocular repair occurred more quickly and tissue restoration was more effective with ICG-stained tissue and laser treatment than with the suture control (Figure 7)(F Rossi & Pini, 2005). Tabakoğlu and Gülsoy compared closure techniques of rat dorsal skin(Tabakoğlu & Gülsoy, 2010). Suturing, 809-nm laser with albumin-ICG solder, 980-nm laser without solder, and 1,070-nm laser without solder were all compared over a 21-day recovery period. All welding techniques were successful at immediate skin closure (Figure 8), while suturing was not, and all welding techniques showed mechanically stronger closure than suturing at the end of the study.
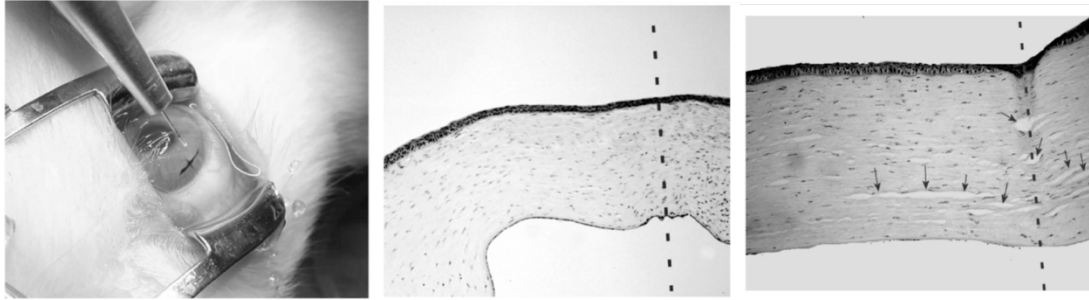
Figure 7. Laser tissue welding of rabbit cornea. (Left) Welding a corneal cut held by a single stitch at the center. Histological section of (center) a laser-welded cornea and (right) a sutured cornea at 30 days post operation. Large lacunae (arrows) are present in the sutured cornea but not seen in the welded cornea. Reproduced from (F Rossi & Pini, 2005.
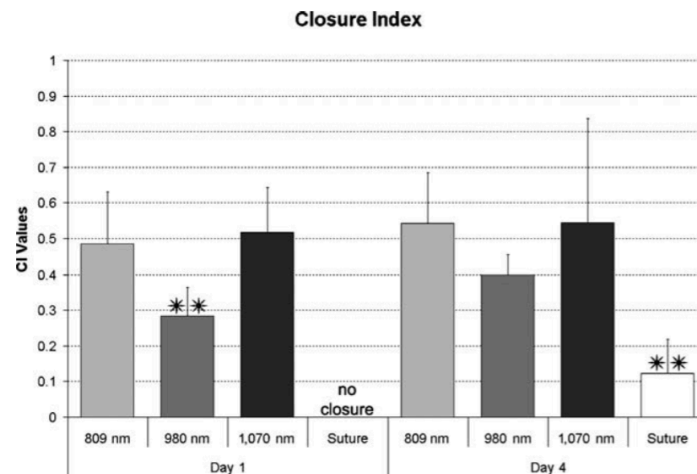
Figure 8. Closure index of procedures using various laser modalities. Figure 4. Closure index values of closing skin incisions using sutures or near infrared laser at 809 nm with solder, 980 nm, or 1070 nm. All laser modalities showed immediate closure at day 1. The 980-nm closure was statistically lower than 808-nm and 1070-nm (* *) ($P<0.05$). On day 4 post-repair, the sutured group closure index was statistically lower than the laser-irradiated groups (* *) ($P<0.05$). Reproduced from Tabakoğlu & Gülsoy, 2010 .

Organic dyes do have a number of inherent advantages over metal nanoparticles: small molecular size and synthetic flexibility, and some research is exploring alternative

small molecule chromophores to ICG that are not limited by low stability and rapid photothermal bleaching. For example, Spence et al. showed that croconaine dyes respond to NIR laser with unusually great stability and efficient heating, making them suitable candidates for laser tissue welding(Spence, Hartland, & Smith, 2013).

Rose Bengal (RB) dye is unique in that it elicits a photochemical response rather than a photothermal response following laser irradiation, generating no significant heat in the process (Figure 9). While not following exactly the same mechanism as LTW, this "photochemical tissue bonding" has shown promising results. Incisions in rat median nerves were repaired *in vivo* using a chitosan adhesive film mixed with RB and a 532-nm green laser. While the sutured group resulted in greater tensile strength than RB-chitosan treatment after one week, this photochemical process resulted in better nerve realignment and organization compared to the disorganized suture repair(Barton et al., 2013). Additionally, an *in vivo* study on the sciatic nerve of adult rats was performed using photochemical tissue bonding (PTB) and RB with green laser at 532 nm. Several combinations were tested with PTB, sutures, a human amniotic membrane wrap, and an autologous vein wrap. The study showed that PTB alone and PTB with the amnion wrap showed significant functional improvement over the suture alone(O'Neill et al., 2009). In another study, *ex vivo* incised calf intestine was treated with a 532-nm laser and an adhesive albumin-RB film. The laser application significantly increased the adhesion strength and did not increase the average temperature of the adhesive. This is an example of photochemical tissue bonding (PTB) that causes crosslinking of fibers without producing heat(Lauto et al., 2010).
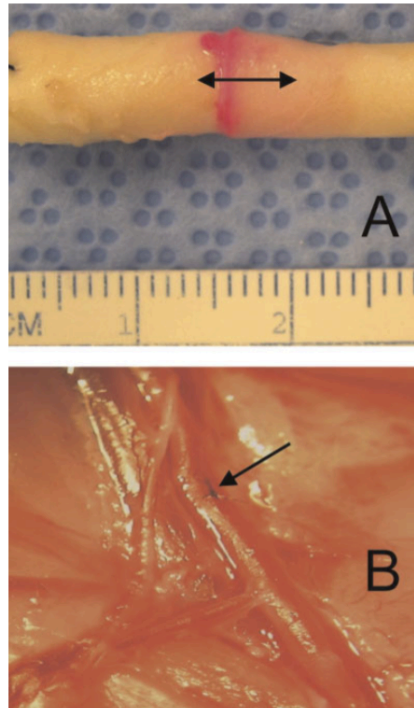
Figure 9. Laser tissue welding of porcine artery. (A) *Ex vivo* porcine carotid artery closure by photochemical tissue bonding. Arrow indicates are of artery overlap. (B) *In vivo* rat femoral artery 6 hours following repair. Arrow shows the repair site with a marking stay suture. Reproduced from Barton et al., 2013.

Inorganic nanoparticles, including gold nanorods (Figure 10), are finding greater use as chromophores for LTW. While gold nanoparticles have been studied extensively, a fundamental examination of nanoparticle heating demonstrated that carbon black, single-walled carbon nanotubes, silver nanoparticles, and copper nanoparticles can all be used as NIR chromophores(Schrand, Stacy, Payne, Dosser, & Hussain, 2011). Gold nanorods (GNRs) are being extensively researched in many medical applications, including laser welding(Gobin, O'Neal, et al., 2005a). GNRs are stable over long periods of time, do not leach easily due to their larger size, facilitate efficient photothermal conversion, and do not undergo photobleaching(Hoffman et al., 2003a). GNRs are widely-employed due to

tunable shape, functionalization(Brust, Fink, & Bethell, 1995), and localized heat(M. Daniel & Astruc, 2004; H.-C. Huang, Rege, & Heys, 2010a). Light absorption by GNRs can be tuned to a maximum absorbance wavelength by adjusting the size ratio of the nanoparticles. Additionally, the surface of these nanoparticles can easily be modified to shield the nanoparticles from the immune system, alter their properties, and / or to conjugate bioactive molecules.
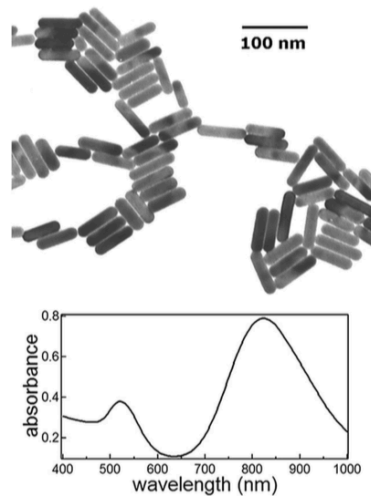
Figure 1. Transmission electron micrograph and ultraviolet-visible NIR spectra of the gold nanorods used in the tests.

Figure 10. Gold nanorod chromophore characteristics. (Top) Transmission electron microscopy image of gold nanorods and (bottom) gold nanorod absorption spectra. Reproduced from Ratto et al., 2009a.

GNRs convert light to heat through collective electron oscillations(Ratto et al., 2009a). Various groups have calculated that roughly five orders of magnitude fewer GNRs are required to produce the same amount of heat as ICG, making GNRs a million-fold more effective NIR light absorbers. Colloidal GNRs were used to directly stain porcine eye lens capsules *ex vivo* at the interface between a patch from a donor eye and the treated eye. Laser pulses (40 msec) locally denatured the ocular collagen, reaching temperatures above

50°C confined to within 70 μm from the area of exposure (Figure 11)(Ratto et al., 2009a), showing the extent to which heat can be localized. In another study, the hetero-transplantation of *ex vivo* porcine lens capsules that were soaked in a collagen-GNR mixture and welded with an 810-nm diode laser was performed. Results showed successful welding at a heat flux of less than half of the tissue collateral damage threshold, a roughly two-fold improvement over ICG(Ratto et al., 2008).

Indirect laser tissue welding or laser tissue soldering (LTS) employs an exogenous chromophore within a liquid, semi-solid or solid solder. Laser light induces conformational changes in collagen in many different types of tissue. In the cochlea basil membrane, for example, delayed effects of laser radiation on collagen result in increased tissue stiffness(Wenzel, Anvari, Mazhar, Pikkula, & Oghalai, 2007). LTS can potentially avoid these effects of tissue exposure to laser. These solders are typically polymers with high biocompatibility. This avoids direct staining and irradiation of the tissue and employs wavelengths in the therapeutic optical window.
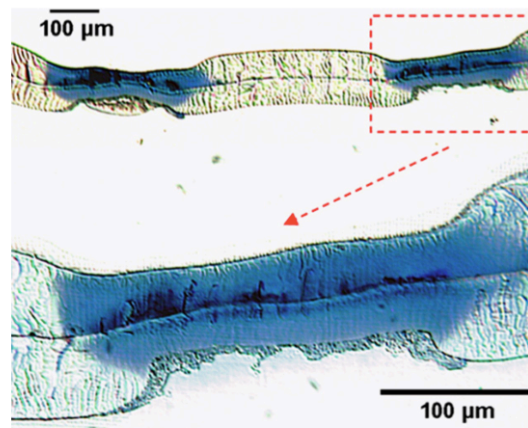
Figure 11. Laser tissue welding of lens capsule. Histological section of spot laser welding of sandwiched anterior lens capsules with toluidine blue stain. The results from each spot are reproducible. Reproduced from Ratto et al., 2009a.

Liquid solders with organic dyes are reported to be difficult to handle(C. Bleustein & Walker, 2000) and can lead to inconsistent results in weld strength. Albumin is among the most commonly studied solder material, and is often coupled with ICG and NIR laser at 800–810 nm. Higher concentrations of albumin (semi-solid solders) correlate with increased bond strength and higher burst threshold pressures(B. Bleier et al., 2007). On the other hand, solid thin films can be inflexible, and are not readily able to incorporate into or adapt to the tissue geometry(Francesca Rossi et al., 2011).

An *ex vivo* study on porcine aortas utilized laser-assisted vascular welding. Poly(ε-caprolactone) (PCL) and poly(lactic-co-glycolic acid) (PLGA) scaffolds were created with semi-solid albumin solder and albumin solder containing hydroxypropylmethylcellulose (HPMC) to improve bonding. A 670-nm diode laser was used, and the breaking strength, resilience under hydration, and thermal damage were assessed. PLGA welds were stronger in terms of breaking strength, but did not hold up well with hydration. The addition of HPMC increased the breaking strength of PLGA welds after hydration. Pulsed, as opposed to continuous wave, laser inflicted less tissue damage(Dara R. Pabittei, Heger, Simonet, et al., 2013). This work highlights the possibility of using multi-phase polymer composites to combine the ease and reproducibility of a solid solder with the wound integration of a viscous solder.

Chitosan is another solder matrix material being explored in LTW(Esposito et al., 2013b; Lauto et al., 2010). Chitosan is biocompatible, inexpensive, and can be processed into very thin transparent films. In one study, chitosan films embedded with GNRs were placed on rabbit tendons and irradiated with pulsed-wave 810-nm diode laser. Strong adhesion was measured using tensile strength tests(P. Matteini et al., 2010). Matteini et al.

sealed rabbit carotid artery *in vivo* with an 810-nm diode laser and a hyaluronan-GNR composite. Immediately after the procedure, there was no bleeding and artery patency was confirmed. Follow-up showed patent arteries and no adverse host reaction to the soldering material. Hyaluronan provided stability to the solder(Paolo Matteini, Ratto, Rossi, Rossi, et al., 2010).

The Rege group employed thin elastin-like polypeptide (ELP) matrices crosslinked with GNRs to weld ruptured porcine intestine with 800-nm laser irradiation. Fluid-tight seals in the intestine were created (Figure 12), and bacterial leakage across the weld did not occur, indicating the application of these solders in preventing anastomotic leakage(H.-C. Huang et al., 2013b). Collagen is vital in wound healing and mimics the extracellular matrix(Fang, Yuan, Peng, & Li, 2014; Shoulders & Raines, 2009a), with low immunogenicity(Alencar, Funovics, & Figueiredo, 2007). Previously, collagen applied by laser improved wound healing and reduced scarring in skin(Steinstraesser et al., 2010a). Our group additionally explored collagen-GNR thin hydrogel solders *ex vivo* in porcine intestine with 800-nm laser. The burst pressure of welded intestine reached up to 64% of that of native intestine while greatly minimizing laser power density compared to other studies. Pulsed wave laser created robust welds while maintaining lower temperatures at the solder-tissue interface than continuous wave laser(Urie et al., 2015b).

The success of these improvements in chromophores and solders highlights the need for further development of next generation solders for laser tissue welding. Multi-wavelength chromophore systems, improved composite adhesiveness, drug loading, photochemical bonding, and plasmonic nanoparticles all have the potential to drive enhancement of laser tissue welding results.
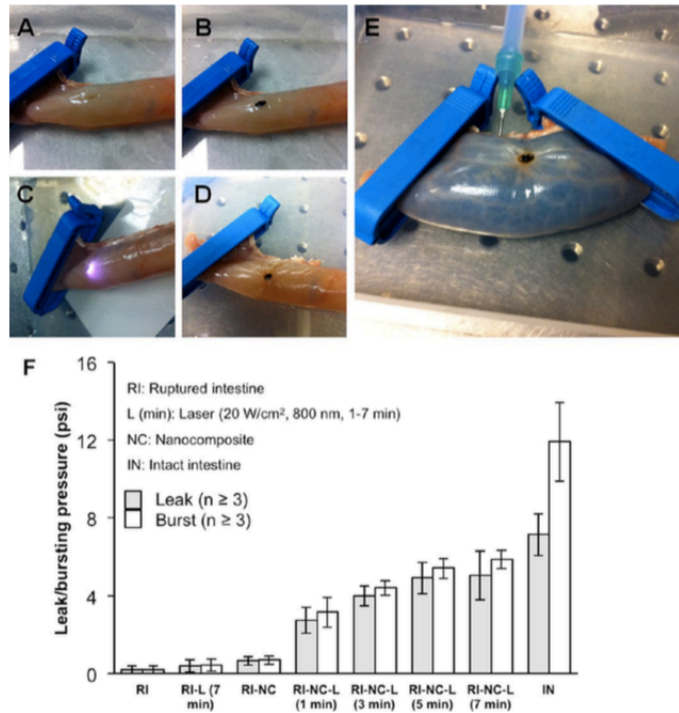
Figure 12. Leakage and burst pressures of welded intestine. (A) 5mm incision made in the intestine. (B) Solder placed over incision, and (C) irradiated with a laser to (D) create a seal. (E) The leaking and bursting pressures were measured and reported. (F) Bursting and leakage pressures of tissues before and after laser tissue welding using nanocomposite solders. Reproduced from H.-C. Huang et al., 2013b.

competing sutureless techniques. Different types of sutureless tissue fusion methods for wound healing include surgical sealants or adhesives and direct heat tissue compression devices. While a detailed review of these techniques cannot be given here, a brief and qualitative comparison to laser tissue welding is described in the following section.

Adhesives, including cyanoacrylate or fibrin glues, often suffer from toxicity, brittleness, low wound strength (especially in wet wound settings), long polymerization

times, difficult application, wound reopening, and poor uniformity. Some thin film adhesives are able to create an instant seal and prevent bacterial leakage but may not be suitable for load-bearing tissue, vascular, nerves, or muscle. Alternatively, direct heat tissue fusion devices require a more available wound site and lead to greater and more widespread thermal damage. The tissue is sealed by clamping wound edges together and directly applying heat to the clamp(J. D. Cezo, Passernig, Ferguson, Taylor, & Rentschler, 2014a).

Laser tissue welding was compared to fibrin glue in the closure of *ex vivo* lung and tracheal incisions on rabbits. An 808-nm diode laser was used with a solder composed of bovine serum albumin, indocyanine green dye, and either hyaluronic acid or chitosan (gelling agents). LTW provided burst strengths that were twice as high as fibrin glue. Solders composed of chitosan required much less laser time than hyaluronic acid solders(B. S. Bleier, 2010a).

Conclusions

The chromophores, solders, and procedures employed for laser tissue welding have changed very little since the 1990s. Despite this, the results from laser tissue welding show that this technique has great potential for clinical translation and application. The more recent work highlighted in this chapter shows that technical advances in exogenous chromophores, tissue solders, and heat management will continue to improve laser tissue welding results.

Inorganic nanomaterials, namely materials composed of at least one metallic, ceramic, or carbon allotrope constituent with one or more dimensions on the order of 1–100 nm, can fill a variety of unmet needs in nanomedicine. Inorganic nanomaterials show

promise in tissue repair and regeneration that may potentially lead to improved patient outcomes. Inorganic NPs can improve and modulate material mechanical properties, which play a key role in the ability to tune the material to a specific tissue type or disease state. In addition, inorganic NPs promote cell adhesion and stem cell differentiation. Biological cues including growth factors can also be integrated into these nanomaterials. Inorganic NPs impart electrical, optical, magnetic, or antimicrobial properties to repair cardiac, neural, and skin tissue, among others. Finally, they can also facilitate drug and nucleic acid delivery, which can accelerate/engender tissue repair and regeneration. Additional studies are necessary to develop a clearer understanding of structure–property relationships with a focus on how size, shape, and surface chemistry lead to effective tissue repair *in vivo*. The safety of inorganic NPs in tissue repair and regeneration also needs to be elucidated, particularly for long-term repair and regeneration. As inorganic NPs enter the clinic for concomitant applications, including imaging, cancer treatment, drug delivery, dentistry, and cosmetic products, the pathway for FDA approval and clinical translation of inorganic nanomaterials for tissue repair and regeneration is likely to become more streamlined.

GOLD NANOROD-COLLAGEN PLASMONIC NANOSOLDERS FOR LASER WELDING OF RUPTURED PORCINE INTESTINES

Introduction to *Ex Vivo* Laser Tissue Welding

Over 1.5 million people suffer from colorectal cancer or inflammatory bowel disease in the US (Center for Disease Control and Prevention and National Cancer Institute). Colorectal and intestinal surgeries often require resection of a portion of the colon, necessitating anastomosis. In anastomosis, disjointed sections of tissues are joined together. Intestinal anastomosis is typically carried out using hand-placed sutures or surgical staples. These conventional techniques may lead to anastomotic leakage, which results in infection, septic shock, and ultimately patient death. It is suggested that clinical leakage occurs in 17% of all colorectal anastomoses cases(Park, 2010a), and clinicians predict that the number of patients at risk for anastomotic leakage will rise(Park, 2010a).

A suture-free, rapid hydrosealing approach towards anastomoses and tissue repair is less invasive and can decrease infection, prevent leakage, shorten operative times, and improve healing rates. Sealants, including fibrin glues, are limited by difficult application, poor uniformity, and low wound strengths(B. S. Bleier, 2010b), especially in wet wound environments(Duarte, Coelho, Bordado, Cidade, & Gil, 2012a). As an alternative, near-infrared (NIR) radiation can be applied to a plasmonic protein matrix to adjoin ruptured tissue. This laser tissue welding (LTW) approach is an attractive stitch-free method with application in surgeries involving intestine, blood vessels(Wolf -de Jonge, Beek, & Balm, 2004b), nerves(Schober, Ulrich, Sander, Dürselen, & Hessel, 1986), and skin(Gobin, O'Neal, et al., 2005b). In addition, LTW has the potential to reduce the skill required for performing efficient anastomosis(Bilici, 2010b). While the mechanism behind LTW is

somewhat unclear(Constantinescu et al., 2007b)ʾ(Sriramoju & Alfano, 2011a), recent research has resulted in greater understanding of laser-mediated tissue bonding. Second-harmonic generation microscopy reveals a three-step thermal transition of corneal collagen denaturation, where interfibrillar proteoglycan bridges are broken at 45°C, intramolecular collagen hydrogen bonds are broken at 60°C, and the protein is fully denatured and homogenized at 80°C(Paolo Matteini, Cicchi, et al., 2012c). As a result, the proposed mechanism of LTW is as follows. The incident laser radiation is converted to heat, which denatures and eventually fuses(Paolo Matteini, Ratto, et al., 2009b) tissue proteins, resulting in interdigitation of photothermally altered tissue proteins, which facilitates bonding and sealing(Lawrence S. Bass et al., 1992)ʾ(L. W. Murray, Su, Kopchok, & White, 1989b).

An exogenous chromophore is typically used to generate sufficient heat for tissue welding, given inefficient absorption of laser energy by biological tissues. While LTW treatments have been moderately successful without an exogenous absorber(Garcia et al., 2009b)ʾ(Sriramoju & Alfano, 2012b), chromophores allow the use of radiation that is very minimally absorbed by the tissue. This can reduce thermal damage, limit the need of complex robot-assisted treatments, and facilitate welding of larger tissue dimensions(Gobin, O'Neal, et al., 2005b). However, LTW with these monolithic materials (such as organic dyes) and protein-dye "solders" has been limited by poor laser penetration, peripheral tissue damage, chromophore diffusivity, and poor uniformity of treatment.

Plasmonic nanoparticles absorb NIR light more efficiently than organic dyes(X. Huang, Jain, El-Sayed, & El-Sayed, 2008)ʾ(Hirsch et al., 2006), and gold nanorods (GNRs) are attractive photothermal convertors for laser welding of tissues(H.-C. Huang, Rege, &

Heys, 2010b)'(H.-C. Huang, Walker, Nanda, & Rege, 2013c). GNRs show exceptional optical absorption based on size and morphology, greater stability under physiological conditions, low diffusivity through tissue, and excellent localization of photothermal conversion(Ratto et al., 2009b)'(Qin & Bischof, 2012). Embedding the plasmonic chromophore in a thin-film protein nanocomposite rather than within a high viscosity "solder" can make tissue manipulation easier, decrease closure time, and limit chromophore diffusion(Garcia et al., 2009b).

Collagen, the principal structural constituent in tissues, is the most abundant protein in the body(Shoulders & Raines, 2009b). Collagen scaffolds have been previously fixed to wounds using laser exposure with improved healing and reduced scarring(Steinstraesser et al., 2010b). Here, GNR-collagen nanocomposites (NCs) were developed for *ex vivo* laser welding of ruptured porcine intestinal tissue. The mechanical and photothermal properties of these nanocomposites were modulated to optimize LTW while minimizing laser exposure. In addition, the photothermal behavior of these NCs was determined in response to various laser and material parameters to identify optimal conditions for tissue welding applications. The ultimate tensile strength of welded tissue was significantly enhanced over ruptured intestine, and laser welding resulted in recovery of both leak and burst pressures from ruptured intestines, indicating the promise of these photothermal nanocomposites in laser-facilitated tissue repair.

Materials and Methods

materials. Gold (III) chloride trihydrate (HAuCl$_4$•3(H$_2$O)), cetyltrimethyl ammonium bromide (CTAB), L-ascorbic acid, sodium borohydride, and silver nitrate were purchased from Sigma-Aldrich. Type I rat-tail collagen was purchased from Advanced

Biomatrix. All chemicals were used as received without further purification unless noted below. Fresh porcine small intestines were purchased from Animal Technologies, Inc.

synthesis of gold nanorods. Gold nanorods (GNRs) were synthesized via seed-growth(Babak Nikoobakht & El-Sayed, 2003). All chemicals were freshly prepared in nanopure water (resistivity ~ 18.2 MΩ-cm). Briefly, a seed solution was prepared by sodium borohydride mediated reduction of $HAuCl_4 \bullet 3(H_2O)$ in CTAB. The growth solution was prepared by adding L-ascorbic acid to reduce $HAuCl_4 \bullet 3(H_2O)$ in a CTAB solution with silver nitrate. The seed solution was introduced to the growth solution, forming nanorods stabilized by a CTAB bilayer(Babak Nikoobakht & El-Sayed, 2003). These GNRs possessed absorbance maxima (λ_{max}) in the NIR window (700-900 nm) and were tuned to 800 nm. Absorption, as shown in Supporting Figure S2.1, was determined using a Biotek Synergy2 plate reader. Nanorod aliquots were centrifuged (6000 rcf, 10 min) and resuspended in nanopure water to various final concentrations. Gold concentration was determined using inductively coupled plasma optical emission spectrometry (Thermo Electron Corporation). Further centrifugation, decanting, and dilution steps allowed the generation of a nanorod dispersion with CTAB concentration under 0.25 mM; previous work by the group determined that CTAB concentrations below 0.25 mM are optimal for elastin-like polypeptide (ELP)-based nanocomposites formed with GNRs(H.-C. Huang, Nanda, & Rege, 2012a). In this work, the collagen hydrogels were even more sensitive to free CTAB concentration, and, as a result, additional centrifugation further reduced free CTAB from GNR dispersions.

formation of gnr-collagen nanocomposites. Type I collagen was brought to 4 mg/mL using cold 2X phosphate buffered saline (PBS; pH 7.4), neutralized using 1 M

44

NaOH, loaded in a 48-well plate, and gelled in a humid incubator at 37°C for one hour. The resultant hydrogels (~2 mg collagen) were 12 mm in diameter and 10 mm in height, as determined by a digital caliper.

Conventional collagen hydrogels contain as high as 95% fluid(Levis, Menzel-Severing, Drake, & Daniels, 2013), but plastic compression can remove excess fluid to improve the mechanical properties of collagen hydrogels(Levis et al., 2013)˙(Brown, Wiseman, Chuo, Cheema, & Nazhat, 2005). Through compression, the hydrogel is decreased to <2 mm in thickness(Busby, Grant, MacKay, & Riches, 2013). A cylindrical device, shown in Supporting Figure S2.2, composed of a metal mesh, a paper absorbent, and a one-gram weight (2 grams total weight) was placed on top of the NC in each well. The use of this device, following collagen gelation for 30 minutes, resulted in a decrease in gel thickness from 10 mm to ~1 mm. Uncompressed and compressed gels were then incubated in 3 mL GNR dispersions at various concentrations (corresponding to 1, 2, 5, 7, or 10 wt%) and incubated at 28°C for 24 hours, resulting in the formation of GNR-collagen nanocomposites.

characterization of gnr-collagen nanocomposites. GNR leaching from the NCs was determined by incubating the gels with 20 mL of 1X PBS in scintillation vials at 37°C and 100 rpm. Over a sixty-day period, 100 μL samples were periodically removed from the solution and analyzed for GNR absorbance. Also, 1.5 mL was removed from each sample weekly and concentrated to ~150 μL using a Vacufuge Plus (Eppendorf). These samples were also analyzed for nanorod absorbance in the NIR region, and the 1.5 mL was replaced with fresh PBS. GNR-collagen nanocomposites, with 0, 1, 2, 5, 7, and 10 weight

% GNRs, were tested in three independent experiments, and a representative spectrum from one of the samples is shown in Supporting Figure S2.1.

Nanocomposites were incubated in H_2O for 24 hours and weighed (m_{wet}) to determine swelling properties. The nanocomposites were then lyophilized and weighed again (m_{dry}). The swelling ratio (S) was calculated as: $S = (m_{wet} - m_{dry})/m_{dry}$. Swelling ratios are reported as mean ± one standard deviation from five independent experiments.

Environmental field-emission scanning electron microscopy (FE-SEM), using a PHILIPS FEI XL-30 SEM, was employed to facilitate visualization of GNRs within the collagen matrix. SEM studies were carried out at the Leroy Eyring Center for Solid State Sciences at ASU.

rheological properties. An AR-G2 rheometer (TA Instruments) was used to analyze the mechanical properties of the NCs in an 8-mm diameter parallel plate configuration. The samples were loaded between the plates at a normal force below 0.1 N. Samples remained on the Peltier plate for at least 30 min to exclude any time-dependent relaxation. Samples were tested using a dynamic frequency sweep from 1 to 40 rad/s angular frequency at 25°C and a controlled strain amplitude of 0.05. Nanocomposites were also tested by temperature sweep from 25°C to 85°C at a rate of 3°C/min at a fixed angular frequency of 20 rad/s and strain amplitude of 0.05. The elastic storage modulus (G') and the viscous loss modulus (G") were used to calculate the absolute shear modulus, $|G^*| = (G'2 + G"2)0.5$, and the loss tangent, $\tan \delta = G"/G'$. For reference, purely viscous Newtonian fluids have a 90° loss angle (δ), and the loss angle for purely elastic ideal solids is 0°. All values are displayed as mean ± one standard deviation from five independent experiments.

laser configuration. A solid-state titanium sapphire laser (Spectra-Physics, Millennia) was used for laser treatments. The laser excitation source was configured as follows: a 2 mm diameter beam was passed through a cylindrical lens and screened by a 2×15 mm mask (30 mm2 area) to adjust the area of laser exposure to encompass the entire wound bed site (as described in the experiments below). This expanded area of laser treatment negates the need for sample movement or laser pattern procedures, accommodating minimal skill requirements. In addition, the laser was run at both continuous wave and femtosecond pulsed wave (130 fs pulses at 12.5 ns intervals) conditions, referred hereafter as CW and PW respectively. The excitation source was tuned to overlap with the λ_{max} of the nanocomposites at 800 nm.

photothermal response of gnr-collagen nanocomposites. Both uncompressed and compressed NCs were positioned over the center of 15×50 mm sections of tissue (single-walled), and exposed to laser irradiation for 4 minutes at laser power densities ranging from 0.83 to 2.50 W/cm^2 to investigate NC response to laser exposure. The surface temperature at the center of the nanocomposite was recorded every 5 seconds using an IR camera (ThermaCAM PS60 from FLIR) during the laser exposure. These images were then analyzed and the maximum temperature at the nanocomposite surface was recorded. These conditions providing an initial screening of laser power densities and durations likely to result in welding based on observation that it is generally necessary to exceed 60°C for engendering a robust tissue weld[19]. All temperatures are displayed as mean ± one standard deviation from five independent experiments.

laser tissue welding technique and ultimate tensile strength. Ten-mm full thickness incisions were made at the center of 15×50 mm intestinal samples (single-

47

walled). The opposing sides of the incision were positioned in close proximity, and NCs were placed over the incisions and treated at varying laser powers, as shown in Figure 13. Only the compressed NCs were used for tissue welding due to the higher temperatures reached with these materials compared to uncompressed gels as determined during investigation of NC photothermal response.

The ultimate tensile strength of the tissue under tension was measured using a TA.XTPlus Texture Analyser (Texture Technology Corp.) and Exponent software (Stable Microsystems). Each end of the rectangular tissue sample was held by pneumatic clamps and pulled apart at a rate of 1 mm/s until the tissue reached failure. The maximum force (F) and cross-sectional area of the tissue sample (A) determined the ultimate tensile strength (σ, kPa) of the welded tissue ($\sigma = F/A$). Intact intestine (no central incision) was also tested to establish an ultimate tensile strength for native tissue. All tensile strengths are displayed as mean $\pm$ one standard deviation from three to five independent experiments.
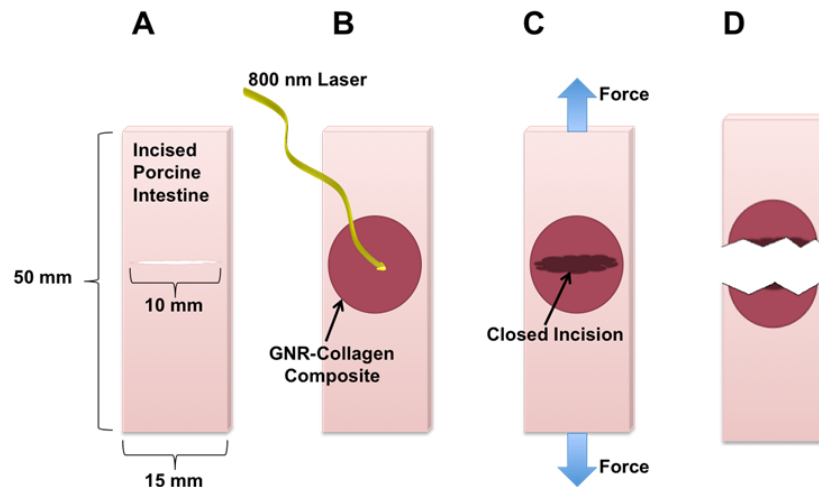
Figure 13. Schematic of laser tissue welding and tensile strength testing. (A) Porcine intestine is cut to 50 mm in length and 15 mm in width, with roughly 2 mm thickness. An incision is made through the intestine that is 10 mm in length. (b) A 15 mm diameter GNR-

Collagen composite is placed over the 10 mm incision and irradiated at 800 nm (near infrared wavelength). (c) The heat generated during irradiation causes protein interdigitation, closing the incision. Tension is applied to the tissue. (d) The tissue is pulled apart, and the ultimate tensile strength is measured.

leak and burst pressure measurements. Fifteen-cm length cylindrical sections of intestine were prepared with a 10-mm incision through and through to one wall. The opposing edges of the incision were maintained in close proximity, and a compressed NC was placed over the top of the incision site. The wound site was then treated with CW or PW laser at 2.33 or 2.50 W/cm^2 for 8 or 10 minutes. These conditions correspond to the greatest returns in ultimate tensile strength of the tissue. Following closure of the incision through laser irradiation, the intestine was closed on both ends using clips and filled with a saline solution using a small needle at a flow rate of 7.5 mL/min until bursting. A DPI 795 digital manometer (Druck) assembled in parallel to the saline flow recorded pressure within the intestinal sample, as shown in Supporting Figure S2.3. Leakage was defined as the point at which drops of saline were grossly seen, and bursting was at the maximum recorded pressure reached. The changes in pressure from the initiation of the experiment to the leakage and bursting points were recorded. Compressed NCs which had dried in an oven at 37°C overnight were also tested to minimize NC contraction during welding. All pressure changes are reported as mean ± one standard deviation from three to twelve independent experiments.

statistical analysis. A three fixed factor analysis of variance (ANOVA) was used to determine statistical significance ($p<0.05$) for photothermal response, ultimate tensile strength, and leak/burst pressure with the factors laser time, laser power density, and laser

type (CW or PW). All modeling was perform by Ms. Madaline Mushaben at Montana State University using the experimental data which I provided.

Results and Discussion

nanocomposite characterization. GNR-collagen NCs were synthesized as compressed or uncompressed hydrogels. The uncompressed gels were 12 mm in diameter and ~10 mm in height, and the compressed gels were also 12 mm in diameter but ~1 mm thick. No significant change in the GNR absorbance maxima (λ_{max}) occurred between the GNR dispersions and the GNR-collagen composites, and no significant change in λ_{max} occurred as the GNR wt% varied from 1 to 10%. The scanning electron microscopy (SEM) images   in
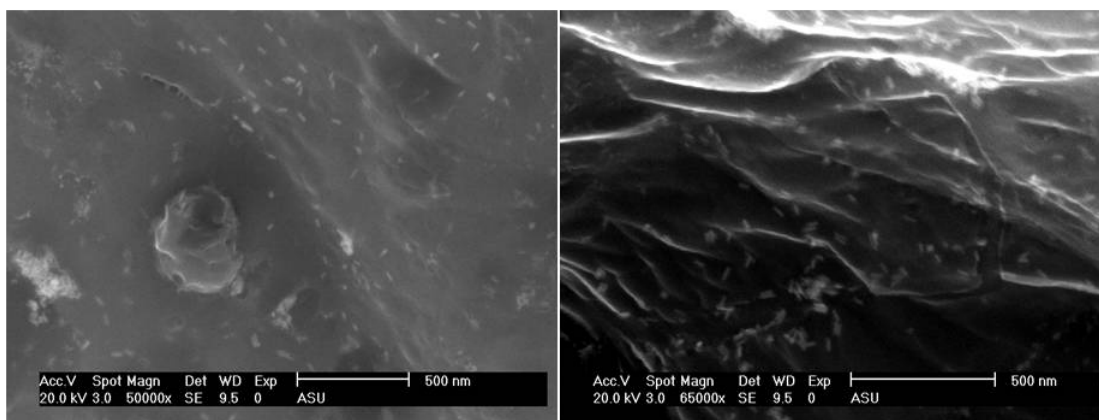
Figure *14* indicate that the GNRs were well distributed within the collagen gels.

Leaching of GNRs can diminish the photothermal response of the nanocomposites. Thus, nanocomposites with various GNR concentrations were incubated in a saline solution at 37°C and stirred at 100 rpm. Loss of GNRs was monitored using absorption spectroscopy. No significant nanoparticle leaching was observed for any GNR wt% tested over a 60-day period, as shown in Supporting Figure S2.4. This suggests that once the

GNRs bind collagen and/or penetrate the gel by diffusion, they become physically entrapped in the collagen matrix.
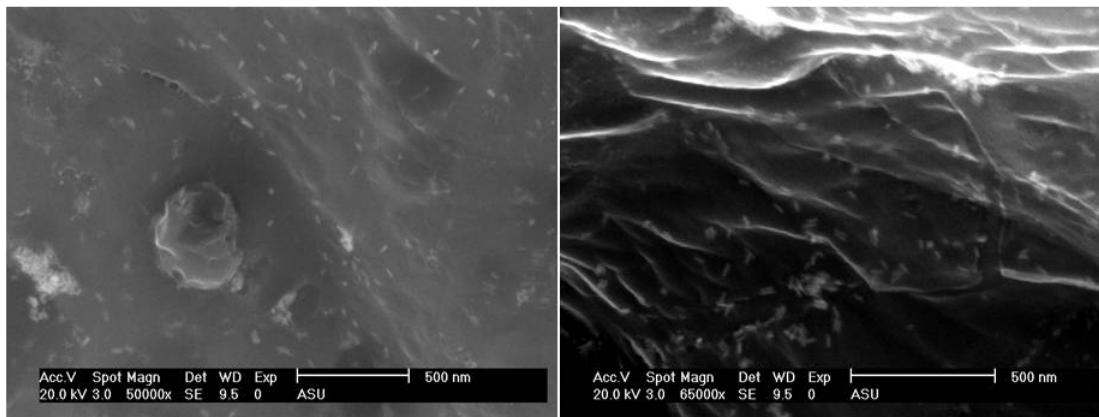
Figure 14. Scanning electron microscopy of GNR-Collagen nanocomposites. Environmental field emission-scanning electron microscopy (FE-SEM) images of 5 wt% Gold Nanorod-Collagen nanocomposites were acquired at an accelerating voltage of 20 kv. Individual nanorods are seen evenly distributed throughout the collagen matrix. Scale bare is 500 nm in both images, and nanorods are approximately 50 mm in length and 15 nm in diameter.

The swelling of the gels can influence the rate of heat transfer within the NC and rheological properties of the NC. The swelling ratios of the uncompressed NCs were 5 to 9 times higher than those of the compressed NCs. The expulsion of fluid content as a result of the compression also allowed for easier manipulation and storage of the NCs. NC swelling decreases as GNR concentration increases for compressed NCs, and significant changes in swelling are not seen for GNR concentrations above 5 wt% (Figure 15). Consequently, NCs with 5 wt% GNRs were subsequently used to minimize both swelling and nanoparticle concentration.
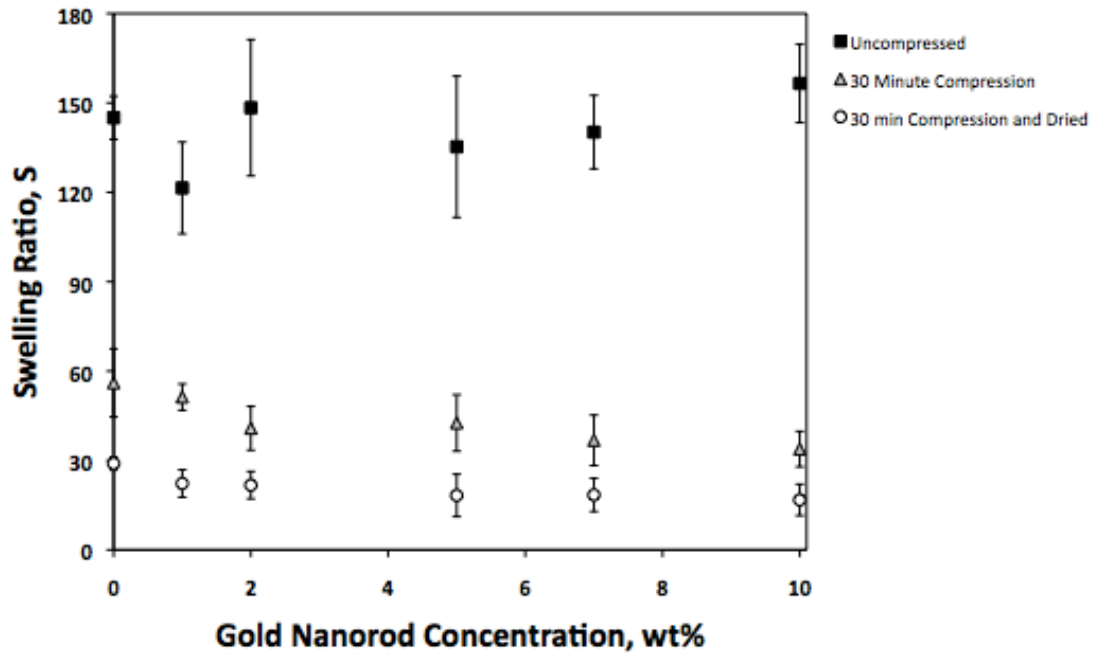
Figure 15. Swelling behavior of GNR-Collagen nanocomposites. Swelling ratios of compressed and uncompressed GNR-collagen nanocomposites as a function of GNR weight percent in the nanocomposite. Please refer the text for experimental details. n=3 experiments.

rheological behavior. The absolute shear modulus and loss angle of the NC solders are important considerations for application in load-bearing functions and also serve to minimize the interfacial mismatch with the tissue. These rheological characteristics were determined for uncompressed and compressed collagen with and without GNRs. Figure 16A and C show that compressing the collagen gels increased the shear modulus by as much as two-fold. This increase in stiffness is a result of removal of the excess fluid present due to gel casting(Abou Neel, Cheema, Knowles, Brown, & Nazhat, 2006). In addition, NC shear modulus increased greatly with frequency, suggesting that the material is able to absorb stress(Y. Yang & Kaufman, 2009) under load-bearing applications. While

significant, only a very small change occurred in shear modulus for gels with GNR content between 0% and 5% by weight. It is likely that the effect of GNRs on the crosslinking and stiffness of the collagen network is minimal, since the nanoparticles were introduced to the gel system following fibrillogenesis.

All collagen gels and GNR-collagen NCs tested under frequency sweep displayed predominately elastic behavior, as shown by loss angles below 45° (loss tangent <1) in Figure 16B and D. Loss angle varied significantly with compression, GNR presence, and frequency. The addition of GNRs increased the elasticity of the collagen matrices at low frequencies, while matrices without GNRs were more elastic at high frequencies.

Rheological studies carried out under a wide range of temperatures facilitate a deeper understanding of the behavior of NCs at physiological as well as elevated temperatures that are induced during LTW operation. The temperature sweep results in Figure 16C illustrate that temperature, GNR content, and compression significantly change the shear modulus of NCs. Figure 16D shows that the loss tangent of NCs was a function of temperature, which is in agreement with previous observations on temperature dependence of collagen elasticity(Misof, Rapp, & Fratzl, 1997). A significant decrease in shear modulus and loss tangent occurred in all cases between 50°C and 60°C (Figure 16C and D).
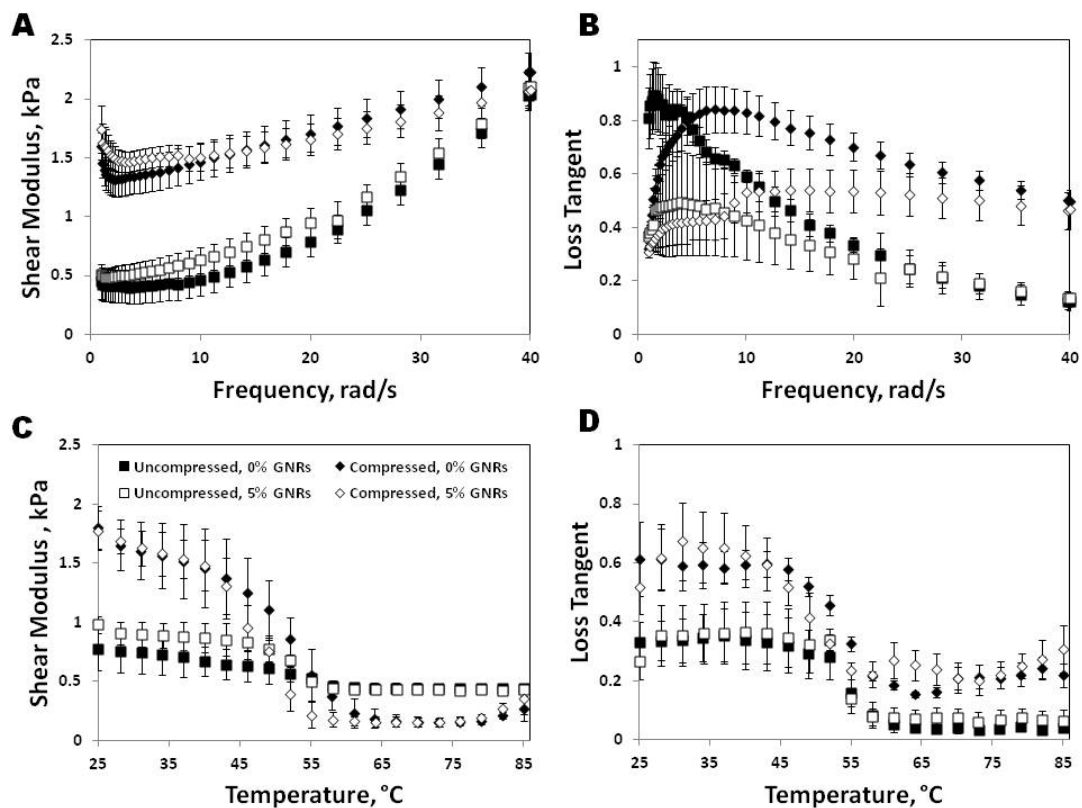
Figure 16. Shear modulus and loss tangent of GNR-Collagen nanocomposites. Uncompressed and compressed nanocomposites in the absence and presence of gold nanorods (5 wt%) where (A) shear modulus is a function of frequency, (B) loss tangent is a function of frequency, (C) shear modulus is a function of temperature, and (D) loss tangent is a function of temperature. The corresponding symbols in (C) are applicable for all four panes. n=5 experiments.

photothermal response of gnr-collagen nanocomposites. It is generally necessary to exceed 60°C for engendering a robust tissue weld(H.-C. Huang et al., 2013c). Other studies have shown that uniform heating of the tissue through the full thickness results in greater weld strength(Bilici, 2010b), although these high temperatures can potentially damage peripheral tissue. It is therefore advantageous to optimize the trade-off

between weld strength and heat generation during LTW operation. The role of laser parameters and material parameters on photothermal properties of GNR-collagen nanocomposites were then investigated. Laser parameter studies include power density, exposure time, and wave type, while material parameter studies include collagen concentration, gel compression time, and GNR wt% in the nanocomposite. Laser parameters were studied for 5 wt% GNR-collagen NCs (~2 mg). Each composite was placed at the center of a section of intact intestine, and irradiated for four minutes.

Figure 17 and Figure 18 show the kinetics of temperature rise of GNR-collagen gels exposed to NIR light at power densities from 0.83 to 1.83 W/cm^2 over time; the temperature response was determined using NIR thermal imaging. The increase in temperature is proportional to the power density of the laser radiation. Heat generation occurred rapidly but approached an upper limit, such that 50% of the total temperature increase occurred within the first 30 seconds of each treatment. Intact intestine alone (no NC) exposed to 1.83 W/cm^2 PW or CW laser results in only an 8°C increase in temperature over basal levels, not even reaching physiological temperature. These results show that the tissue absorption of NIR laser light, and concomitant temperature increase are minimal, which necessitates the use of photothermal biomaterials like GNR-collagen nanocomposites.
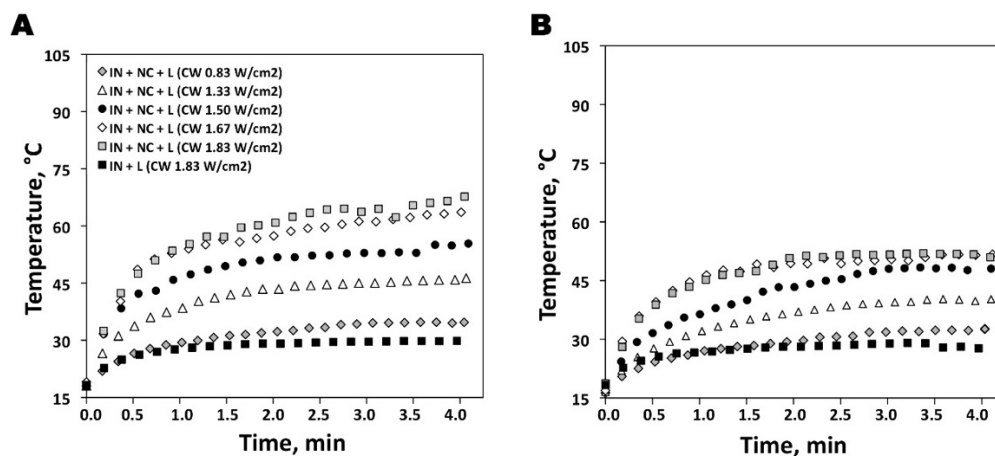
Figure 17. Photothermal response of uncompressed nanocomposites. Temperature responses of uncompressed nanocomposites (NCs) following exposure to (A) continuous wave (CW) and (B) pulsed wave (PW) laser radiation were determined using thermal imaging. The power densities employed are indicated in the legend for CW laser, and the corresponding symbols are applicable to PW laser as well. Each curve is a representative curve from a sample of five independent experiments.

Compressed NCs demonstrated higher efficacies for photothermal conversion compared to uncompressed NCs as indicated by significantly higher temperatures under conditions of similar laser treatments (Figure 17 and Figure 18). Treatment at 1.83 W/cm^2 CW resulted in temperatures greater than 60°C within three minutes for uncompressed NCs, while in no cases did the PW treatments facilitate a temperature rise greater than 60°C. In contrast, treatments with laser powers as low as 1.33 W/cm^2 CW and 1.50 W/cm^2 PW resulted in temperatures in excess of 60°C for compressed NCs. Greater temperature rise in compressed NCs is likely due to closer GNR proximity and decreased water content.

In general, CW irradiation resulted in greater temperatures than those obtained with PW irradiation.
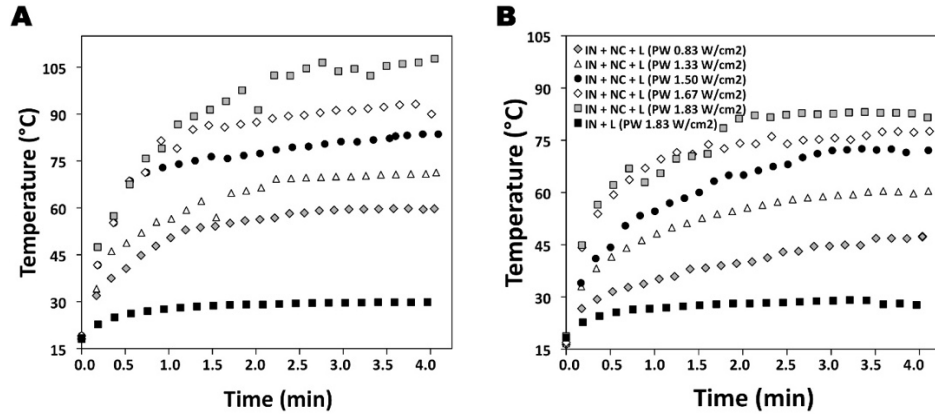
Figure 18. Photothermal response of compressed nanocomposites. Temperature responses of compressed nanocomposites (NCs) following exposure to (A) continuous wave (CW) and (B) pulsed wave (PW) laser radiation were determined using thermal imaging. The power densities employed are indicated in the legend for the PW laser, and the corresponding symbols are applicable to CW laser as well. Each curve is a representative curve from a sample of five independent experiments.

The above results suggest that power densities below 1.33 W/cm^2 will likely not result in temperatures sufficient to create robust tissue fusion (>60°C). It is also likely that these temperatures are elevated compared to the wound bed temperature because the temperatures recorded were at the NC surface. For these reasons, subsequent strength and bursting studies were performed at a laser power density of 1.67 W/cm^2 or higher.

laser tissue welding ultimate tensile strength. GNR-collagen nanocomposites were then investigated for laser-facilitated welding of ruptured porcine intestinal tissue. Ultimate tensile strength is a rapid first-pass indicator of tissue bonding efficacy(Bilici,

2010b)·(Chivers, 2000)·(J. D. Cezo, Passernig, Ferguson, Taylor, & Rentschler, 2014b) for welded tissue (Figure 19). All ruptured intestine (RI) samples failed at the site of incision, while intact intestine (IN) samples failed at the site which was held together by clamps. During laser treatment, the NCs contracted, and the nanocomposite solder could not always be maintained at the same location. This, in turn, likely influenced the variance observed in the ultimate tensile strengths between experiments(Steinstraesser et al., 2010b).
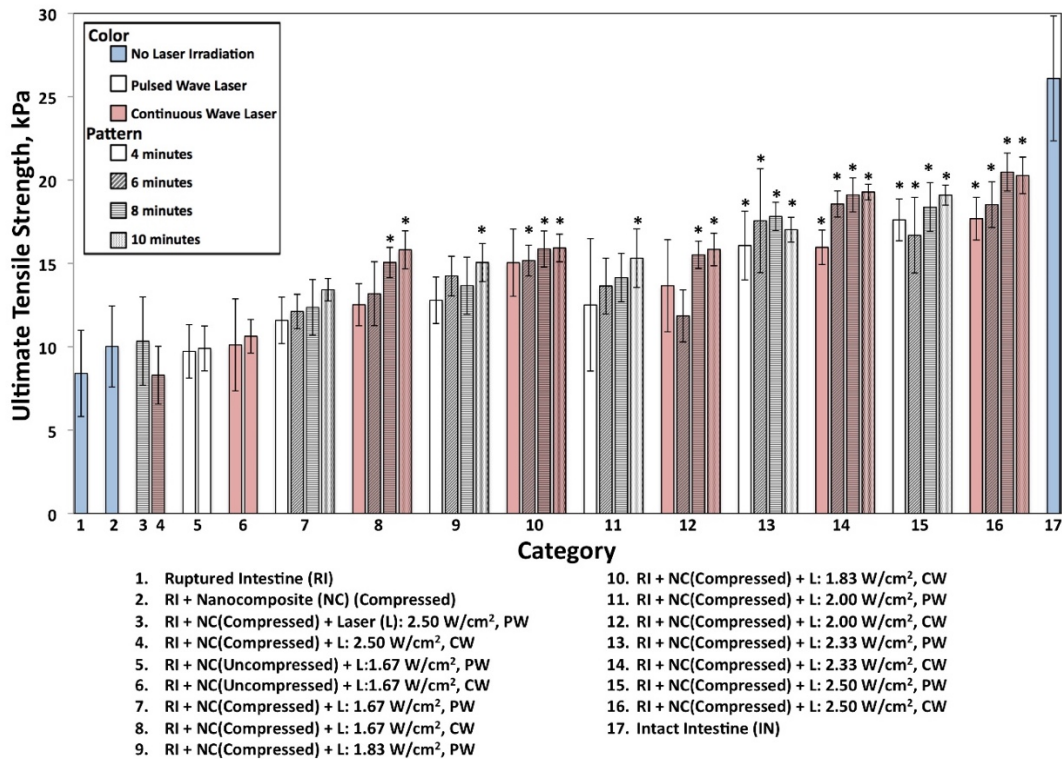
Figure 19. Tensile strength of laser tissue welded ruptured intestines. GNR-collagen nanocomposites (NC), 5 wt% by GNRs, were applied to ruptured intestines (RI) at various laser (L) power densities for pulsed wave (PW) or continuous wave (CW) laser, shown by white and red bars, respectively. Treatment durations were for 4 minutes (no pattern), 6 minutes (diagonal lines), 8 minutes (horizontal lines), and 10 minutes (dots). RI and intact intestine (IN) sample groups that were not exposed to laser are represented in blue. A

maximal UTS recovery of 68% was seen in cases of welded ruptured intestine (RI) compared to the intact intestine (IN). Please refer to the text for experimental details. Asterisks represent treatment groups whose mean is statistically significant ($p < 0.05$) from the mean of the RI control group. $n \geq 3$ experiments.

The ruptured intestine had an ultimate tensile strength (UTS) of 8.40 ± 2.59 kPa, while the strength of intact tissue was 26.10 ± 3.75 kPa. The strength of the ruptured intestine treated with the GNR-collagen NC alone (no laser) was 10.02 ± 2.43 kPa, which was not significantly different from that of the ruptured intestine. The UTS values of the ruptured intestine subjected to continuous and pulsed wave lasers (2.50 W/cm^2 for 8 minutes; no NC employed) were 8.30 ± 1.73 kPa and 10.34 ± 2.65, which were also not dissimilar from that observed for the ruptured intestinal tissue. These results indicate that laser alone or nanocomposite alone fail to restore the mechanical properties of the ruptured intestine.

LTW treatments with GNR-collagen nanocomposites ranged from power densities of 1.67 W/cm^2 for 4 minutes to 2.50 W/cm^2 for 10 minutes. Laser welding resulted in recovery of the UTS, and Figure 19 shows the conditions under which the UTS is significantly different for the LTW treatments compared to the ruptured intestine control group (marked with asterisks). The lowest significant change in UTS (15.06 ± 0.91 kPa or 37.6% return from ruptured intestine) occurred at a laser power density of 1.67 W/cm^2 CW irradiated for 8 minutes. Treatment with a CW laser power density of 2.50 W/cm^2 for 8 minutes resulted in the highest UTS recovery under the conditions tested, at 20.48 ± 1.14 kPa or a 68.3% return in tissue tensile strength. It is noteworthy that at lower power densities of 1.67, 1.83, and 2.00 W/cm^2, only longer treatments resulted in significant

improvements in UTS of the ruptured tissue. In contrast, at power densities of 2.33 and 2.50 W/cm^2, all treatment times resulted in significant increases in UTS for both continuous and pulsed wave lasers. In general, UTS increased with increasing laser power and duration.

Treatment with pulsed wave (PW) lasers resulted in lower UTS values than similar treatment using continuous wave laser in select cases. For example, in case of laser treatments with power densities of 2.33 W/cm^2 for 10 minutes, the UTS was 19.28 ± 0.47 and 17.02 ± 0.74 kPa for CW and PW respectively. The increase in weld strength resultant of CW laser is likely a result of the greater photothermal response for this treatment compared to that observed for PW treatments. However, in the majority of the treatment groups studied, the difference in UTS between CW and PW treatments is insignificant. One such example is at treatment with a laser power density of 2.50 W/cm^2 for 10 minutes, which was the highest power and longest duration employed. The CW group resulted in 20.28 ± 1.09 kPa UTS, while the PW treatment resulted in a UTS value of 19.10 ± 0.60 kPa ($p>0.05$). These results suggest that both CW and PW lasers may be employed for LTW operation. Peripheral thermal damage may be minimized using PW radiation if the pulse duration is less than the thermal relaxation time of the tissue, leading to heat diffusion outside the area of laser exposure and tissue cooling between pulses(Sriramoju & Alfano, 2011a)(Karamzadeh, Wong, Crumley, & Ahuja, 2004).

The above results indicate that the ultimate tensile strength of the welded tissue is higher for conditions that result in higher temperature (greater photothermal response) during the LTW operation. As mentioned previously, temperatures exceeding 60°C result in a greater likelihood of protein fusing, leading to a better tissue seal. A comparison of

Figure 18 and Figure 19 shows that significant return in UTS occurred only at conditions where the NC surface temperature exceeded 85°C within four minutes of laser exposure. It is likely that the wound bed likely requires sustained surface temperatures greater than 60°C to yield significant tissue bonding, although the temperature directly beneath the NC at the actual weld site was not easily measured without disrupting the treatment,

While standard suturing recovers as high as 60% of the tensile strength of the tissue(Poppas et al., 1996), returns in tensile strength as high as 68.3% at very low power densities and moderate exposure times suggest that LTW with GNR-collagen NCs can become comparable to conventional suturing with the potential benefit of rapid hydrosealing. Other groups have even shown that the UTS values of LTW treated tissue are higher than those from conventional suture techniques(Bilici, 2010b).

leak and burst pressure of welded tissue. While tensile strength is a useful first measure of tissue bonding, a critical parameter necessary to determine the success of a tissue seal is the ability to prevent fluid leakage from the lumen following treatment. Leak and burst pressure studies, both of which are common benchmarks for comparing fluid-tight tissue closure(B. S. Bleier, 2010b)'(Garcia et al., 2009b), were both carried out following LTW with GNR-collagen nanocomposites. 5 wt% GNR NCs were placed over a full-thickness 10-mm incision made in porcine intestine and irradiated with laser at different intensities and durations. Cylindrical sections of welded intestines were clamped at the ends and slowly filled with saline until bursting was grossly observed. A laboratory-developed manometer (Supporting Figure S2.3) measured leak and burst pressures immediately following laser treatment. The leak pressure was recorded as the pressure at which drops of saline were first grossly observed leaking from the welded intestinal

sample. The burst pressure was defined as the maximum pressure recorded, which was often associated with a visible and sharp burst of the tissue. Figure 20 demonstrates that intact intestines had significantly different leak and burst pressures (4.914 ± 0.540 psi and 7.586 ± 0.895 psi respectively); leakage occurred at the needle insertion point for all intact intestine samples, while bursting did not always occur at the point of needle insertion. For all other samples tested, leakage occurred at the maximum pressure recorded. In addition, for all ruptured intestinal samples, leakage and bursting were observed at the incision site. For untreated ruptured intestine, these pressures were negligible (0.040 ± 0.038 psi).

Color
- No Laser Irradiation
- Pulsed Wave Laser
- Continuous Wave Laser

Pattern
- 6 minutes
- 10 minutes

1. Ruptured Intestine (RI)
2. RI + Nanocomposite (NC) (Undried)
3. RI + Laser (L): 2.50 W/cm², 10 min
4. RI + NC(Undried) + L: 2.33 W/cm², 6 min
5. RI + NC(Undried) + L: 2.33 W/cm², 10 min
6. RI + NC(Undried) + L: 2.50 W/cm², 6 min
7. RI + NC(Undried) + L: 2.50 W/cm², 10 min
8. RI + NC(Dried) + L: 2.33 W/cm², 6 min
9. RI + NC(Dried) + L: 2.33 W/cm², 10 min
10. RI + NC(Dried) + L: 2.50 W/cm², 6 min
11. RI + NC(Dried) + L: 2.50 W/cm², 10 min
12. Intact Intestine (IN) Leak Pressure
13. IN Burst Pressure

Figure 20. Leak and burst pressure of laser tissue welded ruptured intestine. Compressed 5 wt% GNR-collagen nanocomposites (NC) were applied to ruptured intestine (RI) at various laser (L) power densities for pulsed wave (PW) or continuous wave (CW) laser, shown by white and red bars, respectively. Treatment durations were for 6 minutes (no pattern) and 10 minutes (horizontal lines). NCs were undried (groups 4-7) or dried (groups

8-11). RI and intact intestine (IN) sample groups that were not exposed to laser are represented in blue. A maximal leak pressure recovery of 64% and burst pressure recovery of 42% was seen in cases of welded intestines compared to the intact intestine. Please refer to the text for experimental details. Asterisks represent treatment groups whose mean is statistically significant ($p<0.05$) from the mean of the RI control group. $n\geq3$ experiments.

No significant return in leak or burst pressure (<0.1psi) occurred as a result of application of the NC alone or laser treatment alone. These results further strengthen the conclusions that the NCs, by themselves, do not adhere strongly enough to the tissue to create a meaningful seal and that laser irradiation in the absence of GNR-collagen nanocomposite has negligible effect on tissue closure.

The effect of compressed nanocomposites on recovery of leak and burst pressure of the ruptured intestine following welding was next investigated. Both CW and PW laser treatments of the NC at the site of incision varied in laser power density and duration of exposure. The results of the UTS measurements allowed us to focus the fluid pressure testing to the most likely parameters to show successful welds. Pulsed wave laser exposure at 2.33 W/cm^2 for 6 minutes resulted in a leak/burst pressure of 0.445 ± 0.120 psi and increased to as high as 0.673 ± 0.146 psi at 2.5 W/cm^2 for 10 minutes of exposure. These pressures translated to only an 8% and 13% return in leak pressure, respectively, compared to the intact intestine. In general, increasing the laser power density from 2.33 to 2.50 W/cm^2 and increasing the duration of exposure from 6 to 10 minutes did not significantly improve the sample fluid pressure (Figure 20). In addition, no significant difference was found in the pressures of intestines irradiated with CW and PW laser.

One difficulty in performing welds under the above conditions was that the 12-mm diameter nanocomposites placed over the 10-mm incisions were observed to contract during laser exposure. The possibility of the incision not being completely covered could be overcome through NCs with larger surface area, using multiple NCs during treatment, or decreasing NC contraction by decreasing water content through desiccation. Larger nanocomposites and multiple nanocomposites were not used to minimize the amount of GNRs used in treatment. Instead, the NCs were dried in an oven at 37°C overnight resulting in the expulsion of water from the nanocomposite. This was hypothesized to limit NC contraction and therefore facilitate greater fluid-tight closure of the ruptured tissue. These welding experiments resulted in much higher fluid pressures, beginning at 1.535 ± 0.108 psi (20% and 31% return in leak and burst pressure compared to intact intestine) for samples treated with 2.33 W/cm^2 PW laser for 6 minutes, and reaching up to 3.176 ± 0.162 psi, or 64% and 42% recovery in leak and burst pressure, at 2.50 W/cm^2 PW laser for 10 minutes. As a general trend, resultant fluid pressures increased with increasing exposure time and increased laser power density. However, no significant difference in fluid pressures occurred between samples irradiated with CW or PW laser at the same conditions.

To the best of our knowledge, 2.33 and 2.50 W/cm^2 are among the lowest laser power densities ever shown to result in a significant return in tissue burst pressure using laser tissue welding. In fact, 2.50 W/cm^2 is an eight-fold decrease in laser power density from our previous work using elastin-like polypeptide (ELP)-based NCs for laser tissue welding(H.-C. Huang et al., 2013c). In addition, treatment durations of 6 or 10 minutes are comparable those found in the literature. The type of laser employed - pulsed or continuous

wavelength - did not significantly alter the burst pressures, which differed from observations with the photothermal response of the NCs and ultimate tensile strength measurements of the welded tissue. This suggests that pulsed laser irradiation can bond tissue while mitigating heat generated and potentially minimize peripheral thermal damage(Bilici, 2010b)'(Sriramoju & Alfano, 2011a)'(Ratto et al., 2009b). LTW surface temperatures likely remain lower during pulsed wave treatments because the tissue can cool between incident pulses, and the tissue thermal relaxation time is greater than the pulse duration. Through modulated laser irradiation, heat generation within and heat transfer outside of the area of exposure can be limited.

While these results suggest that increased power and exposure length could further improve the burst pressure, burst pressure is not the only measure of successful laser tissue welding. Limiting the treatment time has large clinical importance, and limiting the laser power also limits the temperatures reached in welding. It is unclear at this time pending *in vivo* experiments whether these factors will impact the viability of the tissue and ultimately healing.

Conclusions

In this study, gold nanorod-collagen plasmonic nanocomposites for NIR laser-facilitated welding of ruptured porcine intestine were generated. The photothermal response of both uncompressed and compressed nanocomposites, and also the role of femtosecond pulsed and continuous wavelength lasers, laser power, and laser duration on the nanosolder photothermal response were investigated. In general, irradiation of NCs with continuous wavelength laser resulted in higher temperatures compared to those obtained with pulsed wavelength laser. Laser welding studies indicated that NCs

significantly enhance the ultimate tensile strength of ruptured porcine intestine at relatively low exposure times and power densities. NC-facilitated welding significantly restored the leak and burst pressures of ruptured intestines, and both laser types resulted in similar performances. These nanocomposite solders will continue to improve with the aid of real-time photothermal response imaging and further optimization of heat transfer and localization at higher power densities, longer exposure times, and increased nanoparticle concentration. It is anticipated that development of promising photothermal biomaterials will result in laser tissue welding becoming a viable option for surgery, especially in cases of friable or difficult-to-reach tissue, postoperative leakage, or infection. Future work will involve the use of *in vivo* models to better ascertain the efficacy of welding/sealing, extent of thermal damage as a function of laser power, exposure duration, area of application, effect of the nanocomposite on tissue healing, and temperatures induced during treatment.

SPATIOTEMPORAL MODELING OF LASER TISSUE SOLDERING

USING PHOTOTHERMAL NANOCOMPOSITES

Introduction

Sutures are a ubiquitous part of surgery, with approximately 90 million surgical incisions requiring closure each year in the U.S. and 3 million stitches placed daily around the world(Tajirian & Goldberg, 2010b). Sutures and staples, however, do not provide an immediate seal to the tissue and, additionally, cannot functionally repair tissues in some cases(Lauto, Mawad, & Foster, 2008c). The ability to rapidly seal ruptured or incised tissue has the potential to decrease infection, leakage, reduced scarring, and healing time compared to suturing(H.-C. Huang, Walker, Nanda, & Rege, 2013d; Hyman, Manchester, Osler, Burns, & Cataldo, 2007; Park, 2010b). Tissue sealants, adhesives, and glues have thus far been limited in their application and ability to rapidly seal tissue reproducibly, especially when bearing a load(B. S. Bleier, Cohen, Bloom, Palmer, & Cohen, 2010; Komatsu, Mori, & Uchio, 2006). Surgical glues have wide use in topical applications, but, due to long polymerization times and toxicity concerns, glues have seen very limited internal use, especially in wet wound environments(Duarte, Coelho, Bordado, Cidade, & Gil, 2012b). Recently developed nanoparticle solutions have been shown to provide rapid adhesion between two hydrogels. The method relies on the nanoparticle adsorbing onto polymer gels to connect the polymer chains(Meddahi-Pelle et al., 2014; Rose et al., 2014b).

Alternatively, laser tissue soldering (LTS) is a rapid tissue sealing technique in which a chromophore converts laser light to heat. This heat induces structural changes in the native tissue and/or biomaterial "solder" leading to a tissue seal through photocoagulation and protein interdigitation (Figure 21)(Barak et al., 1997; B. S. Bleier,

Palmer, Sparano, & Cohen, 2007b; Foyt, Johnson, Kirsch, Bruce, & Wazen, 1996). The laser-absorbing chromophore may be a native tissue constituent or an exogenous material injected or applied to the surgery site. Native chromophores, including water, melanin, and hemoglobin(Paolo Matteini, Ratto, Rossi, & Pini, 2012b) are present in significant amounts within tissues, and have the advantage of eliciting no foreign body response. However, efficient light absorption by these chromophores prevents deep laser penetration which, in turn, can lead to extensive superficial heating but limited heating in deep tissues(F. Rossi et al., 2005). Endogenous chromophores have therefore been extensively studied in thin, transparent, and homogenous tissue, but have been minimally effective in sealing larger tissue geometries(Ratto et al., 2009c).

To overcome these challenges, exogenous chromophore formulations have been used as stains(Paolo Matteini, Sbrana, Tiribilli, & Pini, 2009; Ratto et al., 2009c), pastes(B. S. Bleier et al., 2007b), or patches(H.-C. Huang et al., 2013d; Urie, Quraishi, Jaffe, & Rege, 2015c) in concert with lasers tuned to near infrared wavelengths, at which laser absorbance in the tissue is higher compared to light at visible wavelengths. Tissue stains using aqueous solutions of the organic dye indocyanine green (ICG), and tissue solders largely composed of albumin-ICG viscous liquids or semi-solids have been used. These chromophores work effectively at differentiating laser absorbance from that of the tissue, but organic dyes lack long-term stability and often leach to peripheral tissue(Hoffman, Byrd, Soller, Heintzelman, & McNally-Heintzelman, 2003b). Simultaneously, viscous solders have been criticized for difficulty with reproducing robust soldering with consistency(C. B. Bleustein, Walker, Felsen, & Poppas, 2000; Garcia et al., 2009c; Lauto et al., 2008c).

Plasmonic nanoparticles, including gold nanorods, are inert and stable, easily modified, and convert laser light to heat approximately a million-fold more effectively than organic dyes(Hoffman et al., 2003b), although there are some cytotoxity and bio-elimination concerns(Almeida, Chen, Foster, & Drezek, 2011; Lewinski, Colvin, & Drezek, 2008). The LTS approach of interest here is based on nanocomposite solders composed of gold nanorods (GNRs) cross-linked or embedded within a polypeptide matrix. In the former case, elastin-like polypeptides (ELP) were crosslinked with GNRs, resulting in the formation of thin film patches(H.-C. Huang et al., 2013d), and, in the latter case, collagen hydrogels were physically embedded within GNRs and compressed plastically to form thin film hydrogel patches(Urie et al., 2015c). ELP-GNR nanocomposites successfully soldered *ex vivo* porcine intestine in a 47% return in tensile strength and a 45% return in burst pressure compared to intact intestine, and collagen-GNR nanocomposites similarly resulted in a 68% return in tensile strength and a 42% return in burst pressure compared to intact intestine. The extent of laser absorption in these nanocomposites depends on the wavelength of the laser and the absorbance of the chromophore. Gold nanorods tuned to a maximum absorbance at 800 nm were selected because light is minimally absorbed by water and tissue constituents in this therapeutic window(H.-C. Huang, Rege, & Heys, 2010c). In this work, collagen-GNR nanocomposite hydrogels are used in conjunction with 800 nm NIR laser to solder ruptured porcine intestine.

In addition to tensile strength and burst pressure, the temperature reached during soldering is paramount in establishing the integrity of the solder(H.-C. Huang, Nanda, & Rege, 2012b) while also mitigating tissue damage. Thermal denaturation of collagenous

69

tissue is proposed to follow a three-step mechanism(L. Bass et al., 1992; Paolo Matteini, Cicchi, et al., 2012a; Schober, Ulrich, Sander, Durselen, & Hessel, 1986), which illustrates the temperature range necessary for forming new tissue bonds. First, at approximately 45°C, interfibrillar bridges are broken and the parallel collagen fibril arrangement is impaired. Second, around 60°C intramolecular hydrogen bonds are broken, and the fibrillar edges are frayed. Finally, at 80°C, the covalent bonds within and between collagen molecules are broken, leading to full denaturation, and the tissue becomes homogenized. From this proposed mechanism and previous studies in laser tissue soldering, it has been seen that the optimal temperature window for tissue bonding is between 60-67°C(Sl Jacques & Prahl, 1987; Paolo Matteini, Sbrana, et al., 2009). However, healthy, living cells heated to these same temperatures will be damaged or killed by hyperthermia(Paolo Matteini, Ratto, et al., 2009c). One promising approach for minimizing health cell damage by hyperthermia is the development of micro-particles containing GNRs and superparamagnetic particles agglomerated in a layered polyelectrolyte multilayer matrix. Magnetic particle guidance can be used to enriched the particles in the tissue incision for wound sealing, and the results show damaged areas of less than 100 microns of tissue(He, Frueh, Hu, et al., 2016; He, Frueh, Shao, et al., 2016).

The development of a spatiotemporal model of heat transfer and cell death is motivated by the goal of identifying the optimal conditions for performing laser tissue soldering to help mitigate damage to nearby healthy cells while maximizing solder integrity. A mathematical model of heat transfer and cell death proximal to the nanocomposite and in nearby tissue is described here with the objective of accelerating the identification of optimal LTS treatment parameters. Effective integration of mathematical

modeling with laser solder operation can potentially reduce the overall number and duration of experimental trials and improve outcomes for tissue repair by minimizing healthy tissue damage. Most mathematical modeling of laser-tissue interactions has focused on the heating and coagulation of tissue, not the fusing of tissue, and has not included an exogenous chromophore or solder material. Model predictions of tissue temperatures are important because it is difficult to measure the temperatures reached below the treatment surface during LTS, especially in larger tissue geometries where LTS has had less success. This model is validated using porcine intestine and murine colon experimental results.
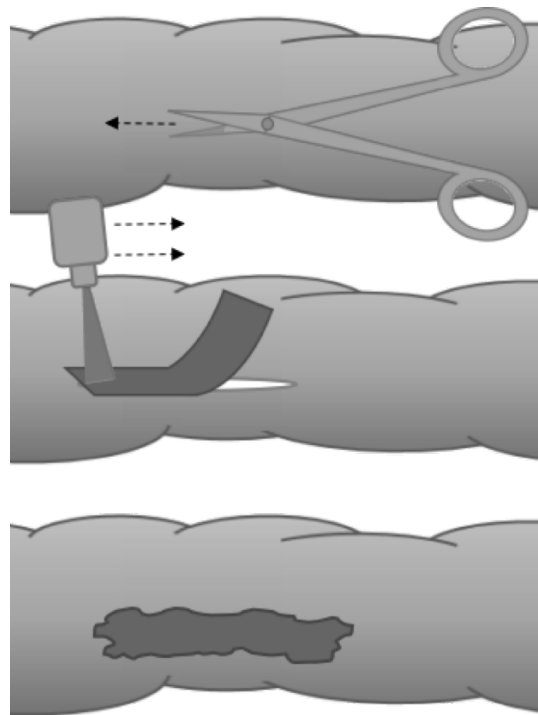
Figure 21. Schematic of laser tissue welding ruptured intestine. The incision of colon tissue (TOP) after the incision is closed using a photo-responsive nanocomposite (center) and laser irradiation to create a rapid, robust seal (BOTTOM) through laser tissue soldering.

Methods

nanocomposite synthesis. Collagen-gold nanorod (GNR) nanocomposites were generated based on methods previously described by us(H.-C. Huang et al., 2008, 2012b, 2010c, 2013d). Briefly, gold nanorods (GNRs) with a maximum absorbance at 800 nm were synthesized using the Nikoobakht seed-mediated method(B. Nikoobakht & El-Sayed, 2003). GNRs were then centrifuged repeatedly and redispersed in nanopure water to a final cetyltrimethylammonium bromide (CTAB) concentration below 0.25mM. Nanorods were dispersed in 4 mg/mL rat tail type 1 collagen at a concentration of 5 wt% GNRs. These collagen-GNR dispersion solutions were brought to neutral pH while on ice and aliquoted into a 48-well plate (12 mm diameter wells). The well plate was kept at 30°C for 1-3 hours to allow the collagen solutions to gel. The resultant gels were roughly 10 mm thick. A hollow cylindrical weight filled with absorbent tissue paper was use to compress the gels and remove excess liquid until the gels were < 1 mm in thickness.

laser configuration. A titanium sapphire laser pumped by a solid-state laser (Spectra-Physics, Millennia) was configured in the following manner: a 2 mm-diameter beam was passed through a cylindrical lens, and the subsequent laser light was screened by small mask with an approximately 0.5 mm x 3 mm opening to adjust the area of exposure to 2 mm x 15 mm at the focus length to simultaneously irradiate the entire portion of the nanocomposite patch covering the wound site (~30 mm^2 area). The laser was tuned to the maximum absorbance of the collagen-GNR nanocomposites, 800 nm.

laser soldering of porcine intestinal tissue. The effectiveness of the laser tissue solder has been previously demonstrated through measuring the tissue burst pressure and tensile strength after soldering. Intestinal porcine tissue was defrosted in water and kept moist at 20°C. First, a 1-cm incision is made through one wall (~2mm thick) of a section

of intestine at the tissue center. The tissue was laid flat on a plastic surface, the incision edges were approximated, and a nanocomposite was placed over the incision(H.-C. Huang et al., 2013d). An infrared (IR) camera (ThermaCAM PS60 from FLIR) was placed directly above the tissue and nanocomposite configuration to capture top-down IR images for recording a 2D array of surface temperatures. The center of the nanocomposite corresponding to the incision area was then irradiated at power densities from 0.83 to 2.33 W/cm^2 for up to 8 minutes. IR images were recorded every 5 seconds during the laser irradiation. Additionally, a Digi-Sense J-type thermocouple (~1.75 mm diameter fiber) was placed directly below the tissue under the center of the nanocomposite. The thermocouple temperature was recorded every 15 seconds. It should be noted that the temperature of individual nanoparticles is higher than the regional thermocouple temperature measurements reported here(Jauffred, Taheri, Schmitt, Linke, & Oddershede, 2015; Ruijgrok, Verhart, Zijlstra, Tchebotareva, & Orrit, 2011; Shao et al., 2015; Xuan et al., 2016).

To compare wound patency, the section of sealed intestine was clamped at both ends and infused with a dyed saline solution until bursting, measuring the maximum internal pressure to determine how much of the native tissue strength was recovered by soldering. A DPI 795 digital manometer (Druck) was placed in parallel to the flow of the dyed saline. Using this manometer, pressure within the intestinal sample was measured. Burst pressure was defined as the point at which the maximum pressure was reached. The change in pressure from the initiation of the experiment to the bursting point was recorded. A syringe pump (NE 300, New Era Pump Systems, Inc) first purged the line and hypodermic needle (26 gauge) for roughly 1 minute, at which point the pressure in the

system was constant and was zeroed using the manometer prior to the infusion line and needle being inserted into the intestine. The intestine section was clamped at both ends and filled with saline solution dyed with green food coloring at a flow rate of 0.5 mL/min using the syringe pump. The infusion continued until intestinal rupture.

The strength of the solder was also tested using rectangular slabs of approximately 50 mm length and 15 mm width of tissue with a soldered incision that was clamped at each end, and an increasing force was applied using a TA.XT Plus Texture Analyzer (Texture Technology Corp.) until failure, extended at a rate of 1 mm/s in uniaxial tension. This force on the tissue under tension was measured using the accompanying Exponent software (Stable Microsystems) to determine the ultimate tensile strength of the tissue by taking the maximum force normalized by cross-sectional area of the tissue.

laser soldering of intestinal tissue in mouse cadavers. Freshly euthanized C57BL/6 mouse cadavers were also used for evaluation of laser tissue soldering. A midline incision was made in each cadaver, and the colon was unpacked from the body cavity. The colon was folded over twice, as shown in Figure 22. While exact dimensions of the mouse colon are difficult to measure, the mouse colon is approximately 0.5 mm thick, as shown in Figure 22. The nanocomposite patch was partly wrapped around the colon. Similar to the porcine intestine, the IR camera was placed directly above the tissue-nanocomposite configuration to record surface temperature data during laser irradiation; however, unlike the porcine intestine, the thermocouple was arranged in one of three configurations, as shown in Figure 22. In one configuration, the thermocouple was inserted into the lumen of the primary section of colon tissue with internal contact on both intestinal walls, and temperatures were recorded. In a second configuration, the thermocouple was inserted in

74

between the primary and secondary colon tissue sections and in direct contact with both. In the final configuration, the thermocouple was inserted in the lumen of the secondary tissue similar to configuration one. In each configuration, the thermocouple was located directly below the nanocomposite that was being irradiated by the laser.
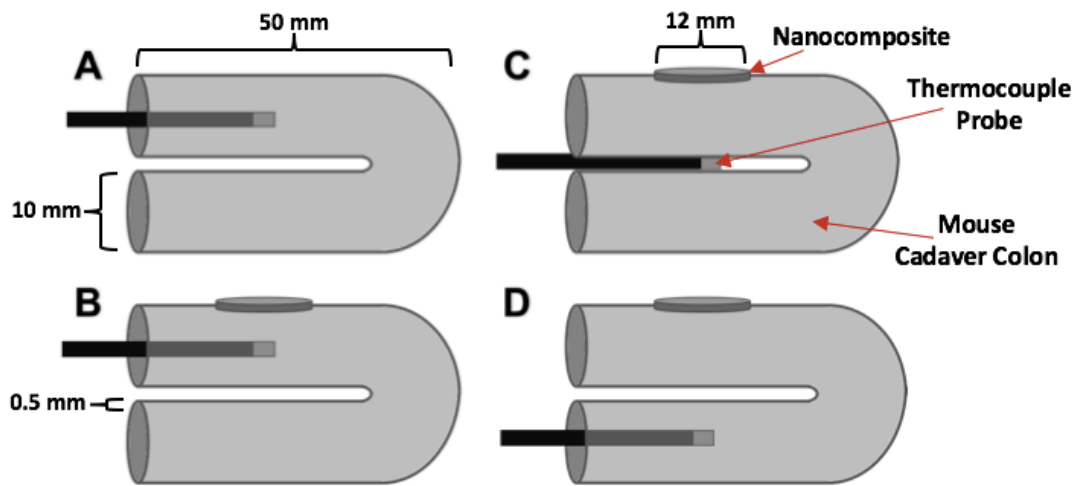
Figure 22. Depiction of nanocomposite patch and temperature probe locations. (A)Within the primary lumen, while the bare intestine is irradiated. (B) Within the primary lumen, while the nanocomposite over the intestine is irradiated. (C) Between the primary and secondary lumen while the nanocomposite over the intestine is irradiated. (D) Within the primary lumen, while the nanocomposite over the intestine is irradiated.

Mathematical Model

      heat transfer. A modified form of the Pennes Bio-heat Equation was used to model heat transfer in laser tissue soldering simulations. This equation is used to model the heat transfer within tissues, including in tissues with blood flow(Fuentes et al., 2009; Pennes, 1948). Equation 1 consists of the simplified form of this equation used in the nanocomposite model:

$$\frac{dT}{dt} = \alpha \, \nabla^2 \, T + \frac{Q_{laser}}{C_p \cdot \rho} \left(1 - 10^{-OD}\right). \qquad (1)$$

The first term of Equation 1 accounts for thermal diffusion, where α is thermal diffusivity of both the tissue and the nanocomposite patch and is defined by Equation 2:

$$\alpha = \frac{k}{C_p \cdot \rho} \qquad (2)$$

where k is the thermal conductivity of the nanocomposite patch or surrounding tissue, C_p is the heat capacity for both the nanocomposite patch and the tissue, and ρ is the density. The second term in Equation 1 accounts for the heat generation from the laser energy absorbed by the GNR-infused collagen patch. The variable Q_{laser} refers to the laser power density for the system, and OD is the optical density of the nanocomposite patch. An additional term accounting for blood flow was excluded here due to the lack of blood flow in the experimental system that was used for model validation, and while blood flow has been shown to have a heat-sinking effect, the blood vessels would be coagulated so quickly that the effect of blood flow is minimal(B. M. Kim, Jacques, Rastegar, Thomsen, & Motamedi, 1996). The equation was transformed into a time-dependent, variational problem and approximately solved on the domains of interest using the finite element method.

The tissue surrounding the patch was assumed to initially be at a fixed temperature, and the modeled tissue region extended sufficiently far beyond the nanocomposite patch such that fixed temperature (i.e., Dirichlet) boundary conditions were applied to the four exterior sidewalls of the porcine model domain and the two end walls of the mouse model domain. This assumption was validated two ways: first, the magnitude of the temperature

gradient near the wall was checked (a gradient of less than $1°C/mm$ was observed) and the size of the domain was increased to confirm that the temperature in the region of interest did not change significantly. A no-flux boundary condition was applied along the bottom tissue surface to represent the low thermal conductivity surface used for the porcine experimental measurements, and a fixed temperature boundary condition was used along the bottom tissue surface to reflect the additional intestinal tissue present in the mouse experiments. A Robin boundary condition was applied along the top of the nanocomposite surface that is exposed to air. The Robin boundary condition, which accounts for convection occurring at the air-composite interface, was applied along the upper surface using:

$$\frac{\partial T}{\partial n} = \frac{U_{air}}{k}(T - T_o) \qquad (3)$$

where U_{air} is the overall heat transfer coefficient for air, T is the local tissue/nanocomposite surface temperature (changing with time), and T_0 is the bulk air temperature.

The model parameters for the nanocomposite patch system are listed in Table 1. Many of the parameters were based on values determined previously for an *in vitro* GNR and cell system(H.-C. Huang et al., 2010c), and many parameter values are relatively close to those of water, consistent with the high water content of the nanocomposite patch and intestinal tissue.

Table 1. Heat transfer and nanocomposite patch parameters used in the mathematical model. Based on References(Diller, Valvano, & Pearce, 2000; H.-C. Huang et al., 2010c; Rylander, Feng, Bass, & Diller, 2007)

Parameter	Variable	Value
Optical Density	OD	0.1
Density	ρ	$0.001 \frac{g}{mm^3}$
Heat Capacity	C_p	$3.4 \frac{J}{g \cdot K}$
Thermal Conductivity	k	$0.58 \frac{W}{m \cdot K}$
Overall Heat Transfer Coefficient (air)	U_{air}	$0.08 \frac{W}{m^2 \cdot K}$
Laser Power Density (area)	Q	$0.0233 \frac{W}{mm^2}$
Optical Thickness	d	$0.50 \, mm$
Laser Power Density (volume)	Q_{laser}	$0.0466 \frac{W}{mm^3}$
Overall Laser Expression	$Q_{expression}$	$13.7 \frac{K}{s}$
Thermal Diffusivity	α	$0.171 \frac{mm^2}{s}$
Initial Temperature	T_0	23 °C
Universal Gas Constant	R	$0.008314 \frac{kJ}{mol \cdot K}$
Arrhenius Scaling Factor	A	$6 \times 10^{29} \, s^{-1}$
Arrhenius Activation Energy	E_a	$200 \frac{kJ}{mol}$

In the LTS experiments, the cylindrical intestine was relaxed into a relatively flat, rectangular shape that was the thickness of the pair of intestine walls, and the width was roughly half the circumference of the intestine. As a result of this configuration, the geometry used in the model of the porcine intestinal tissue was a 3-dimensional rectangular

domain with dimensions of [50 mm × 20 mm × 4 mm], divided into a tetrahedral finite element mesh with divisions of [100 x 40 x 20] for the rectangular, 3-dimensional domain. Simulations were also run on a higher resolution finite element mesh ([150 x 60 x 30] divisions) to confirm that the temperature solution changed by less than 2%. A cylindrical patch, 10 mm in diameter and approximately 1 mm in height, was added atop the tissue surface to represent the nanocomposite solder material. The temperature prediction comparison of the finer meshes to the primary mesh deviated by less than 2%. A diagram depicting the full model domain (intestinal tissue and nanocomposite patch) with the corresponding boundary conditions is displayed in Figure 23.

$$\frac{\partial T}{\partial z} = \frac{U_{air}}{k}(T - T_o)$$

$$\frac{\partial T}{\partial x} = 0$$

$$T = 23°C$$
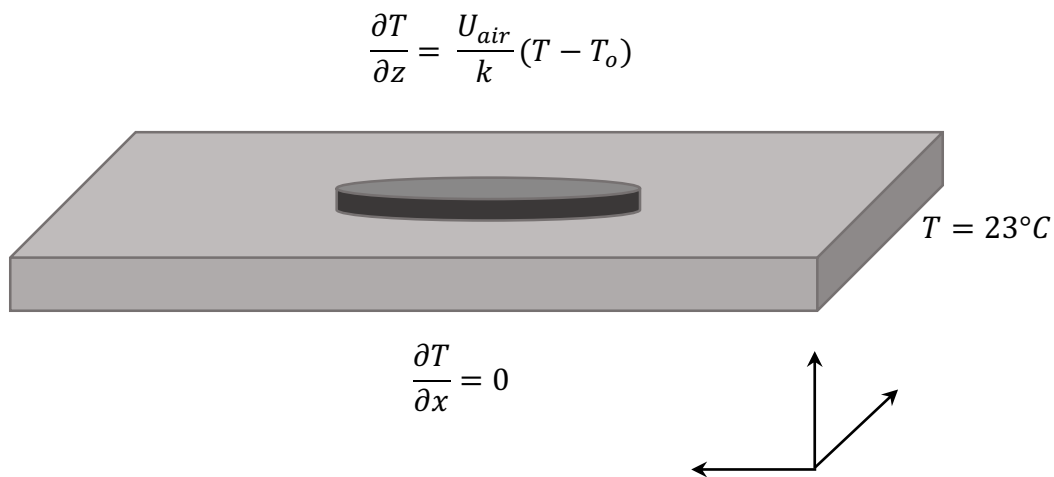
Figure 23. The mathematical model domain. The domain represents the flattened intestine (light grey) with dimensions of [50mm x 20mm x 4 mm] and a circular patch (dark grey) of 10 mm diameter protruding atop the center of the brick was used in the model with its corresponding boundary.

cell death prediction. The Arrhenius cell injury model was used to predict cell death and injury within the tissue(Henriques, 1947; Rylander et al., 2007). Applying the Arrhenius equation (Equation 4), the rate of cell injury can be calculated as:

79

$$k = Ae^{\frac{-E_a}{R \cdot T}} \qquad\qquad (4)$$

where A is a scaling factor, E_a is the activation energy for injury of the cell, R is the universal gas constant, and T is the local temperature. The variables A and E_a were estimated based on previous cell death measurements in a human cell line (PC3-PSMA), and their corresponding values are included in Table 1(H.-C. Huang et al., 2010c). These values are also consistent with the values measured for cells and tissue of similar nature(Bhowmick et al., 2004; Lepock, 2003). The fraction of cells killed, F_D, was calculated by integrating the accumulated cell injury, k, using Equation 5(H.-C. Huang et al., 2010c).

$$F_D = 1 - e^{\int_0^t k*dt} \qquad\qquad (5)$$

The values for F_D range from 0 to 1, with values closer to 1 approaching 100% cell death prediction.

mouse cadaver model. A model similar to the porcine model was created to predict spatiotemporal temperature profiles and corresponding cell death in the intestinal tissue of mice using many of the same parameters. Variations in the parameters were limited to dimensions of the tissue and laser power density. The mouse model domain had the same shape as the porcine model (i.e., a flattened intestine), but the dimensions for the mouse model were 20 mm × 10 mm × 4 mm. Although the wall thickness of the mice intestinal tissue is less than 1 mm, multiple layers of intestinal tissue were present so the overall tissue thickness was set to 4 mm in the z-direction, and the 20-mm length was chosen to ensure that the fixed temperature boundary condition was valid. The laser power density used in this experiment was $0.0167 \frac{W}{mm^2}$, resulting in an overall laser power per volume of

$9.67 \frac{W}{mm^3}$ for the nanocomposite patch. A thermocouple was placed in three different locations within the tissue sample: inside the upper segment of intestine, between the upper and lower segments, and inside the lower segment of intestine (Figure 22).

Results and Discussion

  porcine cadaver intestine model. The heat transfer model was used to predict the temperature distribution within the nanocomposite and porcine intestine. The maximum surface temperature was predicted to reach a value of 69°C (Figure 24) after 4 minutes of laser irradiation at 2.33 W/cm^2 CW, which was consistent with experimental measurements (67°C, Figure 25). Due to the elliptical nature of the laser, this elevated temperature at the patch surface extended outward from the center 10 mm by 2 mm ellipse in the x- and y-directions, respectively, in both the IR images acquired during experimentation and in model predictions as shown in Figure 24. The temperature decreased as the distance from the center of the area of laser exposure in the nanocomposite increased, with the outermost diameter of the patch attaining a temperature of approximately 45°C. Outside the 10-mm diameter of the patch, the domain has a moderately elevated temperature extending approximately 2 mm and 3 mm in the x- and y-directions, respectively.

81
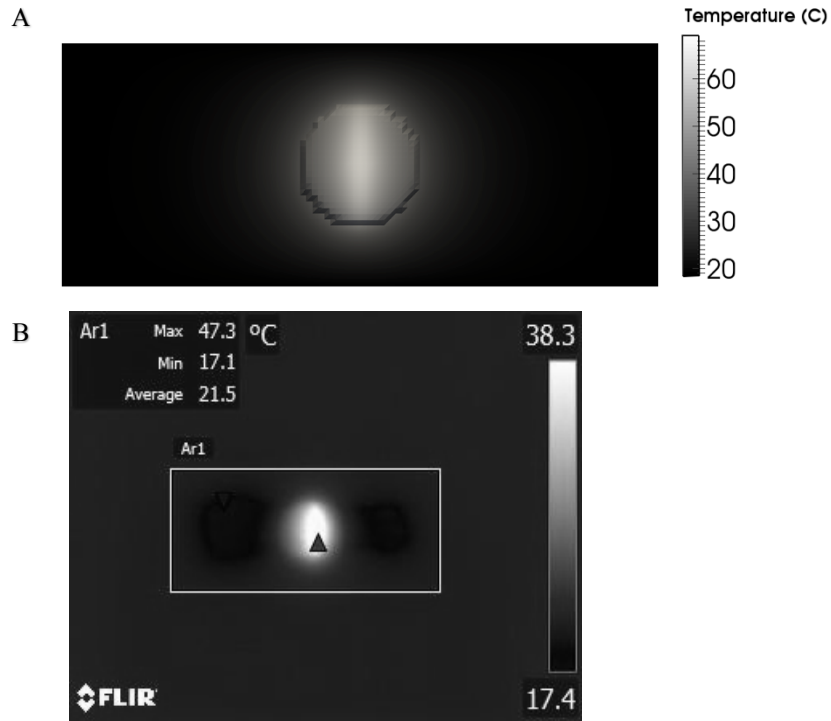
Figure 24. Surface temperature predictions and measurements. (A) Surface temperature prediction from the heat transfer model after 4 minutes of laser treatment at 2.33 W/cm^2 CW in porcine intestine, and (B) experimental measurement of the surface temperature measurement of the porcine intestine (box) after a similar time period.

The heat transfer model predictions are compared to experimental measurements in Figure 25. The temperature at two different points within the experimental system was monitored during laser irradiation of the nanocomposite at 2.33 W/cm^2 CW for 4 minutes. The first location is the surface temperature at the top of the domain (the nanocomposite surface at the laser exposure center), and the second location is inside of the intestinal lumen, directly below the nanocomposite and the 4-mm thick intestine wall. The individual data points show the experimental measurements at the two different locations, and the solid lines show the heat transfer model prediction of the temperatures at these experimental conditions. Variation within the surface temperatures of the experimental

data are seen when incorporating the thermocouple directly underneath in the lumen because the operator holding the thermocouple can create small movements in the LTS configuration. The heat transfer model predictions agree well with the trends shown in experimental data for the nanocomposite and tissue surface temperatures (Figure 25). The agreement is not as good, however, for the temperature inside the intestinal lumen for the earlier time points, which show a difference of approximately 5°C between the heat transfer model prediction and experimental measurements during the first three minutes of the four-minute LTS experiment. In the final minute, the model predictions and experimental results show significantly better agreement. This difference may be due to potential energy absorption directly by the metal thermocouple below the tissue surface. Exploring a different experimental setup for measuring luminal temperatures may improve the experimental results by removing any artifacts in heat generation.
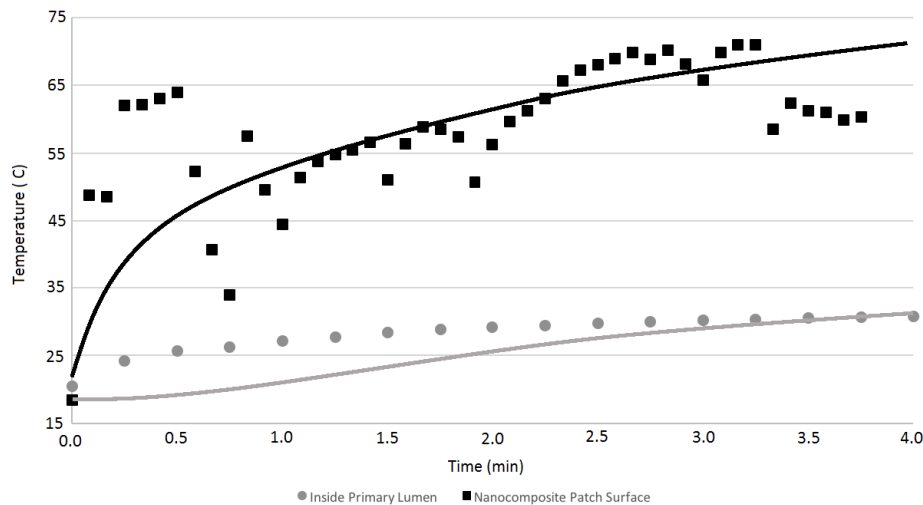
Figure 25. Experimental welding temperature compared to predicted temperature. The solid lines (upper and lower) represent the model temperature prediction at two different locations (surface temperatures and inside the primary lumen) corresponding to the same

locations as the experimental measurements. Experimental data are representative of n=3 independent experiments.

The profile view of the nanocomposite (Figure 26) displays a predicted temperature gradient extending through the entire depth of both the 1 mm patch and 4 mm tissue. The elevated temperatures (>45°C) extend approximately halfway through the depth of the tissue. These results show that even for extended heating periods (4 min) peripheral tissue surface temperature is predicted to rise very little as close as 3 mm in the x or y direction from the nanocomposite patch. Additionally, the temperatures predicted below the tissue surface do not extend beyond 3 mm in the x or y direction from below the nanocomposite. The temperature within the nanocomposite is above approximately 55°C uniformly throughout the material, although the surface of the nanocomposite is not uniformly exposed to the laser suggesting that the GNRs in the nanocomposite rapidly heat up and transfer heat throughout the nanocomposite. These elevated temperatures extend through the nanocomposite and into the intestinal tissue directly below.
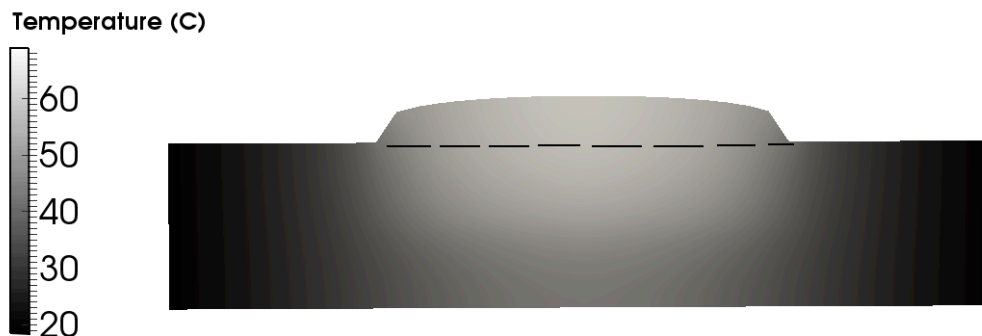
Figure 26. Profile view of the temperature gradient through the x-z plane. The dashed line (−) represents the patch-tissue interface, with the area above encompassing the patch and the area below encompassing the tissue.

The results of the cell death model predictions in porcine intestine are shown in Figure 27. As temperature and time at the elevated temperature increased, cell death also increased. With temperatures reaching above 50°C for some of the tissue depth, close to 100% of the cells in the portion of the domain where temperatures exceeded 50°C were predicted to have been killed by hyperthermia (Figure 27). It is interesting to note the sharper transitions (i.e., sharper gradients) in the cell death model predictions relative to temperature predictions. Increased cell death at higher temperatures is due to the exponential relationship between hyperthermal cell death and temperature that is described by the Arrhenius cell death model. This result suggests that any cell death that results from the LTS process is likely to be mostly limited to the tissue immediately adjacent to and below the soldering nanocomposite and limited beyond that region. It should be noted, however, that additional, longer-term cell death may occur after the initial thermal insult(Pearce & Thomsen, 1995). In a surgical setting, this region directly below the nanocomposite includes the negative space of the wound bed and the tissue edges likely to become necrotic as the wound heals. The incision space and necrotic tissue negate much of the concern regarding extensive cell death directly underneath the nanocomposite, where the majority of cell death occurs as shown in Figure 27.
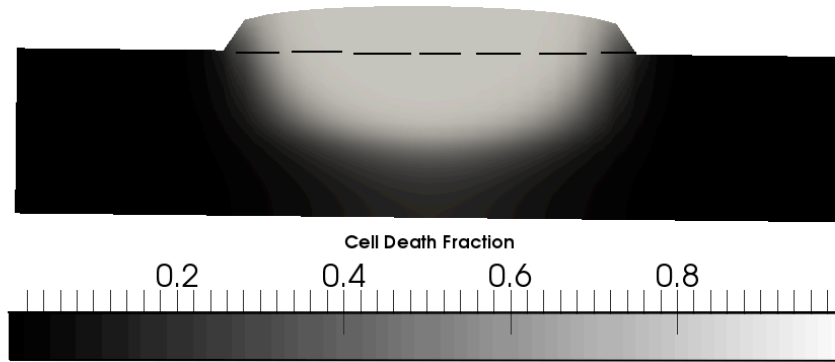
Figure 27. Cell death fraction through the porcine tissue. Cell death after 4 minutes of laser treatment at 2.33 W/cm^2 CW. The dashed line (–) represents the patch-tissue interface, with the area above encompassing the cell-free patch and the area below encompassing the tissue.

Increasing the duration of the laser treatment resulted in higher temperatures and longer time for injury accumulation in both the immediate area undergoing laser irradiation as well as the surrounding area, and these increased temperatures and accumulated injuries are predicted to generate more extensive cell death. For this reason, the power density and duration of laser treatment must be limited to mitigate any extensive and peripheral elevated temperatures and extensive cell death(Dewhirst, Viglianti, Lora-Michiels, Hanson, & Hoopes, 2003). Ultimately, an optimum set of conditions should exist that balance the increase in temperature with the duration of the heating.

Because exact mechanisms of LTS and heat-induced tissue fusion are not entirely known(Constantinescu et al., 2007c; Sriramoju & Alfano, 2011b), the spatiotemporal model cannot be extended to predict solder integrity at various LTS power densities and laser durations. It has been hypothesized in the literature, however, that a critical soldering temperature exists below which protein interdigitation(Paolo Matteini, Rossi, Menabuoni, & Pini, 2007b) and bonding(B. S. Bleier et al., 2007b) will not occur. General consensus

in the field is that the critical temperature is in the range of 60-65°C(Paolo Matteini, Sbrana, et al., 2009), although this varies by tissue type. Below this critical temperature, solder strength will be insufficient to cause tissue fusion, while above this temperature, thermal damage increases significantly and tensile strength is decreased(Hoffman et al., 2003b). Correlating the temperature to mechanical strength (while exact mechanisms are not known) can aid in determining the critical soldering temperature as well as in adjusting parameters that can be employed to lower the temperature while maintaining solder integrity to further limit thermal damage and cell death. This is demonstrated in Figure 28, which shows that irradiation of the nanocomposite using a laser at 1.83 W/cm^2 results in a steady-state temperature of approximately 57°C after roughly 4 minutes (white boxes), and at 2.33 W/cm^2 results in approximately 75°C in 4 minutes (black boxes). Additionally, a negligible rise in temperature is seen for collagen films in absence of GNRs following irradiation with NIR laser as shown in Figure 28 (grey circles). While only 5% GNR-collagen nanocomposites were used in this work, future work could include optimizing the nanocomposites to minimize the amount of GNRs used while still maintaining reasonably low and inexpensive laser power densities to produce sufficient heat for soldering. In Figure 28, unlike Figure 25, a thermocouple has not been placed below the tissue surface, and it can be seen that the temperature variations are much less extreme.
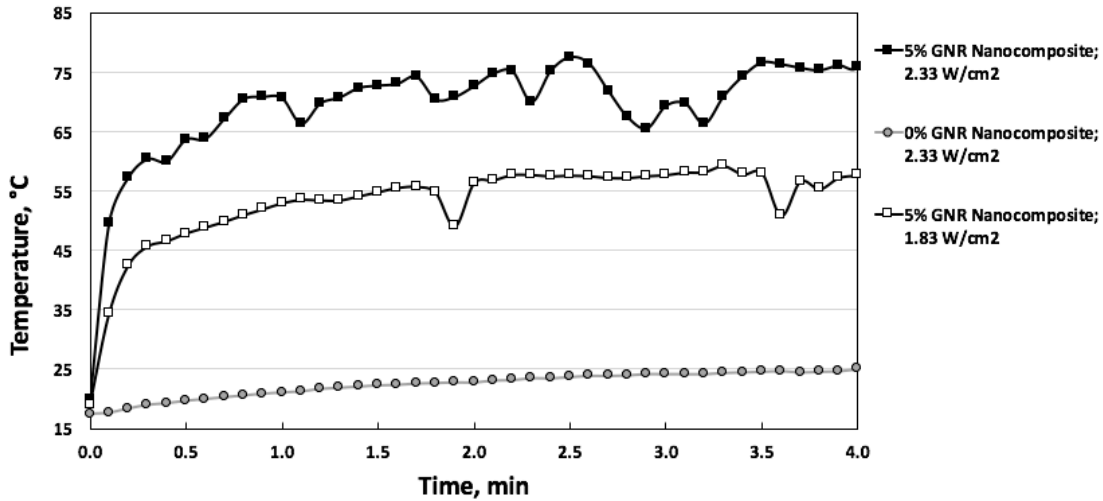
Figure 28. Nanocomposite surface temperature during laser soldering. Surface temperature of porcine intestine as measured by IR images. Grey circles indicate collagen patches with 0% GNRS irradiated at 2.33 W/cm^2, white boxes represent 5% GNR-collagen nanocomposites irradiated at 1.83 W/cm^2, and black boxes show 5% GNR-collagen nanocomposites irradiated at 2.33 W/cm^2. Curves are representative of the temperatures reached in n=3 independent experiments and the lines connecting the data are only for visualization of data trends.

From Figure 29, the laser soldering condition that results in a temperature of 57°C results in a 21.9% return in tissue tensile strength that is not statistically significant compared to the tensile strength of ruptured intestine. By contrast, the soldering condition that results in a temperature of 75°C results in a 58.5% return in tensile strength of that of the native tissue compared to the ruptured tissue. The effect of these two temperatures is even more pronounced in the comparison of the fluid pressures at which intestine rupture first occurs. When LTS is performed at 57°C for 4 minutes, there is no significant increase return in the native tissue pressure from the unsoldered ruptured intestine and thus has remained largely unsoldered. By comparison, soldering at the 75°C condition for 4 minutes

88

results in a 46.9% return in rupture pressure of the native intestine, which is significantly different than that of the untreated ruptured tissue and a strong indication of successful soldering. Because the improvement in rupture pressure is nearly 10-fold in the 75°C treatment compared to the 57°C treatment, the 57°C did not reach or maintain the critical soldering temperature for sufficient treatment time, while the 75°C treatment did elicit tissue fusion. These results strongly advocate for a correlation between soldering temperature and closure strength. The temperature predictions from Figure 26 suggest that there is sufficient heat to induce soldering in the full 4-mm thickness of the intestine with a critical soldering temperature of 60°C. Also, due to the highly localized predicted elevated temperatures, sealing of peripheral tissue or inadvertently sealing the intestinal lumen closed appears highly unlikely. Further work using this spatiotemporal model to predict solder strengths based on LTS temperatures will incorporate the fundamental investigation of the heat-induced chemical mechanisms involved in tissue fusion.
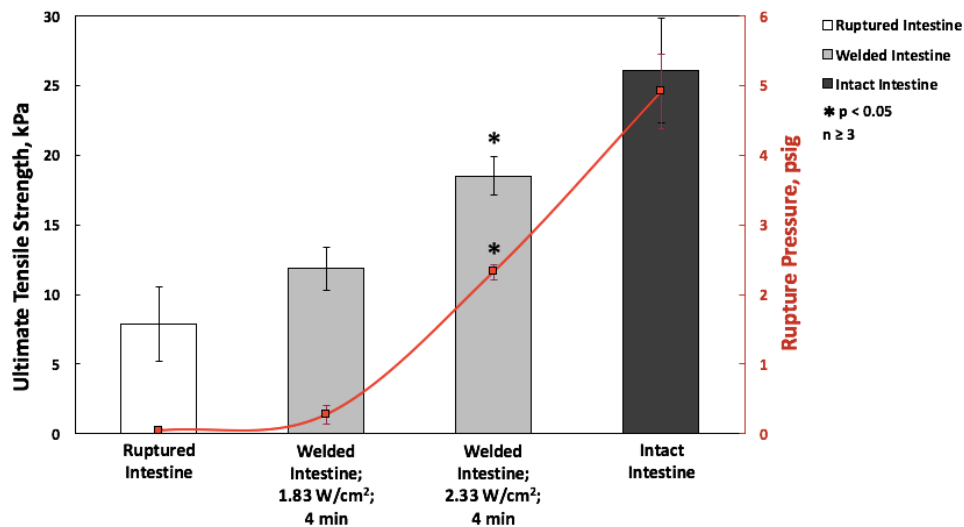
Figure 29. Tensile strength and rupture pressure of porcine intestine. Intestines (grey) were laser soldered at 1.83 or 2.33 W/cm^2 for 4 minutes, compared to ruptured (white) and intact intestine (black). Red line indicates the rupture pressure at these conditions.

mouse cadaver colon model. The mathematical model of temperature distribution in the LTS patch and mouse intestine predicted a maximum temperature of approximately 48°C over the 4 minutes of laser duration (Figure 30). As with the porcine predictions, the maximum temperature was attained near the center of the elliptical region directly exposed to the laser. The region of elevated temperatures extended outward approximately 3 mm past the outer edge of the patch in both the positive and negative x-directions, but the magnitude of the temperature elevation was very small for most of the tissue surrounding the patch. The temperature outside of the patch region reached a high of approximately 32°C (Figure 30).
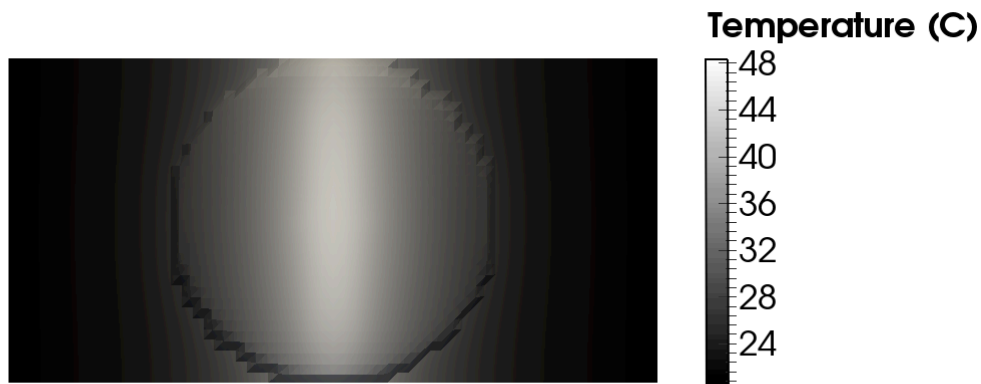
Figure 30. Surface temperature prediction for heat transfer model. Surface heat transfer for mouse tissue after 4 minutes of laser duration.

Temperatures were recorded at three points within the tissue below the patch: inside the primary lumen, between the primary and secondary lumen, and inside the secondary lumen (Figure 22). The thickness of the intestinal wall was assumed to be approximately 0.5 mm thick, meaning the temperatures were recorded at depths of 0.5 mm, 1.0 mm, and 1.5 mm below the surface of the intestine (i.e., below the patch). The experimentally measured temperatures at each location are plotted versus time for the duration of the laser

90

treatment, and compared with the mathematical model predictions of temperature at the same locations in Figure 31.

The model predictions (shown as lines in Figure 31) show many of the same characteristics observed in the experimental data (shown as distinct points). Specifically, the rate at which the temperature increases within the tissue is similar between the model and experiment, and the temperature differences between the tissue layers are also consistent. It should be noted that for the uppermost location (thermocouple in Figure 22), the laser was turned off after 2 minutes so comparisons with the model predictions after that time are not possible. There are also some differences between the model predictions and experimental measurements, especially early in the experiment between 30 seconds and one minute. These differences could stem from the location of the probes in the model relative to the actual location from the experiment because the exact thickness of the intestine wall is not known. Similarly, they could be caused by the thermocouple directly absorbing some laser energy. These results suggest that the heat generated in LTS is not sufficient to seal adjacent tissue inadvertently.
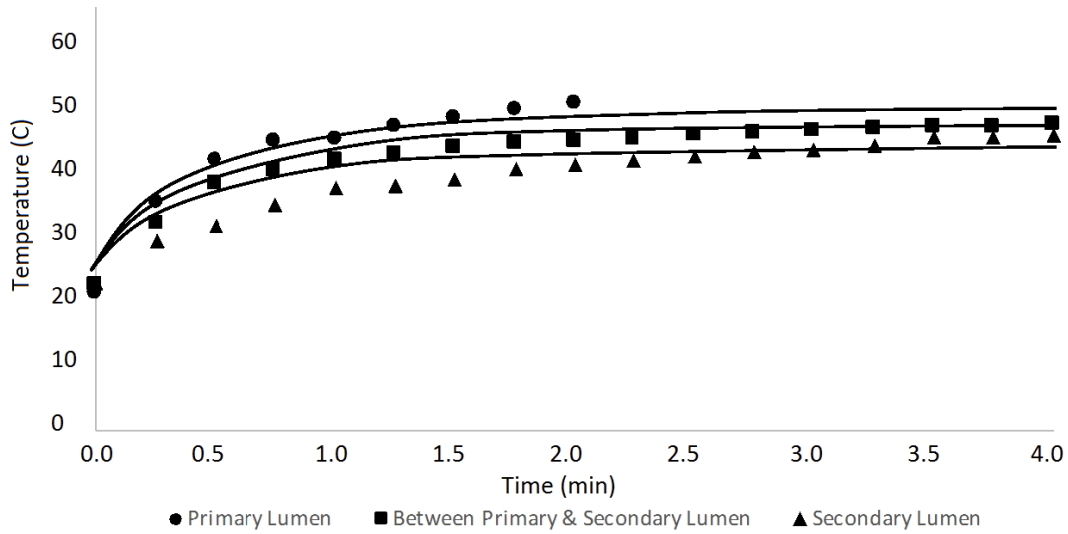
Figure 31. Temperature over time at various thermocouple locations. Temperature for locations shown in Figure 22 in the mouse intestinal tissue (discrete points), and the solid lines represent the model prediction for each respective location. The lowest line corresponds to within the secondary lumen, the middle line signifies the temperature between the primary and secondary lumen, and the top-most line corresponds to within the primary lumen.

Conclusions

A spatiotemporal model has been developed for predicting temperature changes and potential thermal damage during the LTS process with the long-term goal of enabling optimized outcomes and reducing total experimental work by correlating laser power density and treatment duration to solder strength. The model predicts temperature within a photothermal nanocomposite material and surrounding tissue as well as cell death in tissue during the LTS process. For the model results replicating the porcine experimental measurements, the surface of the composite patch reaches temperatures in excess of 60°C while the adjacent tissue directly below the nanocomposite reaches temperatures in excess of 50°C. However, the elevated tissue temperatures are only reached for the few minutes

92

the laser remains on, and temperatures return to ambient within minutes of the laser being turned off. All temperature predictions from the mathematical model are consistent with experimental measurements. The model predicts that a high fraction of cells is killed by hyperthermia in the tissue immediately adjacent to the nanocomposite, but this is a relatively small region that in a surgical setting would contain tissue subject to cell death already because of the incision, and the vast majority of cells are expected to survive just a short distance (~2 mm) from the patch. The mathematical model was also assessed through comparisons to temperature measurements from LTS experiments on mouse intestines. In this case, temperature measurements at multiple tissue depths were available, and the mathematical model predictions were quantitatively consistent with the experimental measurements.

Future work will focus on predicting the strength of the solder and identifying conditions that minimize cell death and necrosis in the region adjacent to the patch. Future work also will include mechanistic work with *in vivo* data to better understand the molecular processes involved in tissue fusion and incorporate these into a predictive model. In addition to laser power density and duration of irradiation, a number of treatment parameters can be varied to optimize LTS using photothermal nanocomposites. These include concentration of the chromophore GNRs in the nanocomposite, laser power density, duration of exposure, humidity, blood flow, and tissue homogeneity. Future work on this mathematical model includes incorporating more variables into a predictive model that will assist in the identification of optimal conditions for tissue fusion and repair.

RAPID SOFT TISSUE APPROXIMATION AND REPAIR USING LASER-ACTIVATED NANOSEALANTS

Introduction

In surgical tissue repair, sutures or staples physically approximate tissue discontinuities but can simultaneously cause tissue trauma and complications, including infection(Park, 2010b). Alternatively, glues, sealants, and adhesives rely on chemical interaction with the tissue, often at slow polymerization rates. Many adhesives, including cyanoacrylate and fibrin glues, impart insufficient closure, poor adhesion(Jeon et al., 2015), toxicity(Dong et al., 2015), or inhibit cell migration(Yeung, Faraj, McIntosh, Dhillon, & Dua, 2016). Laser-activated tissue repair is an alternative approach for tissue repair without sutures, staples, or polymerization. In this approach, laser light absorbed by a chromophore is converted to heat, which restructures tissue proteins(Constantinescu et al., 2007c; Sriramoju & Alfano, 2011c) to fuse with the applied sealant material by means of protein interdigitation(Paolo Matteini et al., 2007b). Laser tissue sealing has been shown to reduce operation and healing times, infection, and scarring compared to conventional repair(Alster & Zaulyanov-Scanlon, 2007b; Atalay et al., 2009b). However, inconsistent seal strength(Dara Rosmailina Pabittei, 2013), potential for thermal damage(Mushaben et al., 2018) and inadequate laser penetration(F. Rossi et al., 2005) limit this method as a viable replacement to physical approximation as the platform technology in the operating room. The deficiencies of existing laser-activated tissue repair necessitate the development of novel laser-responsive biomaterials for tissue repair.

Near infrared (NIR) light (700-1,300 nm) is an attractive modality for medical treatment because of the general inertness of healthy tissue to light stimuli(Weissleder,

2001) and because of the relatively deeper penetration of these wavelengths into tissue compared to visible light. Exogenous chromophores that absorb and convert NIR light to heat can localize elevated temperatures at specific locations, thereby minimizing broad thermal damage in tissue(Esposito et al., 2013a). Gold nanoparticles, widely studied in therapeutics and diagnostics(Urie & Rege, 2015), are promising photothermal convertors for NIR light activated tissue repair(Gobin, O'neal, et al., 2005). Specifically, gold nanorods (GNRs) efficiently convert NIR light to heat(M. C. Daniel & Astruc, 2004), are easily functionalized(Hoffman et al., 2003b), and are highly photostable compared to NIR-absorbing dyes(Brust, Fink, Bethell, Schiffrin, & Kiely, 1995). Embedding GNRs within a polypeptide (e.g. silk) matrix can overcome chromophore leaching, slow heat transfer, and inconsistent chromophore application, which are typically associated with glues that contain organic dyes(Urie, Flake, & Rege, 2017). Silk can be fabricated into various morphologies(Perrone et al., 2014; Rockwood et al., 2011; Tao, Kaplan, & Omenetto, 2012) for diverse applications in tissue engineering(X. Zhang, Reagan, & Kaplan, 2009). Silk fibroin elicits low immunogenicity and inflammatory response(Yucel, Lovett, & Keplan, 2014), with robust mechanical properties(Koski, Akhenblit, McKiernan, & Yarger, 2013; Tucker et al., 2014). Silk scaffolds possess high thermal stabilities(X. Zhang et al., 2009) and degrade slowly *in vivo*(Algarrahi et al., 2015; Thurber, Omenetto, & Kaplan, 2015; W. Zhang et al., 2015), desirable for applications requiring tissue ingrowth(Diab et al., 2012; Horan et al., 2009) or sustained release(Yucel, Lovett, Giangregorio, Coonahan, & Kaplan, 2014; Yucel, Lovett, & Keplan, 2014).

In this work, silk-GNR nanosealants were developed as flexible films and viscous pastes for laser-activated soft tissue approximation and repair. In cadaveric porcine

intestine, these laser-activated nanosealants (LANS) rapidly seal incisions and prevent bacterial leakage, unlike clinical standard suturing. LANS also repair skin incisions in live mice faster, with greater mechanical recovery, and with less fibrosis and inflammation compared to conventional surgical sutures. These results indicate that laser-activated nanosealants can replace sutures, glues, or staples in soft tissue surgery and potentially prevent complications including surgical site infection, sepsis, and dehiscence(Park, 2010b; Wick et al., 2011), ultimately leading to improved patient outcomes.

Materials and Methods

materials. Cetyltrimethylammonium bromide (CTAB) was purchased from BP Chemicals (Santa Ana, CA). $NaBH_4$, $HAuCl_4 \cdot 3(H_2O)$, $AgNO_3$, and L-ascorbic acid were purchased from Sigma-Aldrich (St. Louis, MO). Nanopure water was obtained from a Millipore filtration system (Darmstadt, Germany) with 18.2 MΩ-cm resistivity. Cadaver porcine small intestine was purchased from Animal Technologies, Inc. (Tyler, TX). To maintain reagent integrity: $HAuCl_4 \cdot 3H_2O$ was kept at 0°C; $NaBH_4$ and $AgNO_3$ solids were stored under vacuum; $HAuCl_4$ and $AgNO_3$ solutions were kept at 4°C; and CTAB solutions were maintained at 27°C. Other reagents were maintained at room temperature.

cocoon degumming and aqueous silk preparation. *Bombyx mori* silk cocoons from lab-cultivated larvae were degummed(C. Guo, N. Hall, B. Addison, & L. Yarger, 2015; Rockwood et al., 2011) to extract aqueous silk with a broad spectrum of molecular weight averaging 100 kDa. In brief, cocoons were cut up and washed in deionized water. The cocoons were boiled in 0.5 wt% Na_2CO_3 and 1 wt% Marseille soap for 30 minutes, washed in distilled water three times, and vacuum-dried at room temperature. 2 grams of degummed silk fibers were dissolved in 10 mL of 9.4M lithium bromide (LiBr) at 60°C

for four hours, centrifuged to separate insoluble contents, and dialyzed for 72 hours at 4°C against a 3.5 kDa membrane to remove LiBr and impurities. Dialysate water was changed daily. The silk was centrifuged at 14,000 rpm for 30 minutes to remove remaining impurities. The solution was then stored at 4°C until use.

gold nanorod synthesis. Gold nanorods (GNRs) were prepared via a seedless growth method(Ali, Snyder, & El-Sayed, 2012). Briefly, 5 mL of 1 mM $HAuCl_4$ were added to 5 mL of 0.2 M CTAB and 8 µL of 12.1 M HCl (37% w/w). $AgNO_3$ (200 µL) was then added. Freshly-dissolved ascorbic acid (70 µL, 78.8 mM) was added, and the solution was carefully mixed until turning colorless. Cold $NaBH_4$ (15 µL, 10 mM) was then added immediately. The solution was incubated at 25°C for 6 hours, and the GNRs were centrifuged at 14,000 rpm for 30 minutes. The supernatant was discarded; the pellet was dispersed in water and centrifuged again for 30 minutes at 14,000 rpm. The supernatant was discarded, and the pellet was dispersed in water to the desired concentration.

formation of silk-gnr nanosealants. To prepare silk-GNR nanosealant films, the concentrated GNR dispersion (1 wt%) was added to 1 mL of the 6 wt% purified silk solution and mixed until homogenous at 4°C. Approximately 100 µL of the nanosealant mixture was poured into 1 cm diameter petri dishes and dried overnight at room temperature. In some cases, nanosealants were immersed in a small volume of methanol for 24 hours and left to air dry for 24 hours. This methanol treatment rendered the nanosealants insoluble in water(Tao et al., 2012). Four silk films were used in this study: pristine silk films (PS), silk films embedded with GNRs (S-GNR), methanol-treated silk films (mS), and methanol-treated silk films embedded with GNRs (mS-GNR), shown in Figure 32A.
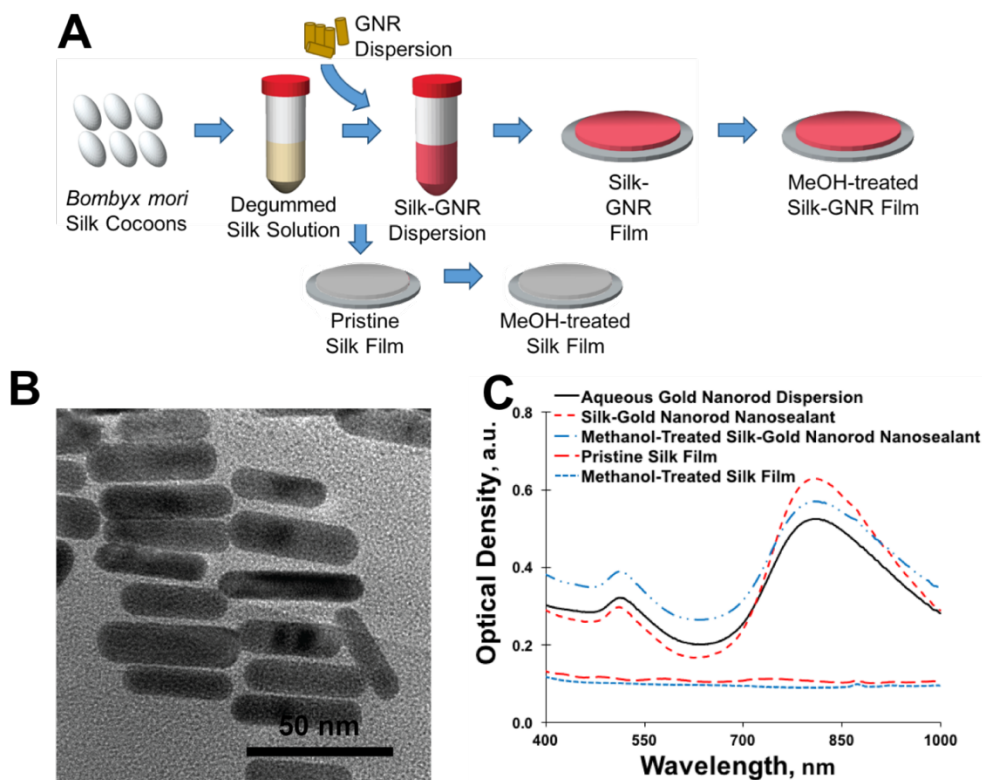
Figure 32. Generation and characterization of silk-gold nanorod nanosealants. (A) Generation of silk-gold nanorod nanosealants. Silkworm cocoons are degummed and purified. Pristine silk is aliquoted and dried, creating thin films which can be treated with methanol. Similarly, a GNR dispersion can be homogenized into the silk solution, and thin films can be slow dried and treated with methanol. (B) Transmission Electron Microscopy (TEM) image of GNRs in aqueous dispersion. (C) Absorbance spectra of GNR aqueous dispersions, pristine silk films, methanol-treated silk films, silk-gold nanorod nanosealants, and methanol-treated silk-gold nanorod nanosealants.

nanoparticle leaching, film solubility, and mechanical strength. Films were placed in scintillation vials with 10 mL of phosphate-buffered saline (PBS). For up to 6

months, 100 µL samples of the supernatant were tested with a Synergy 2 Multi-Mode Reader (BioTek Instruments; Winooski, VT) for absorbance at 800 nm as an indication of GNR content leached from the solid-phase nanosealants into the supernatant. To measure mechanical strength, the silk films were patched on a paper frame and mounted on an ElectroPuls E3000 (Instron, Norwood, MA). The samples were tested at a crosshead speed of 2 mm/min. Ultimate tensile strength was defined as the maximum stress, and the elongation to failure was the final point before a >10% decrease in load.

transition electron microscopy. GNRs were concentrated ten-fold by centrifugation. A copper-coated carbon grid was dipped in GNRs, dried three times, and desiccated. TEM images were taken on a Philips CM200-FEG high resolution TEM at 200 kV and were analyzed using ImageJ. The dimensions of 300 nanostructures were measured for reported values.

ftir and solid-state nmr microscopy. FTIR spectra were collected on a Bruker IFS66V/S FTIR/FT-Raman spectrometer with a diamond ATR (Pike Tech.). Spectra were collected at a resolution of 4 cm^{-1} with a wide-band MCT detector, KBr beam splitter, and 16 scans. Helical and random coil domains had similar peaks. To avoid ambiguity, amorphous structure was used to note peak assignments. Solid-state NMR spectra were collected on a Varian VNMRS 400 MHz spectrometer equipped with 1.6 mm triple-resonance MAS probe operating in triple resonance mode (^{1}H/^{13}C/^{15}N). ^{1}H-^{13}C cross-polarization magic-angle-spinning (CP-MAS) NMR experiments were done at a spinning speed of 20 kHz. The CP condition for ^{1}H-^{13}C CP-MAS NMR consisted of a 1.85 µs ^{1}H π/2 pulse, followed by a 1.0ms ramped (10 %) ^{1}H spin-lock pulse with a radio frequency (rf) field strength of 97 kHz at the ramp maximum. Experiments were performed with a 25

kHz sweep width, 3s recycle delay, and two-pulse phase-modulated (TPPM) ^{1}H decoupling level of 135 kHz. 24576 scans were applied for all samples.

photothermal response of laser-activated silk-gnr nanosealants. Nanosealant response to NIR light was investigated to determine photothermal conversion and optimal treatment conditions. A Millenia titanium sapphire laser pumped by a solid-state laser (Spectra-Physics; Irvine, CA) with a 1.5 mm diameter spot size at 800 nm wavelength was configured as continuous wave (CW) or pulsed wave (PW) with 130 femtosecond pulses at 12.5 nanosecond intervals. The laser power output varied from 0.8 to 6.4 W/cm^2, measured by a power meter. Silk films were placed on glass slides and irradiated at the nanosealant center for 120 seconds, followed by no laser exposure for 60 seconds to allow for cooling. An A325sc infrared camera (FLIR; Nashua, NH) captured top-down images of the nanosealant surface. Infrared (IR) images recorded at 1-second intervals measured surface temperatures across the nanosealant. Also, to create a moist environment mimicking surgery, a drop of saline was placed on the nanosealant. S-GNR nanosealants were not tested wet due to their rapid dissolution. The IR images were analyzed to determine the maximum surface temperature at the center of the laser exposure area. Films are sufficiently thin to assume that the surface temperature is very similar to the superficial tissue temperature directly below.

cadaveric porcine intestine incision model. Porcine intestines were cut to sections 8 cm in length and kept moist with saline. 8 mm-long incisions were made through one intestinal wall. Incision edges were approximated, and a silk-GNR nanosealant was centered over the incision and irradiated with 800-nm laser, ranging from 0.8 to 6.4 W/cm^2 for 2 to 6 minutes. The laser was oriented at one end of the 10-mm incision, and, at a speed

of approximately 0.5 mm/second, was moved back and forth along the incision line during the treatment. Alternatively, intestinal incisions were closed by suturing, using 4-0 PDS* *Plus* suture (Ethicon; Somerville, NJ), by closing the incision with 4 interrupted sutures or continuous suturing with 4 or 8 passes through the intestine. In another group, incised intestine was sutured with 4 passes of continuous suture, and a nanosealant was placed over the sutured incision and sealed to reinforce the suture line. Finally, collagen-GNR compressed hydrogels, generated using previously described methods(Urie et al., 2015c), were also used to seal incised intestine for comparison.

After laser sealing, the intestine was infused with saline until bursting to assess closure patency. A DPI 795 digital manometer (Druck), connected in series to a syringe pump, recorded the burst pressure, defined as the maximum pressure reached which is typically accompanied by rupture of the tissue and sharp loss in pressure. The syringe pump purged the line for roughly 1 minute, at which point the pressure was constant and zeroed using the manometer prior to being inserted into the intestine. The intestine section was clamped at both ends and filled with saline dyed with green food coloring at a flow rate of 0.5 mL/min or 1.0 mL/min.

Intestine was cut into 15-cm long segments with laser repair performed as described. Intact, incised, and incised and sealed intestine sections were suspended in 250 mL flasks, with the intestine ends held at the top of the flask and the center of the intestine immersed in 200 mL of fresh LB broth. The intestine sections were filled with 10 mL of fresh LB broth or broth containing DH5-α *E. coli* at an OD of 0.5 absorbance units (au). The flasks were incubated at 37°C and 150 rpm, measuring the turbidity of the LB Broth for 24 hours as an indirect measure of bacterial growth. LB broth was first inoculated with

ampicillin, and the porcine intestines were thawed and immediately rinsed in 5% bleach three times and once in nanopure water to inhibit viable bacteria originated in the intestine.

murine dorsal skin incision model. BALB/c mice and C57BL/6 mice (8-12 weeks) (Charles River Laboratories, Wilmington, MA, USA) were used with approximately equal numbers of male and female mice in a dorsal skin incision model in strict accordance with the Guide for the Care and Use of Laboratory Animals of the National Institutes of Health. Animal procedures were approved by the Arizona State University Institutional Animal Care and Use Committee (protocol 15-1428R) and conducted according to relevant national and international guidelines. Prior to surgery, each animal was anesthetized with 120mg/kg ketamine and 6mg/kg xylazine by intraperitoneal injection. The back was shaved and prepped using chlorhexidine gluconate and alcohol. Two 1-cm, full-thickness skin incisions side-by-side on the back of each animal were spaced 1 cm apart. A small volume of PBS was injected into the wound, and the apposing wound edges were approximated with forceps. Incisions were closed by S-GNR nanosealant sealing or using simple interrupted silk or nylon 5-0 suture, 4 knots (PROLENE, Ethicon). A 1.2 x 0.5 cm S-GNR nanosealant was applied over the incision, which quickly dissolved into a viscous paste due to the underlying moisture. The laser was scanned across the nanosealant-covered incision at a rate of 0.5 mm/second for 2 minutes at 4.8 W/cm^2 and an angle between 60 and 80° from the skin, corresponding to nanosealant temperatures not exceeding 80°C and underlying skin temperatures estimated at 60°C. For comparison, the left incision on each mouse was commercially-sutured, and the right incision was laser sealed. The mice were recovered on a heating pad until fully mobile. The mice were housed individually to prevent suture or nanosealant removal.

Skin was assessed 2 or 4 days after surgery. Mice were euthanized by CO_2 inhalation and cervical dislocation. Following euthanasia, rectangular sections of the wound area (2 x 1 cm, measured by calipers after underlying fascia removal) were excised. Sutures were removed to measure the strength of the healed tissue alone. Skin samples were stretched under tension until failure at a rate of 2 mm/sec using a TA.XT*Plus* (Texture Technologies Corp., Hamilton, MA). Tensile strength was defined as the peak stress. Resilience was calculated as the area under the stress-strain curve.

Samples for histological analyses were fixed in 10% neutral buffered formalin, processed and embedded in paraffin, cut into 4 mm-thick sections, and subsequently stained with hematoxylin and eosin (H&E) or Masson's trichrome. A board-certified veterinary pathologist, initially blinded to sample source, read and analyzed the slides for evidence of healing, inflammation, and collagen incorporation; the pathologist subsequently participated in discussions on interpreting the results from the different samples.

statistical analyses. Repeated measures one-way ANOVA were used to assess statistical significance.

Results and Discussion

nanosealant generation and characterization. Pristine silk (S), methanol-treated silk (mS), pristine silk-GNR (S-GNR), and methanol-treated silk-GNR (mS-GNR) nanosealants were formed as 10-mm diameter films ~200 µm thick by slow drying (Figure 32A). Aqueous dispersions of GNRs, 41.2±7.1 nm length and 11.1±1.6 nm width (Figure 32B), had a characteristic plasmonic resonance peak at 800 nm (Figure 32C), consistent with the aspect ratio(Mackey, Ali, Austin, Near, & El-Sayed, 2014; Near, Hayden, & El-

Sayed, 2013). S-GNR and mS-GNR nanosealants maintained similar absorbance behavior. Over a six-month period at room temperature, GNRs incorporated into silk films showed no significant changes in absorbance spectra, indicating a long and stable shelf life, unlike commonly used organic NIR dyes such as indocyanine green(Brust, Fink, Bethell, et al., 1995). Thermogravimetric analysis showed similar behavior for silk and GNR-containing silk films, indicating that presence of GNRs did not influence this behavior (Figure S4.1, Supporting Information).

Silk fibroin consists primarily of a repeating alanine-enriched motif (GAGAGX)(Tao et al., 2012). The distribution of helix, β-sheet, and random coil conformations was characterized by FTIR spectroscopy (Figure 33A, resonance bands summarized in Table S1) and from alanine Cβ group signals in ^{1}H$\rightarrow$^{13}C cross polarization magic angle spinning (CP-MAS) solid-state nuclear magnetic resonance (NMR) spectroscopy (Figure 33B)(Asakura, Sato, & Aoki, 2015). Degummed silk showed β-sheet domains(X. Hu, Kaplan, & Cebe, 2006; Paquet-Mercier, Lefèvre, Auger, & Pézolet, 2012) via amide I bands at 1698 and 1622 cm^{-1} (Figure 33A), and spectrum deconvolution indicated 61.7% β-sheet conformation (Figure 33C, Figure S4.2). GNR doping had minimal effect on silk structure when comparing silk films and S-GNR nanosealants. Methanol treatment increased β-sheet conformation by ~16% for the mS films and ~24% for the mS-GNR nanosealants.

These protein conformations determine the nanosealant solubility and mechanical properties for tissue approximation applications. S-GNR nanosealants dissolved readily in saline (Figure 33D-G) due to the random coil/α-helical structure. Conversely, mS-GNR nanosealants were insoluble (Figure 33H) because methanol treatment annealed α-helices

into crystalline β-sheets(Tao et al., 2012). S-GNR nanosealants showed greater tensile strength and elongation break than the more brittle mS-GNR nanosealants (Figure S4.3, Table S4.1) due to β-sheet conformations and low water content from methanol treatment(Lu et al., 2010). By modulating solubility, in particular, these nanosealants have application in internal or superficial tissue repair. The aqueous insolubility of mS-GNR nanosealants made them attractive for laser-activated repair of intestinal tissue because surgeries occur in environments where tissue is flushed and kept hydrated. Alternatively, by adding a small amount of moisture to S-GNR nanosealants, the dry films dissolve into a semisolid viscous paste. These S-GNR nanosealants were used in skin repair.

Samples	Deconvoluted FTIR	
	β-sheet	Amorphous
Degummed silkworm silk	61.7%	38.2%
Lyophilized silk	4.4%	95.6%
Silk Film (PS)	19.5%	80.5%
Methanol treated Silk Film (mS)	35.1%	64.9%
Silk-Gold nanorod Film (S-GNR)	23.3%	76.7%
Methanol treated Silk-Gold nanorod Film (mS-GNR)	47.6%	52.4%
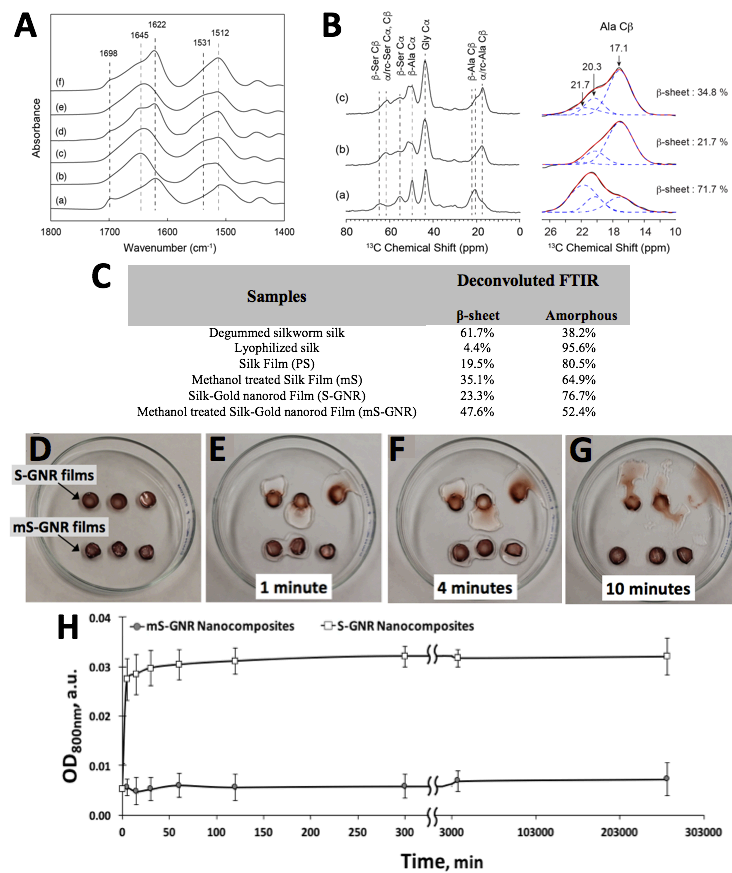
Figure 33. FTIR spectra and solubility of silk-gold nanorod films. (A) FTIR spectra of (a) degummed silkworm silk, (b) lyophilized silk, (c) slow-dried silk film and (d) further

treated with methanol, and (e) slow-dried silk-GNR and (f) further treated with methanol. After methanol annealing, the films increased in β-sheet content with the bands at 1698 cm^{-1}, 1622 cm^{-1} and 1512 cm^{-1} enhanced. (B) ^{1}H$\rightarrow$^{13}C CP-MAS NMR spectra of (a) degummed silk, (b) GNR-silk film prepared by slow drying and (c) further treated with methanol. The deconvolutions of alanine Cβ group were shown at the right side. The ^{13}C resonances at 17.1, 20.3, and 21.7 ppm were assigned to helical/random coil, ordered β-sheet, and disordered β-sheet conformations, respectively[28]. (C) Table showing the fraction of different conformations of silk materials from deconvolution of FTIR spectra. (D) Nanosealant film integrity in saline. The top nanosealants are pristine silk-gold nanorod (S-GNR) films, and the bottom are methanol-treated silk-gold nanorod (mS-GNR) films. Films are dry. (E-H) Saline solution was added to the surface of each nanosealant, and images were taken for 10 minutes. (H) At 10 minutes, the intact mS-GNR films were dried. S-GNR films showed a large extent of dissolution at ten minutes, while mS-GNR nanosealants showed no integrity loss. (I) GNRs leaching from S-GNR and mS-GNR nanosealants as monitored by optical density at 800 nm, indicative of GNRs.

photothermal response of nanosealants. Temperature management mitigates thermal damage in laser-activated photothermal repair, and repair temperature determines tissue strength(Hoffman et al., 2003b; Mushaben et al., 2018). The surface temperatures of nanosealants irradiated at 800 nm with continuous- (CW) or pulsed-wave (PW) laser were imaged with an infrared camera (Figure 34A-D). Nanosealant temperatures increased with laser power density, and temperatures rapidly approached an upper bound with exposure time (Figure 34A). This rapid heating shows that shorter laser exposures are needed for LANS compared to organic dyes(D. Hu et al., 2016). One central drawback to conventional

photothermal repair is peripheral heat damage to surrounding tissue, which can be exacerbated with longer durations of high temperatures. S-GNR nanosealants rapidly cool after laser treatment, suggesting that peripheral thermal damage can be minimized(Mushaben et al., 2018).
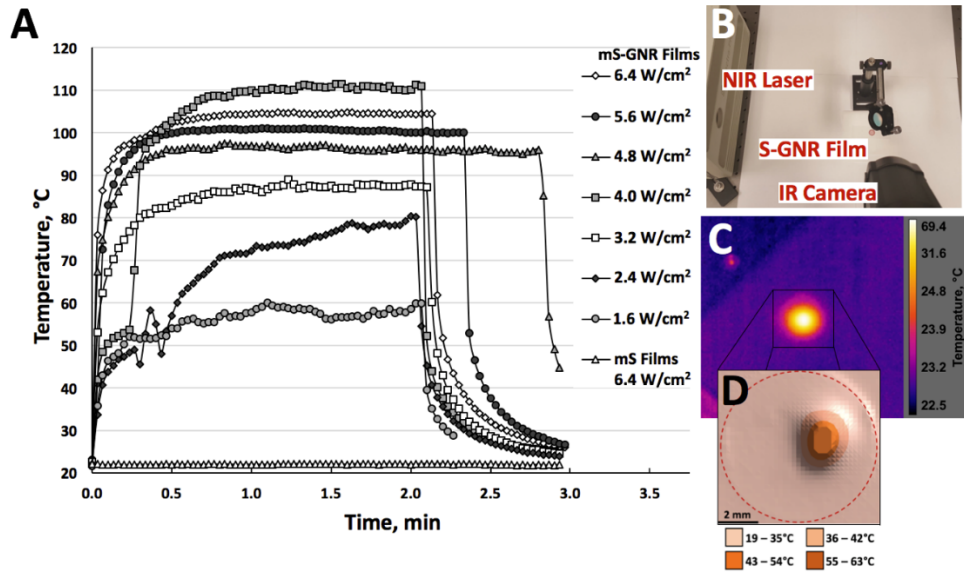
Figure 34. Photothermal response of nanosealants and infrared imaging. (A) Photothermal response of S-GNR nanosealants during irradiation with continuous wave (CW) laser. S-GNR nanosealants were irradiated for two minutes with 800-nm laser at power densities from 1.6 to 6.4 W/cm^2. Following approximately two minutes, the laser was removed, corresponding with rapid decrease in surface temperature. The response of silk films without GNRs (S) to 6.4 W/cm^2 laser is indicated by open triangles. In all cases, the temperature response was determined using images taken by an infrared camera. Curves are representative of n=3 independent experiments. (B) Image of experimental setup with the NIR laser reflected onto the S-GNR nanosealant while thermal data are recorded with an infrared (IR) camera. (C) Representative IR image of the nanosealant being irradiated

with a laser beam. (D) The surface temperature contour plot of the nanosealant from the IR image. Red dotted line is the approximate position of the S-GNR nanosealant.

Protein interdigitation between the nanosealant and tissue cannot adequately occur below 60°C and can weaken above 65°C(Paolo Matteini, Sbrana, et al., 2009). This optimal temperature range was reached at 1.6 W/cm^2 CW laser, or at 2.4 W/cm^2 PW. However, at 3.2 W/cm^2 CW, repair temperatures were reached in just 4 seconds and subsequently exceeded, suggesting that higher laser powers can considerably shorten treatment times. As shown previously(Mushaben et al., 2018; Urie et al., 2015c), greater pulsed laser powers are needed to reach the same temperatures as with CW laser because the nanosealant cools between pulses. By optimizing laser conditions and material parameters, treatment conditions can be optimized for tissue repair. Our recent work indicates that laser-activated tissue repair conditions limit cell death to the tissue underlying the immediate path of the laser(Mushaben et al., 2018). Effective design of sealants and modulation of the laser is therefore critical to ensure minimal thermal damage to tissues.

During colorectal surgery, the tissue is kept moist and flushed often. To mimic a saline drip, saline was dropped onto the mS-GNR nanosealant surface. Laser irradiation generated minimal heat in S and mS films, because silk by itself is not an NIR chromophore (Figure S4.4). When wet, the temperature reached a given laser power decreased significantly, but the repair range of 60-65°C was reached at 4.0 W/cm^2 (Figure S4.4). Silk-GNR nanosealants rapidly convert near infrared light to heat in a dose-dependent manner, and surface temperatures as high as 65°C were reached within 5 seconds of laser exposure at powers as low as 2 W/cm^2. This fluence (10 J/cm^2) is among the lowest fluences reported for an exogenous laser-activated tissue repair material to reach optimal tissue

interdigitation temperatures. The temperature increased more rapidly in mS-GNR than S-GNR nanosealants likely due to water removal by methanol.

methanol-treated silk-gnr nanosealants in *ex vivo* intestine repair. Rapid wound closure is critical to advancing outcomes in surgery(Huh, Kim, & Kim, 2010; Park, 2010b), limiting dehiscence and shortening the inflammatory period. Cadaveric pig intestines were incised and infused with dyed saline while recording burst pressure (Figure 35A-D), which is the pressure prior to failure when pressure drops sharply as the intestine rips open at the seal or needle insertion point, and is a clinically-relevant indicator of the seal strength(B. S. Bleier et al., 2010; Garcia et al., 2009c). Seen in Figure 35E, fluid flowed freely across the unclosed incision (0.03±0.07 psi). In contrast, intact intestine withstood up to 3.8±1.1 psi. Incised intestine closed with interrupted or continuous sutures withstood very little pressure before bursting the suture line (0.2±0.2 and 0.5±0.3 psi, respectively). A clinically-irrelevant number of eight continuous suture passes was needed to maintain a hydroseal with burst pressure similar to that of intact intestine (4.1±0.7 psi). LANS (6.4 W/cm^2 for 6 minutes) returned significant burst pressure, corresponding to temperatures between 65-72°C. Burst pressures of intestine sealed with mS-GNR LANS (3.01±0.7 psi) or collagen-GNR LANS(Urie et al., 2015c) (2.8±0.7 psi) were similar to that of the intact intestine and over seven times greater than those of clinical suturing. Although sutures physically approximate tissue well, they provide only a cursory barrier to fluid flow which is broken by even very low fluid pressures. LANS, in contrast, can withstand much higher fluid pressures, similar to those of the native tissue.

LANS can also be used to reinforce suture lines. The mS-GNR nanosealant was centered over interrupted sutures and lasered (6.4 W/cm^2 for 6 minutes). The sutured and

LANS-sealed intestine held 3.7±0.6 psi, similar to intact intestine. Use of LANS over the suture line significantly improves closure compared to sutures alone, indicating potential to reinforce suture lines in many surgical procedures. Burst pressures increased with laser power density and duration (Figure S4.5), and the difference in burst pressure from 2 to 4 minutes of treatment is larger than that observed from 4 to 6 minutes, suggesting a laser exposure time at which sealing strength approaches a maximum. Burst pressure of native and welded intestine were compared at different infusion rates of 0.25mL/min and 0.5mL/min and were found to be fairly comparable for the two infusion rates at a given power density (Figure S4.6).
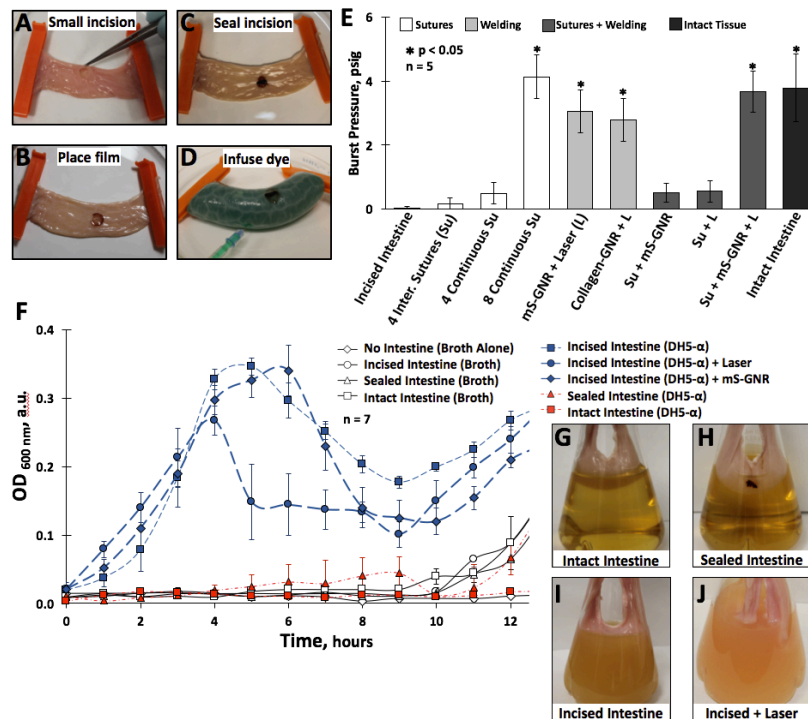
Figure 35. Laser sealing of incised porcine intestine *ex vivo*. (A) An 8mm-length incision is made through one wall of clamped intestinal sections. (B) Incision edges are approximated, and an mS-GNR nanosealant is placed over the incision. (C) The incision is sealed using NIR laser at 6.4 W/cm^2 for 6 minutes. (D) The intestine is infused with dyed

saline to dilate the intestine until rupture. (E) Burst pressures were determined for ruptured, sutured (Su), laser-sealed (L), sutured + laser-sealed, and intact intestine. Burst pressure measurements of native porcine tissue, incised intestine sealed for 6 minutes at 6.4 W/cm^2, incised tissue without sealing, and incised tissue closed by interrupted or continuous sutures, where n=6. Alternatively, no incision was made, and the intact intestine bursting pressure was determined, dilating as the tissue was filled with liquid. (F) Bacterial leakage from the intestinal lumen and subsequent growth. The optical density (OD) of the absorbance at 600 nm light of solutions of LB broth are recorded over 24 hours during incubation at 37°C and 150 rpm (full 24 h profile in SI. Intestinal sections are partially immersed in the broth solution, where the white diamonds are no intestine, white circles are ruptured intestine, white squares are intact intestine(G), and white triangles are sealed intestine with mS-GNR films at 6.4 W/cm^2 for 6 min (H). Blue data sets represent ruptured intestine filled with a DH5-α E. coli bacteria solution and immersed in the LB broth. Ruptured intestine alone (blue squares) (I), ruptured intestine and laser treatment (blue circles) (J), and ruptured intestine where the incision is covered by a silk-GNR nanosealant (blue diamonds).

Anastomotic leakage requires surgical intervention(Eetezadi, Ekdawi, & Allen, 2015); preventing bacterial leakage from sealed colorectal tissue is critical to preventing patient morbidity. Bacteria were introduced into the intestine while suspended in a flask of LB broth (Figure 35F-J, Figure S4.7). The turbidity of the broth was monitored as an indicator of bacterial leakage from the lumen and subsequent growth. Intact intestine, ruptured intestine, and ruptured intestine sealed with an mS-GNR nanosealant at 6.4 W/cm^2 for 6 minutes filled only with sterile broth (not containing bacteria) did not have any

significant bacterial growth over the first 8-12 hours. Growth then occurs rapidly until approximately 20 hours and remains constant over the final 2-4 hours. Because of the rapid increase in turbidity after approximately 12 hours even when no bacteria were introduced, it is likely that existing bacteria are transferred to the media from the intestine itself.

Intact intestine and LANS-sealed intestine filled with DH5-α *E.coli* showed similar growth profiles, with no growth for the first 12 hours. The growth solution of ruptured intestine filled with bacteria, however, showed rapid bacterial growth. Ruptured intestine alone, ruptured intestine treated with laser alone at 6.4 W/cm^2 for 6 minutes (no nanosealant), and ruptured intestine with an mS-GNR film applied over the incision (no laser) showed bacteria growth in the first hour, reaching local maxima at approximately 4 hours. Early growth from unsealed intestines is due to leakage of the DH5-α from the intestinal lumen. Notably, bacterial leakage is not seen in the intact or sealed intestine containing DH5-α bacteria, showing that LANS prevented bacterial leakage from the lumen.

Cadaver porcine intestines were ruptured and sealed using mS-GNR nanosealants with laser, and these sealed intestines showed more than 7-fold increase in sealing efficacy over clinically-relevant suturing and prevented bacterial leakage from the intestinal lumen. These results suggest that nanosealant-based laser sealing can result in rapid hydrosealing for various types of wounds, incisions, anastomoses, or ligations in surgery. In addition to intestine, these results are especially promising for other tissue and surgery models where sutures do not provide a rapid hydroseal. While many adhesives, glues, or sealants fail to adhere or polymerize in wet conditions, these laser-activated nanosealants have application in internal surgical procedures as an alternative to sutures or staples.

skin repair in mice via silk-gnr nanosealants. Dorsal skin incisions on BALB/c mice (Figure 36A-C) were closed by S-GNR nanosealants irradiated at 4.8 W/cm^2 (Figure 36C). Sterile saline was dropped into the wound, and an S-GNR nanosealant film was placed over the moist incision, dissolving the nanosealant into a viscous paste over the incision line. The wound edges were approximated, and the laser was run along the incision at 0.5 mm/sec for 2 minutes, resulting in temperatures between 60-70°C (Figure S4.8). Incisions were alternatively closed by interrupted suture or skin glue with a single stay suture (Figure 36A and B, respectively).

The wound edges of sutured skin were not rejoined (Figure 36G and J) after two days. Although the strength of the sutured skin was 25.1±8.7 kPa (Figure 36M), this strength is likely due to physical approximation by adherent wound exudate removed or dissolved in the fixation process. The epidermis and dermis were separated by a large number of neutrophils, cellular debris, and fibrin, while the adipose tissue and muscularis had moderate numbers of neutrophils. Skin closed by commercial glue + a stay suture resulted in similar strength after two days (Figure 36H and K), though the wound margins were connected with few spindloid cells and minimal collagen at subcutis. The epidermis and dermis were separated with large numbers of neutrophils, cellular debris, and fibrin, and the overlying glue was separate from the epidermis with large numbers of neutrophils and cell debris while the dermis contained fewer neutrophils. The skin glue elicited a lesser inflammatory response in the dermis than the silk or PGA sutures but a qualitatively greater response in the epidermis. A stay suture with the skin glue group was required to hold the incision closed in these studies.
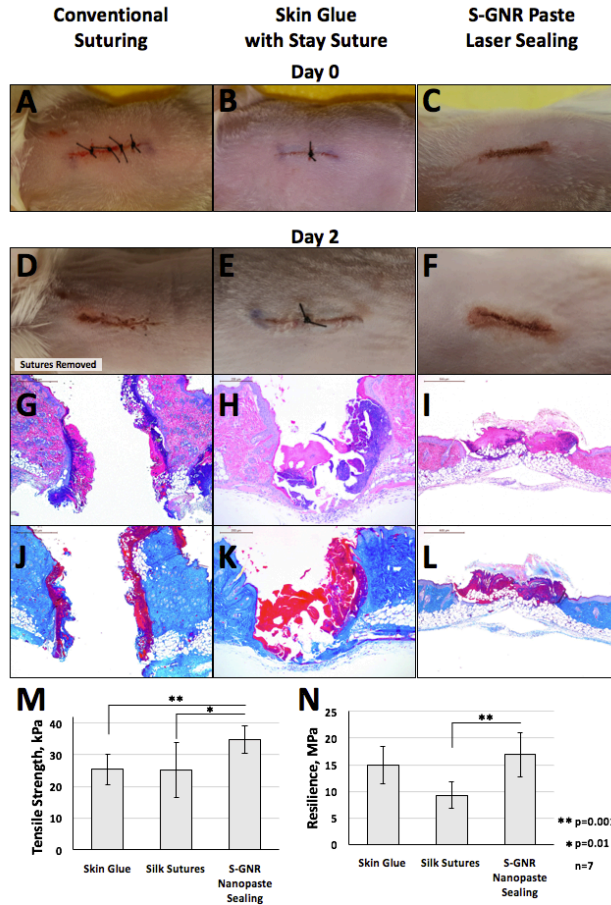
Figure 36. Skin incision healing in live BALB/c mice 2 days after treatment. Left column: Skin incision closure by commercial silk suture, 4 interrupted knots. Center column: incision closure with skin glue and one centered stay suture. Right column: incisions are sealed with S-GNR paste and laser at 4.8 W/cm^2 for 2 min. (A-C) Skin incisions immediately following surgery. (D-F) Skin incisions 2 days after surgery. (G-I) Formalin-fixed tissue sections stained with hematoxylin & eosin. (J-L) Formalin-fixed tissue sections stained with Masson's trichrome. (M) Tensile strength of treated skin incisions two days following surgery, where n=7. (N) Resilience of treated skin incisions two days following surgery, where n=7.

Laser-activated S-GNR paste significantly increased skin strength (34.6±4.3 kPa) after two days, with continuous underlying adipose tissue. The epidermis and dermis are separated with fewer neutrophils, cellular debris, and fibrin than sutured or glued skin, and the overlying nanosealant material is separate from the epidermis with lower numbers of neutrophils and cellular debris than in sutured or glued skin. The dermis and the adipose tissue also have smaller numbers of scattered neutrophils. These results indicate that the LANS-repaired skin elicits a lower inflammatory response while simultaneously bridging the incision more completely than suturing or gluing skin after 2 days. Eventually a porcine model will be needed to study healing in the absence of skin contractile forces that are present in murine skin and to study scarring results for translation to human skin. Briefly, the resilience of the incised skin closed by these three methods indicates that failure occurred in a similar manner for each (Figure 36N and Figure S4.9).

After four days, the wound margins appeared qualitatively less defined in the sutured and LANS-sealed skin than the glued skin (Figure 37A-C). Additionally, glue caused the incision site to become rigid and brittle, which did not occur after lasering the S-GNR paste nanosealant. Only partial-thickness continuity was shown by skin glue treatment after 4 days, while the sutured and laser-sealed skin samples show full-thickness tissue continuity (Figure 37G-I), accounting for the treatment groups being similar in tensile strength, compared to significant differences in strength after 2 days. Mouse skin heals by contraction and therefore the earlier time points (i.e. day 2) are of key significance in determining the efficacy of the repair approach.
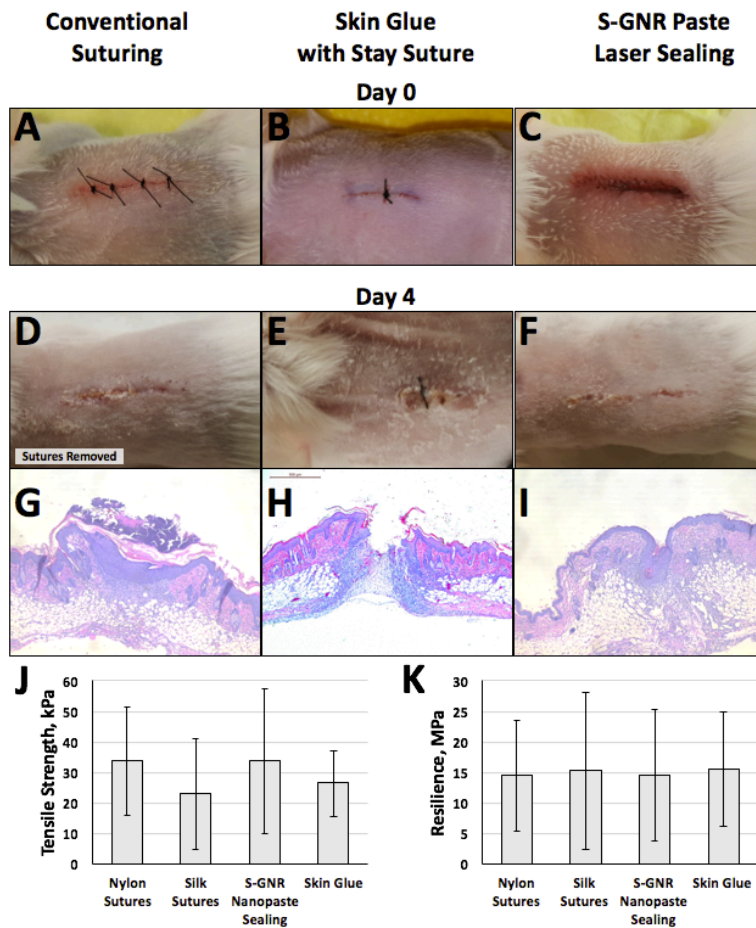
Figure 37. BALB/c Mouse Skin Incision Healing After 4 Days. Left Column, Skin incision closure by commercial silk suture ("conventional suturing"), 4 interrupted knots. Center Column, incision closure with skin glue and one centered stay suture. Right Column, incisions are sealed with S-GNR paste and laser at 4.8 W/cm^2 for 2 min. (A-C) Skin incisions immediately following surgery. Of note, the silk-GNR paste has a maroon color, which is seen in the skin incision and may be misconstrued as blood. (D-F) Skin incisions 4 days after surgery. (G-I) Formalin-fixed tissue sections stained with hematoxylin & eosin. (J) Tensile strength of treated skin incisions two days following surgery, where n=3. (K) Resilience of treated skin incisions two days following surgery, where n=3.

The incision disruption in the epidermis of sutured skin (Figure 37G) was overlain with fibrin clot, neutrophils, and cellular debris. In the dermis, subacute inflammation was evidenced by infiltration of large numbers of neutrophils and macrophages and lower numbers of lymphocytes, edema, and fibrin deposition. The skin closed with glue and a stay suture was mildly connected with few spindloid cells and minimal collagen (Figure 37H). The overlying glue partially adhered to the epidermis, with neutrophils and cell debris. The epidermis of the incision margins was not fused. The dermis contained small numbers of neutrophils.

The skin closed via S-GNR paste LANS (Figure 37I) showed marked subacute inflammation in the dermis. The disruption at the epidermis, however, was significantly smaller than sutured or glued skin, suggesting more rapid reepithelization and healing. The amount of exudate surrounding the wound was also reduced, indicating less inflammation or an advanced stage of healing. Overall, laser tissue repair with silk-GNR nanosealants increased the rate and extent of regeneration of the epidermis with lowered inflammation. Similar results were found in C57Bl6 mice (Figure S4.10).

Conclusions

Silk-GNR nanosealants were generated as thin films, and employed methanol treatment to alter their mechanical properties including solubility, tensile strength, and elasticity. These modifications serve to modulate nanosealant properties for internal or superficial tissue repair. Insoluble silk-GNR sealants efficiently convert NIR light to heat, providing a rapid hydroseal in cadaveric intestines that holds seven-fold fluid pressure to sutures and prevents bacterial leakage. Soluble silk-gold nanorod sealant pastes also convert laser light to heat and close skin incisions more rapidly and with less inflammation

than clinical suturing or skin glue. Silk-GNR nanosealant closed murine skin incisions *in vivo*, with a ~40% increase in skin tensile strength over sutured skin two days post-surgery. The laser-activated nanosealant approach also increased the rate of regeneration of the disrupted epidermis. This work shows that advances in exogenous chromophores, tissue-integrating nanomaterials, and heat management make laser-activated tissue repair a viable platform technology for ubiquitous use in medicine and surgery. The performance of these nanosealants highlights the need for further next generation photosensitizing materials in tissue repair and regeneration, and multi-wavelength absorption, adhesive chemistry, drug loading, and photochemical bonding will drive improvements to laser-activated tissue repair.

LASER ACTIVATED NANOGLUES FOR PREVENTING SURGICAL SITE INFECTION

Introduction

Over the last 50 years, surgical procedures have significantly increased in frequency, complexity, and invasiveness(Anderson, 2011). Surgical site infections (SSIs) occur in 2-5% of surgical patients in the US, impacting 300,000-500,000 lives each year(Anderson, 2011). SSIs are the most common and costly healthcare-associated infections, accounting for $3-10 billion/year in healthcare expenditure and posing a 2-11 fold greater risk of death compared to patients without SSIs(Anderson et al., 2014). The most common infectious agent is *Staphylococcus aureus,* which occurs in 20% of SSIs among hospitals that report to the CDC and 37% among the community hospitals; methicillin-resistant *S. aureus* (MRSA) is the most common pathogen in community hospitals(Anderson, 2011). Clinical recommendations for SSI prevention include parenteral antimicrobial prophylaxis, perioperative glycemic control, and normothermia. Despite improvements in surgical techniques, administration of antimicrobial prophylaxis, and surveillance protocols, SSIs remain a huge challenge(Anderson et al., 2014; Tajirian & Goldberg, 2010b); no recommendation is provided regarding antimicrobial dressings or sealants applied after primary closure in the operating room(Berríos-Torres et al., 2017). There is an urgent need to prevent and treat SSIs efficiently to decrease time and costs associated with recovery and reduce mortality, and best technologies and practices for combating SSIs need to be urgently identified.

Materials used for skin closure such as absorbable and non-absorbable sutures, staples, and tissue adhesives vary in tensile strength, immune response, and resistance to

infection(Tajirian & Goldberg, 2010b). Sutures have been used for millennia but are associated with risk of infection, wound dehiscence, require significant surgical skill and time, are traumatic, and may not be feasible for inaccessible or friable tissue(Gurusamy, Toon, Allen, & Davidson, 2014; Paolo Matteini, Ratto, Rossi, Centi, et al., 2010; Seiler et al., 2009; Urie et al., 2018). Staples can result in malapposition of wound edges, causing scarring and trauma(Edlich et al., 2010; Urie et al., 2018). Tissue adhesives provide faster, less painful closure but cannot be used alone in areas of high tension and may demonstrate poor adhesion, toxicity, or delayed cell migration(Jeon et al., 2015; Tajirian & Goldberg, 2010b; Yeung et al., 2016). Additionally, there is some preliminary evidence that tissue adhesives may augment wound closure and resist local infection in diabetic and immunodeficient patients(Frykberg & Banks, 2015; Piaggesi et al., 2010). Although there have been studies showing the efficacy of biosealants such as fibrin, there is currently no conclusive evidence regarding the efficacy of microbial sealants in preventing SSIs(Falk-Brynhildsen, Söderquist, Friberg, & Nilsson, 2014; Ikossi-O'Connor, Ambrus, & Rao, 1983; Organization, 2016). For example, in spine surgeries, opportunistic SSIs can lead to devastating complications, including slow-healing/chronic wounds(Piper et al., 2017). Antibiotic-coated sutures have provided mixed/unclear efficacies depending on use(Edmiston Jr, Daoud, & Leaper, 2013; Elsolh, Zhang, & Patel, 2017). Clinically, vancomycin is used prophylactically to combat SSIs including in spine surgery(Lemans et al., 2019). Although some benefit is seen, the overall efficacy and optimal application method are unclear(Bakhsheshian, Dahdaleh, Lam, Savage, & Smith, 2015; Hall, 2015).

To overcome the limitations of commercial adhesives and dressings, anti-microbial, laser-activated sealants were developed which seal wounds using exogenous

chromophores that convert near-infrared (NIR) light to heat. Tissue sealing using laser energy has been attributed to a photothermal effect resulting in restructuring of the extracellular matrix, collagen homogenization, and interdigitation of collagen fibrils(Constantinescu et al., 2007c; L. W. Murray et al., 1989b). NIR light operates in the therapeutic window (700-1300 nm) of biological tissues and has been used for laser sealing of vascular structures(O'neill et al., 2007; Xie et al., 2004) and other tissues. In previous work, silk-GNR laser-activated nanoglues (LANGs) were developed for rapidly sealing skin incisions and prevented bacterial leakage in intestines(Urie et al., 2018). These studies suggest the transformative role of tissue sealing using NIR lasers for preventing SSIs, especially in immunocompetent and diabetic patients.

In this work, novel silk-silver nanoprism and silk-indocyanine green LANGs rapidly seal tissue and also act as depots for extended release of antibacterials (e.g. vancomycin) in a skin incision model for wound closure in spine surgeries. These pathologies are at high risk for SSIs(Martin et al., 2016; Sadoskas, Suder, & Wukich, 2016; Wukich, McMillen, Lowery, & Frykberg, 2011) and local or systemic antibiotics are clinically recommended for SSI prevention and treatment(Sadoskas et al., 2016). Silver nanoprisms (AgNPs) exhibit efficient antimicrobial activity(Panáček et al., 2006; Rai, Deshmukh, Ingle, & Gade, 2012) and shape-dependent absorption of NIR light, generating heat(Jin et al., 2001; Millstone, Hurst, Metraux, Cutler, & Mirkin, 2009; Q. Zhang, Li, Goebl, Lu, & Yin, 2011). Sealing efficiency, anti-microbial efficacy, and laser-induced temperature response were determined for these LANGs.

Materials and Methods

materials. Cetyltrimethylammonium bromide (CTAB) was purchased from BP Chemicals (Santa Ana, CA). $NaBH_4$, $HAuCl_4\bullet3(H_2O)$, $AgNO_3$, L-ascorbic acid, cardiogreen (indocyanine green or ICG), trisodium citrate, and polyethylene glycol (PEG, MW 3350 gm/mol) were purchased from Sigma-Aldrich (St. Louis, MO). Vancomycin was purchased from Chem-Impex Int'l (Wood Dale, IL). Nanopure water was obtained from a Millipore filtration system (Darmstadt, Germany) with 18.2 MΩ-cm resistivity. To maintain integrity, $HAuCl_4\cdot3H_2O$ and vancomycin were kept at 0°C, and CTAB solutions were maintained at 27°C. Other reagents were maintained at room temperature.

nanoparticle synthesis. Gold nanorods (GNRs) were prepared via a seedless growth method(Ali et al., 2012). 5 mL of 1 mM $HAuCl_4$ were added to 5 mL of 0.2 M CTAB and 8 μL of 12.1 M HCl (37% w/w). $AgNO_3$ (200 μL) and freshly-dissolved ascorbic acid (70 μL, 78.8 mM) were added and then gently mixed until turning colorless. Cold $NaBH_4$ (15 μL, 10 mM) was then added immediately. The dispersion was incubated at 27°C for 6 hours and then centrifuged at 14,000 rpm for 30 minutes and redispersed in water three times.

Silver nanoprisms (AgNPs) were prepared via direct chemical reduction(Q. Zhang et al., 2011). With a total reaction volume of 20 mL, 19.272 aqueous solution at 4°C had the following chemicals added: $AgNO_3$ (40 μL, 50 mM), trisodium citrate (0.4 mL, 75 mM), PEG (120 μL, 6wt%), and H_2O_2 (48 μL, 30%). The solution was vigorously stirred, and $NaBH_4$ (120 μL, 100 mM) was quickly added during the mixing. At this point the solution turned a slight yellow color. The solution was stirred vigorously for several hours. After ~30 minutes, the solution turned a deep gold color. After another ~60 minutes, the

solution turned a deep blue. The nanoparticle synthesis was concluded after approximately 4 hours.

laser-activated nanoglue formulations. Silk fibroin was extracted from *Bombyx mori* silk cocoons(C. Guo et al., 2015; Rockwood et al., 2011). In brief, cocoons were cut up and washed in water, boiled in 0.5 wt% Na_2CO_3 for 30 minutes, washed in water three times, and dried at room temperature. 2 grams of degummed silk fibers were dissolved in 10 mL of 9.4M lithium bromide (LiBr) at 60°C for four hours, centrifuged to separate insoluble contents, and dialyzed for 72 hours at 4°C against a 3.5 kDa membrane to remove LiBr and impurities. Dialysate water was changed daily. The silk was centrifuged at 14,000 rpm for 30 minutes to remove remaining impurities. The solution was then stored at 4°C until use.

To prepare silk LANG films, ICG or a nanoparticle dispersion was added to the 6 wt% purified silk fibroin solution and gently mixed until homogenous at 4°C. Approximately 0.5 mL of the silk mixture was evenly-pipetted into 1 cm x 1 cm plastic slides and dried overnight at room temperature. Three silk LANGs were used in this study: pristine silk films (pS), silk films embedded with GNRs (S-GNR), silk films embedded with AgNPs (S-AgNP), and silk films loaded with ICG (S-ICG). Each of these film types were also potentially loaded with free vancomycin (Vanc). A silk film embedded with 1 wt% AgNPs and loaded with 100 μg vancomycin, for example, is hereafter referred to as S-AgNP(2wt%)-Vanc(100μg).

characterization of photothermal response. LANG films were tested for absorbance across a spectrum from 300-1000 nm with a Synergy 2 Multi-Mode Reader (BioTek Instruments; Winooski, VT). The photothermal response of different

chromophore concentrations in LANGs was assessed using continuous-wave laser at varying powers to determine the optimum laser power for tissue sealing. Protein interdigitation between the LANG and tissue occurs between 60-65ºC. A photothermal response will determine the laser power required to attain this temperature[5]. S-AgNP LANGs were irradiated with laser power densities between 0.5-6.5 W/cm^2 for up to two minutes using continuous-wave (CW) laser, and the temperature response was determined using an IR camera[5]. Laser power densities resulting in LANG temperatures of 60 ºC along the incision in the minimum time were used for subsequent *in vivo* studies.

in vitro **bacterial inhibition.** MRSA USA300 (LAC), the most common community-associated *MRSA* strain in the U.S.(Anderson, 2011), was grown in trypticase soy broth (TSB) or on trypticase soy agar (TSA). Cultures were grown from frozen glycerol stocks for 17-19 hours overnight at 37°C with gentle rotary mixing and then diluted 1:40 in fresh media for growth to mid-logarithmic phase at 37°C for 2.5 hours of gentle mixing.

The bactericidal effects of various LANGs were evaluated on Mueller-Hinton agar for MRSA inhibition using a disk diffusion susceptibility assay, and the zone of inhibition was measured(Balouiri, Sadiki, & Ibnsouda, 2016). A cell density of $2x10^8$ CFU/mL was used as the inoculum, and commercial antimicrobial doxycycline disks (30 µg/mL, Becton Dickinson, NJ) served as a positive control(Islam, Ahmed, & Rahman, 2013; Reller, Weinstein, Jorgensen, & Ferraro, 2009). 5 mg of LANG film was cut and dissolved in 20 µL and compared to the doxycycline control. LANG paste or nanoparticle dispersion (20 µL) was pipetted onto the agar. The plates were incubated at 37°C after *MRSA* inoculation onto the agar surface, addition of the LANG pastes and nanoparticle dispersions, and placement of control antibiotic disks. Zones of inhibition were measured after 24 hours.

Since the pastes, surface suspensions, and antibiotic disks differ in diameter, four quadrant radius measurements were averaged for each zone. To determine diameters, radius measurements were doubled and disk width (6 mm) was added. All agar diffusion assays were performed at least three times. Prior to use, all LANG materials were UV sterilized.

In a broth assay of antibacterial susceptibility, exponential phase *MRSA* cultures were adjusted to an OD_{600} of 0.068 in PBS. Bacterial suspensions (100 µL) in cation-adjusted Mueller Hinton broth (CAMHB) (900 µL) were added to wells of 24-well plates containing lasered LANG films, nanoparticle suspensions, or free vancomycin (2 µg/mL) at its minimum inhibitory concentration for *MRSA*("Vancomycin (Vancocyn, Lyphocin) | The Antimicrobial Index Knowledgebase—TOKU-E," n.d.). Bacterial growth was determined via photos of visual turbidity and absorbance at 600 nm for up to 5 days standing incubation at 37°C. LANG films were lasered to prevent dissolution during the bacterial growth assay. Cell viability was determined by plating duplicate 10-fold serial dilutions for samples in question onto Mueller Hinton agar plates and enumerating colonies after 16 hours of incubation at 37°C.

in vivo **bacterial inhibition.** Full-thickness skin incisions (0.75 cm) were generated on the backs of male and female BALB/c immunocompetent mice *in vivo*. These incisions were closed using suture, vetbond, or LANGs in the presence or absence of NIR laser (Figure 38). Closed wounds were then topically inoculated with 10^5 Colony Forming Units (CFU) of *MRSA*. *MRSA* SQ was cultured for 16 hours in TSB rotating, rinsed in 0.9% saline, resuspended to OD_{600} of 0.07, and put on ice until inoculation. After incision closure. 20µL of MRSA culture placed directly on incision. Mice were euthanized 7- or 14-days post-infection. The following groups were evaluated: (1) S-GNR LANGs, (2) S-

AgNP LANGs, (3) S-ICG LANGs, (4) S-ICG-Vanc LANGs, (5) simple interrupted Vicryl Plus suture, and (6) commercial Vetbond skin glue with a stay suture. Full thickness cutaneous wounds from the controls and treated samples were collected for histology (H & E) and CFU measurements.
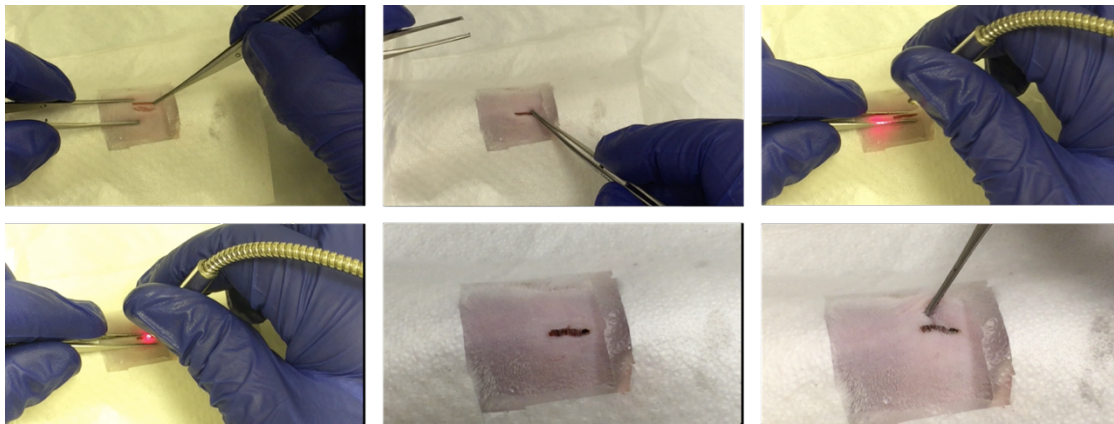
Figure 38. Skin incision closure using LANGs. A small incision is placed on the back of a mouse and kept moist. A LANG is placed within the incision bed and allowed to dissolve into a paste. The wound margins are then gently pressed closed while the incision line is irradiated with NIR laser.

To harvest the dorsal skin tissue, 1 cm by 2 cm pieces were taken around the incision and cut into halves (perpendicular to the incision). For initial load, each half was processed. To process, top (cranial) halves of tissue were placed in microcentrifuge tubes with autoclaved 0.6mm steel homogenization beads and 200 μL sterile saline before processing in a Bullet Blender (2X5 min at speed setting #6). Homogenate volume was brought to 0.5 mL (by visual tube markings) before being serially diluted 1:5 (twice) and each dilution plated in duplicate.

Results and Discussion

lang formation and characterization. I previously synthesized silk-GNR and collagen-GNR LANGs as flexible films or viscous pastes. In this work, silk-GNRs were generated as previously described(Urie et al., 2018). Novel silk-AgNP and silk-ICG LANGs were also used in sealing skin incisions (Figure 39A-C). AgNPs were synthesized triangular in shape with an average size of 30 nm (Figure S5.1). Silk-GNR (S-GNR), S-AgNP, and S-ICG LANGs all display a characteristic plasmonic resonance peak at 800 nm (Figure 39D).

S-GNR, S-AgNP, and S-ICG LANGs all generate heat in response to NIR laser, and their temperatures rapidly with laser power density (Figure 40). The ideal temperature for protein interdigitation between LANG and the tissue is 60-65ºC. The laser power density can be adjusted to optimize the photothermal response of LANGs for effective tissue approximation, repair, and minimum thermal damage of tissues (see Figure S4.4).
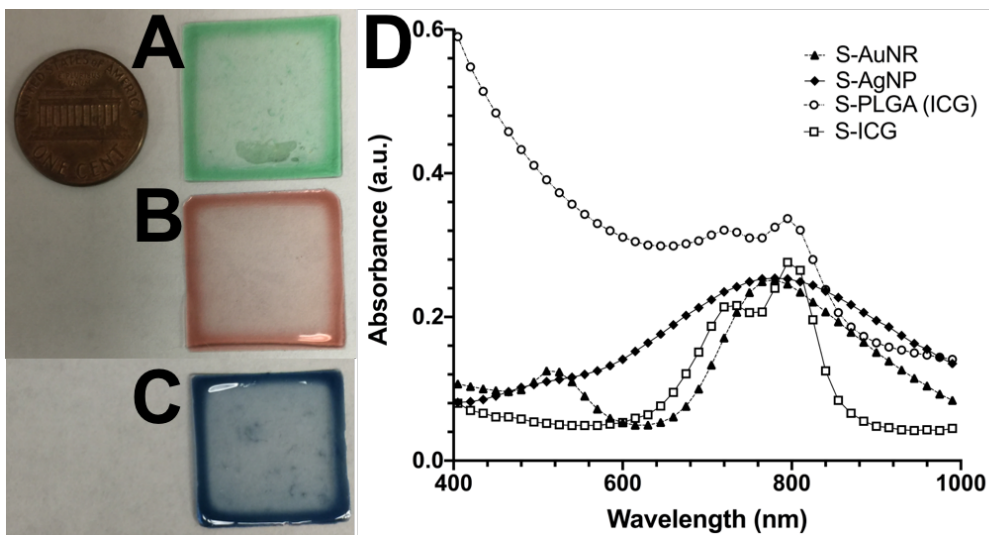
Figure 39. Photothermal Characterization of LANGs. (A) Silk-ICG LANG film. (B) Silk-GNR LANG film. (C) Silk-AgNP LANG film. (D) Absorbance spectra of LANG films. Representative curves of three independent experiments.

127
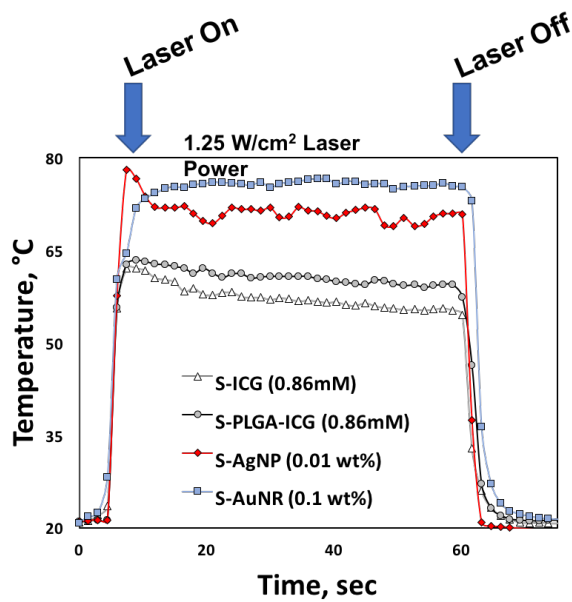
Figure 40. Laser photothermal response of LANG films. Laser photothermal response of LANG films. Films irradiated with 1.25 W/cm^2 NIR laser for approximately 30 seconds. Representative curves of three independent experiments.

anti-bacterial activity of langs *in vitro* and *in vivo*. In disk diffusion assays, LANG films were dissolved into pastes, as is the case when skin closure was performed *in vivo*. These LANG pastes were assessed on the agar plates for their zone of inhibition of *MRSA* growth. As shown in Figure 41, pristine silk (pS) showed no zone of inhibition. S-GNR and S-GNR-AgNP LANGs showed a small zone of inhibition, though S-AgNP LANGs, interestingly, did not inhibit growth. Aqueous dispersion of GNRs (no silk present) also inhibited growth, suggesting that perhaps the small concentration of free CTAB still present following GNR synthesis is inhibiting growth. This would logically explain why the GNR dispersion inhibited growth in a wider zone than the S-GNR or S-GNR-AgNP LANGs, as the dispersion likely contains a higher concentration of free CTAB. As the S-AgNP LANGs unexpectedly did not show a zone of inhibition over this

24-hour assay, subsequent broth assays were performed at increased AgNP concentrations and time lengths to find a minimum inhibitory concentration (MIC).
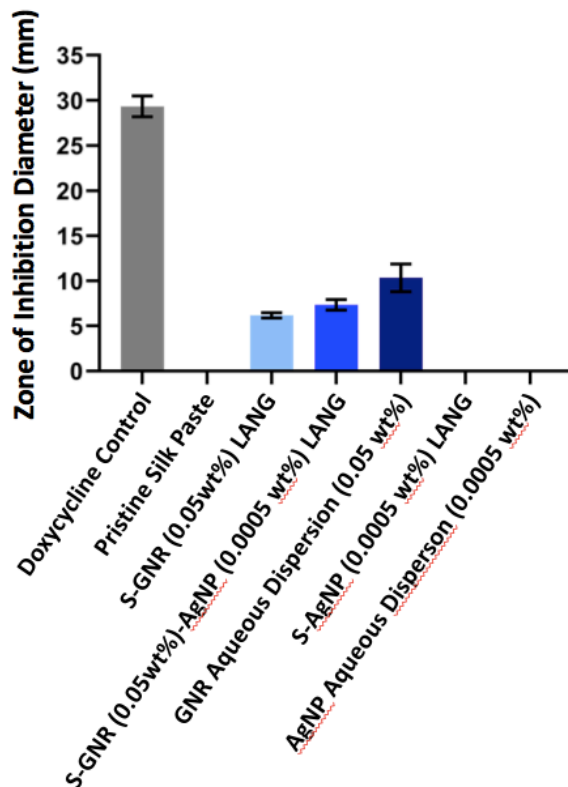
Figure 41. MRSA inhibition efficacy of nanoparticles via disk diffusion assay. Doxycycline 30 mg/mL disk as a positive control, pristine silk film as a negative control (n=3).

In a broth antibacterial susceptibility assay, Vicryl Plus suture was shown to have minimal inhibition of growth, as evidenced by turbidity similar to the *MRSA* growth control (Figure 42). S-AgNP(1.0wt%) lasered LANG films similarly did not inhibit *MRSA* growth, indicating that even the high concentration of 1.0wt% AgNPs was not sufficient to generate ample silver ions for antibacterial activity, or that the silver ions were in some way inactivated due to the presence of the silk fibroin. On the other hand, S-AgNP(1.0wt%)-

Vanc(1600µg) and S-ICG(0.86mM)-Vanc(1600µg) both inhibit MRSA growth similar to the MIC vancomycin control (2µg/mL).
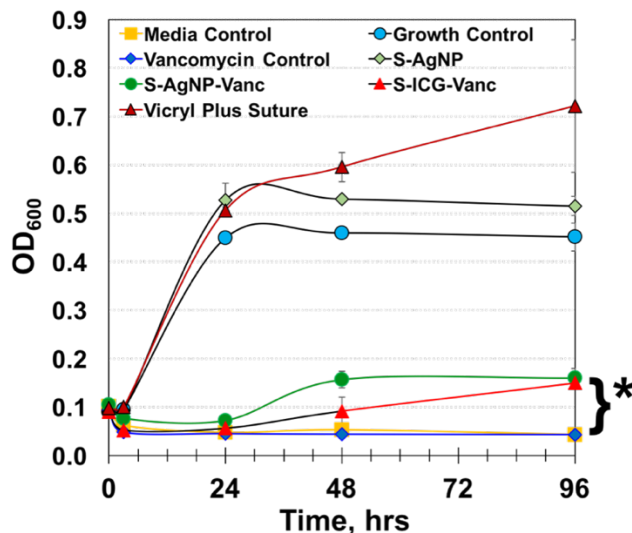
Figure 42. MRSA inhibition efficacy of nanoparticles via broth assay. MRSA growth as indicated by growth solution turbidity (OD at 600 nm), given lasered LANG films present in growth solution (n=3).

To determine the MIC of vancomycin in S-ICG-Vanc LANGs, additional antibacterial susceptibility assays were performed. All S-ICG-Vanc LANGs at various vancomycin amounts (ranging from 25 µg to 1000 µg) prevented turbidity in the MRSA growth solution with the exception of one replicate of the lowest concentration (25 µg) (Figure 43). As a result, the next-lowest concentration (50 µg) was used *in vivo*.

Dorsal skin incisions of BALB/c mice were closed by simple interrupted Vicryl Plus suture, commercial skin glue with a stay suture, or lasered LANGs. After incisions in mice skin, closure groups were as follows: (1) sutured, *MRSA* inoculation; (2) nanoglued S-ICG-Vanc(5 µg) LANG), MRSA inoculation (Figure 44A). Two mice were euthanized 1 h post inoculation to determine MRSA bacterial load (avg 4.5 x 10^5 CFU/g) (Figure 44B).

Mice with LANG-sealed incisions had reduced MRSA loads compared to sutured incisions (Figure 44C). Despite higher bacterial loads with sutured incisions, no gross signs of wound infection were observed.
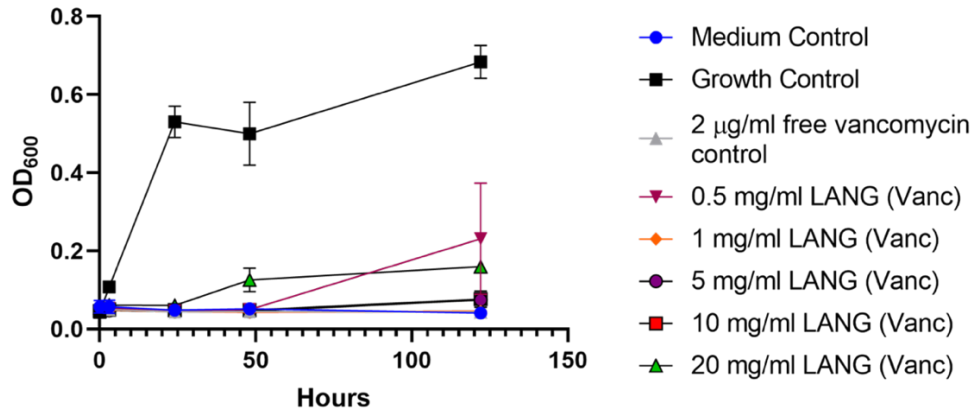

Figure 43. MRSA inhibition efficacy of vancomycin via broth assay. MRSA growth as indicated by growth solution turbidity (OD at 600 nm), given lasered LANG films present in growth solution (n=3).

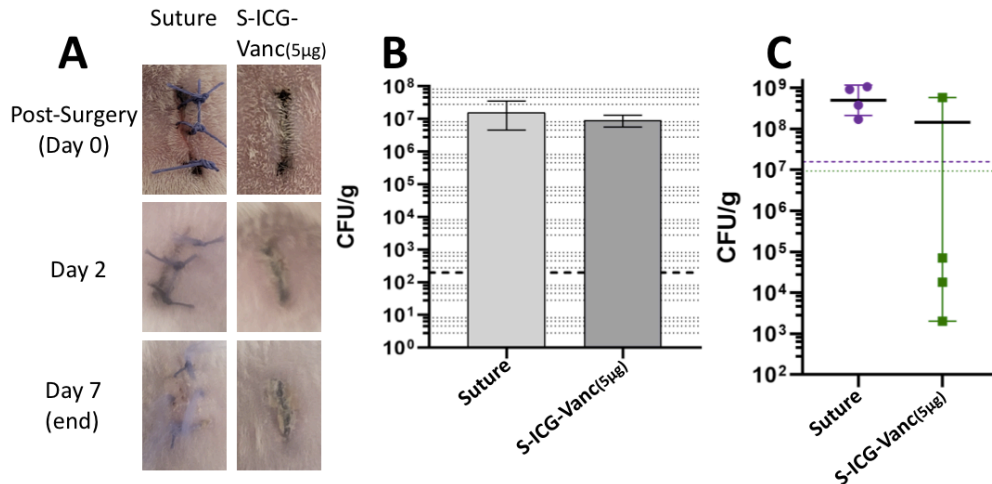**Figure 44.** Dorsal murine skin healing. (A) Dorsal skin incisions (1 cm) were made on the back of BALB/c mice and incisions were closed using Vicryl Plus antibiotic suture or S-ICG-Vanc(5 μg) LANG (n=4). (B) MRSA bacterial load one hour post- inoculation (n=1).

(C) MRSA bacterial load 7 days post-inoculation, dotted lines indicate 1-hour bacterial loads (n=4).

Future Work

Skin inflammatory response following *MRSA* infection and use of LANGs will be evaluated by monitoring TNF-α, IFN-α, IFN-β, IL-1α, macrophage inflammatory protein 2 (MIP-2), IL-6, and IL-8 protein levels using ELISAs. Total collagen will be assessed to evaluate healing using trichome staining. Blood will be collected from mice following euthanasia and plasma levels of C-reactive protein, fibrinogen, fibronectin, and von Willebrand factor (VWF) will be measured using ELISA to evaluate inflammation and endothelial injury markers. TUNEL assay will be used to evaluate apoptotic cells. The efficacy of LANGs will also be evaluated in immunodeficient and diabetic mice, since these patients remain at a significantly higher risk for SSIs.

Conclusions

The effectiveness of silk-GNR, silk-AgNP, and silk-ICG laser-activated nanoglues (LANGs) for tissue sealing and MRSA control were compared in immunocompetent BALB/c mice using a skin incision model. Gold nanorods, silver nanoprisms, indocyanine green, and vancomycin in LANGs were evaluated using antibacterial susceptibility assays. The goal of this work was to evaluate LANGs for their efficacy for tissue sealing as well as prevention and control of *MRSA* infection in immunocompetent mice. Laser tissue sealing with silk-indocyanine green-vancomycin LANGs resulted in a greater reduction of the MRSA infection in incised mice skin compared to sutured skin.

Novel LANGs simultaneously seal soft tissues, combat surgical site infections (SSIs), and augment tissue healing. Current clinical practices to treat traumatic lacerations

such as sutures, adhesives, tape, or staples are susceptible to infection and wound dehiscence(Tajirian & Goldberg, 2010b). There exists an urgent need to prevent and treat SSIs efficiently to decrease patient mortality, time, and costs associated with recovery. To address this clinically unmet need, nanoglues were developed that provide a leak-proof tissue seal following laser irradiation, thereby preventing the infiltration of microorganisms into the surgical site. Novel silk materials were developed containing the chromophore indocyanine green and vancomycin that can be activated by near-infrared laser with the ability to seal lacerations rapidly and combat dermal bacterial infection, including those that are caused by MRSA. LANGs seal and protect the wound site from infections.

REFERENCES

Abergel, R., & Meeker, C. (1984). Nonthermal effects of Nd: YAG laser on biological functions of human skin fibroblasts in culture. Lasers in Surgery ….

Abou Neel, E. A., Cheema, U., Knowles, J. C., Brown, R. A., & Nazhat, S. N. (2006). Use of multiple unconfined compression for control of collagen gel scaffold density and mechanical properties. Soft Matter, 2(11), 986. https://doi.org/10.1039/b609784g

Akbik, D., Ghadiri, M., Chrzanowski, W., & Rohanizadeh, R. (2014). Curcumin as a wound healing agent. Life Sciences, 116(1), 1–7. https://doi.org/10.1016/j.lfs.2014.08.016

Akturk, O., Kismet, K., Yasti, A. C., Kuru, S., Duymus, M. E., Kaya, F., … Keskin, D. (2016). Collagen/gold nanoparticle nanocomposites: A potential skin wound healing biomaterial. Journal of Biomaterials Applications, 31(2), 283–301. https://doi.org/10.1177/0885328216644536

Alencar, H., Funovics, M., & Figueiredo, J. (2007). Colonic Adenocarcinomas: Near-Infrared Microcatheter Imaging of Smart Probes for Early Detection—Study in Mice 1. Radiology.

Algarrahi, K., Franck, D., Ghezzi, C., Cristofaro, V., Yang, X., Sullivan, M. P., … Mauney, J. R. (2015). Acellular Bi-Layer Silk Fibroin Scaffolds Support Functional Tissue Regeneration in a Rat Model of Onlay Esophagoplasty. Biomaterials, 53, 149–159. https://doi.org/10.1016/j.biomaterials.2015.02.092

Ali, M. R. K., Snyder, B., & El-Sayed, M. A. (2012). Synthesis and Optical Properties of Small Au Nanorods Using a Seedless Growth Technique. Langmuir, 28(25), 9807–9815. https://doi.org/10.1021/la301387p

Almeida, J. P. M., Chen, A. L., Foster, A., & Drezek, R. (2011). In vivo biodistribution of nanoparticles. Nanomedicine, 6(5), 815–835. https://doi.org/10.2217/NNM.11.79

Alster, T., & Zaulyanov-Scanlon, L. (2007a). Laser Scar Revision: A Review. Dermatologic Surgery, 33(2), 131–140. https://doi.org/10.1111/j.1524-4725.2006.33030.x

Anderson, D. J. (2011). Surgical site infections. Infectious Disease Clinics of North America, 25(1), 135–153.

Anderson, D. J., Podgorny, K., Berrios-Torres, S. I., Bratzler, D. W., Dellinger, E. P., Greene, L., … Maragakis, L. L. (2014). Strategies to prevent surgical site infections in acute care hospitals: 2014 update. Infection Control & Hospital Epidemiology, 35(S2), S66–S88.

Annabi, N., Tamayol, A., Shin, S. R., Ghaemmaghami, A. M., Peppas, N. A., & Khademhosseini, A. (2014). Surgical materials: Current challenges and nano-enabled solutions. Nano Today, 9(5), 574–589. https://doi.org/10.1016/j.nantod.2014.09.006

Annabi, N., Yue, K., Tamayol, A., & Khademhosseini, A. (2015). Elastic sealants for surgical applications. European Journal of Pharmaceutics and Biopharmaceutics, 95, 27–39. https://doi.org/10.1016/j.ejpb.2015.05.022

Archana, D., Singh, B. K., Dutta, J., & Dutta, P. K. (2015). Chitosan-PVP-nano silver oxide wound dressing: In vitro and in vivo evaluation. International Journal of Biological Macromolecules, 73, 49–57. https://doi.org/10.1016/j.ijbiomac.2014.10.055

Armitage, J., & Lockwood, S. (2011). Skin incisions and wound closure. Surgery (Oxford), 29(10), 496–501. https://doi.org/10.1016/j.mpsur.2011.06.022

Asakura, T., Sato, Y., & Aoki, A. (2015). Stretching-Induced Conformational Transition of the Crystalline and Noncrystalline Domains of 13C-Labeled Bombyx mori Silk Fibroin Monitored by Solid State NMR. Macromolecules, 48(16), 5761–5769. https://doi.org/10.1021/acs.macromol.5b01365

Atalay, M., Oksala, N., Lappalainen, J., Laaksonen, D. E., Sen, C. K., & Roy, S. (2009a). Heat shock proteins in diabetes and wound healing. Current Protein & Peptide Science, 10(1), 85.

Bakhsheshian, J., Dahdaleh, N. S., Lam, S. K., Savage, J. W., & Smith, Z. A. (2015). The use of vancomycin powder in modern spine surgery: Systematic review and meta-analysis of the clinical evidence. World Neurosurgery, 83(5), 816–823.

Balouiri, M., Sadiki, M., & Ibnsouda, S. K. (2016). Methods for in vitro evaluating antimicrobial activity: A review. Journal of Pharmaceutical Analysis, 6(2), 71–79. https://doi.org/10.1016/j.jpha.2015.11.005

Barak, A., Eyal, O., Rosner, M., Belotserkousky, E., Solomon, A., Belkin, M., & Katzir, A. (1997). Temperature-controlled CO2 laser tissue welding of ocular tissues. Survey of Ophthalmology, 42, S77–S81. https://doi.org/10.1016/S0039-6257(97)80029-X

Barton, M., Morley, J. W., Stoodley, M. A., Ng, K.-S., Piller, S. C., Duong, H., … Lauto, A. (2013). Laser-activated adhesive films for sutureless median nerve anastomosis: Laser-activated adhesive films. Journal of Biophotonics, 6(11–12), 938–949. https://doi.org/10.1002/jbio.201300054

Bashir, M. R., Bhatti, L., Marin, D., & Nelson, R. C. (2015). Emerging Applications for Ferumoxytol as a Contrast Agent in MRI. Journal of Magnetic Resonance Imaging, 41(4), 884–898. https://doi.org/10.1002/jmri.24691

Bass, L., Moazami, N., Pocsidio, J., Oz, M., Logerfo, P., & Treat, M. (1992). Changes in Type-I Collagen Following Laser-Welding. Lasers in Surgery and Medicine, 12(5), 500–505. https://doi.org/10.1002/lsm.1900120508

Bass, L. S., & Treat, M. R. (1995). Laser tissue welding: A comprehensive review of current and future clinical applications. Lasers in Surgery and Medicine, 17(4), 315–349. https://doi.org/10.1002/lsm.1900170402

Bass, Lawrence S., Moazami, N., Pocsidio, J., Oz, M. C., Logerfo, P., & Treat, M. R. (1992). Changes in type I collagen following laser welding. Lasers in Surgery and Medicine, 12(5), 500–505. https://doi.org/10.1002/lsm.1900120508

Berríos-Torres, S. I., Umscheid, C. A., Bratzler, D. W., Leas, B., Stone, E. C., Kelz, R. R., … Mazuski, J. E. (2017). Centers for Disease Control and Prevention guideline for the prevention of surgical site infection, 2017. JAMA Surgery, 152(8), 784–791.

Bhowmick, P., Coad, J. E., Bhowmick, S., Pryor, J. L., Larson, T., De la Rosette, J., & Bischof, J. C. (2004). In vitro assessment of the efficacy of thermal therapy in human benign prostatic hyperplasia. International Journal of Hyperthermia, 20(4), 421–439. https://doi.org/10.1080/02656730310001637343

Bilici, T. (2010a). Modulated and continuous-wave operations of low-power thulium (Tm:YAP) laser in tissue welding. Journal of Biomedical Optics, 15(3), 038001. https://doi.org/10.1117/1.3431108

Bilici, T. (2010b). Modulated and continuous-wave operations of low-power thulium (Tm:YAP) laser in tissue welding. Journal of Biomedical Optics, 15(3), 038001. https://doi.org/10.1117/1.3431108

Bleier, B., Palmer, J., Sparano, A., & Cohen, N. (2007). Laser-assisted cerebrospinal fluid leak repair: An animal model to test feasibility. Otolaryngology - Head and Neck Surgery, 137(5), 810–814. https://doi.org/10.1016/j.otohns.2007.05.060

Bleier, B. S. (2010a). Laser Tissue Welding in Lung and Tracheobronchial Repair: An Animal Model. CHEST Journal, 138(2), 345. https://doi.org/10.1378/chest.09-2721

Bleier, B. S., Cohen, N. M., Bloom, J. D., Palmer, J. N., & Cohen, N. A. (2010). Laser Tissue Welding in Lung and Tracheobronchial Repair An Animal Model. Chest, 138(2), 345–349. https://doi.org/10.1378/chest.09-2721

Bleier, B. S., Palmer, J. N., Sparano, A. M., & Cohen, N. A. (2007a). Laser-assisted cerebrospinal fluid leak repair: An animal model to test feasibility. Otolaryngology-Head and Neck Surgery, 137(5), 810–814. https://doi.org/10.1016/j.otohns.2007.05.060

Bleustein, C. B., Walker, C. N., Felsen, D., & Poppas, D. P. (2000). Semi-solid albumin solder improved mechanical properties for laser tissue welding. Lasers in Surgery and Medicine, 27(2), 140–146. https://doi.org/10.1002/1096-9101(2000)27:2<140::AID-LSM5>3.0.CO;2-C

Bouten, P. J. M., Zonjee, M., Bender, J., Yauw, S. T. K., van Goor, H., van Hest, J. C. M., & Hoogenboom, R. (2014). The chemistry of tissue adhesive materials. Progress in Polymer Science, 39(7), 1375–1405. https://doi.org/10.1016/j.progpolymsci.2014.02.001

Braghirolli, D. I., Steffens, D., & Pranke, P. (2014). Electrospinning for regenerative medicine: A review of the main topics. Drug Discovery Today, 19(6), 743–753. https://doi.org/10.1016/j.drudis.2014.03.024

Brown, R. A., Wiseman, M., Chuo, C.-B., Cheema, U., & Nazhat, S. N. (2005). Ultrarapid Engineering of Biomimetic Materials and Tissues: Fabrication of Nano- and Microstructures by Plastic Compression. Advanced Functional Materials, 15(11), 1762–1770. https://doi.org/10.1002/adfm.200500042

Brust, M., Fink, J., Bethell, D., Schiffrin, D. J., & Kiely, C. (1995). Synthesis and reactions of functionalised gold nanoparticles. Journal of the Chemical Society, Chemical Communications, 0(16), 1655–1656. https://doi.org/10.1039/C39950001655

Busby, G. A., Grant, M. H., MacKay, S. P., & Riches, P. E. (2013). Confined compression of collagen hydrogels. Journal of Biomechanics, 46(4), 837–840. https://doi.org/10.1016/j.jbiomech.2012.11.048

Butcher, A. L., Offeddu, G. S., & Oyen, M. L. (2014). Nanofibrous hydrogel composites as mechanically robust tissue engineering scaffolds. Trends in Biotechnology, 32(11), 564–570. https://doi.org/10.1016/j.tibtech.2014.09.001

Capon, A., Souil, E., Gauthier, B., Sumian, C., Bachelet, M., Buys, B., … Mordon, S. (2001). Laser assisted skin closure (LASC) by using a 815-nm diode-laser system accelerates and improves wound healing. Lasers in Surgery and Medicine, 28(2), 168–175.

Cezo, J. D., Passernig, A. C., Ferguson, V. L., Taylor, K. D., & Rentschler, M. E. (2014a). Evaluating temperature and duration in arterial tissue fusion to maximize bond strength. Journal of the Mechanical Behavior of Biomedical Materials, 30, 41–49. https://doi.org/10.1016/j.jmbbm.2013.10.007

Cezo, J., Kramer, E., Taylor, K., Ferguson, V., & Rentschler, M. (2013, February). Tissue fusion bursting pressure and the role of tissue water content (T. P. Ryan, Ed.). https://doi.org/10.1117/12.2002184

Chelala, E., Thoma, M., Tatete, B., Lemye, A. C., Dessily, M., & Alle, J. L. (2007). The suturing concept for laparoscopic mesh fixation in ventral and incisional hernia repair:

Mid-term analysis of 400 cases. Surgical Endoscopy, 21(3), 391–395. https://doi.org/10.1007/s00464-006-9014-x

Chhabra, H., Deshpande, R., Kanitkar, M., Jaiswal, A., Kale, V. P., & Bellare, J. R. (2016). A nano zinc oxide doped electrospun scaffold improves wound healing in a rodent model. Rsc Advances, 6(2), 1428–1439. https://doi.org/10.1039/c5ra21821g

Chivers, R. A. (2000). In vitro tissue welding using albumin solder: Bond strengths and bonding temperatures. International Journal of Adhesion and Adhesives, 20(3), 179–187.

Cilesiz, I. (1999). Controlled Temperature Photothermal Tissue Welding. Journal of Biomedical Optics, 4(3), 327–336.

Cimador, M., Castagnetti, M., & Milazzo, M. (2004). Suture materials: Do they affect fistula and stricture rates in flap urethroplasties? Urologia ….

Cirocchi, R., Randolph, J. J., Montedori, A., Cochetti, G. G., Arezzo, A., Mearini, E. E., … Trastulli, S. (2014). Staples versus sutures for surgical wound closure in adults. Cochrane Database of Systematic Reviews. https://doi.org/10.1002/14651858.CD011250

Constantinescu, M. A., Alfieri, A., Mihalache, G., Stuker, F., Ducray, A., Seiler, R. W., … Reinert, M. (2007a). Effect of laser soldering irradiation on covalent bonds of pure collagen. Lasers in Medical Science, 22(1), 10–14. https://doi.org/10.1007/s10103-006-0411-0

Coolman, B. R., Ehrhart, N., Pijanowski, G., Ehrhart, E. J., & Coolman, S. L. (2000). Comparison of skin staples with sutures for anastomosis of the small intestine in dogs. Veterinary Surgery, 29(4), 293–302. https://doi.org/10.1053/jvet.2000.7539

Coulthard, P., Esposito, M., Worthington, H. V., van der Elst, M., van Waes, O. J. F., & Darcey, J. (2010). Tissue adhesives for closure of surgical incisions. In The Cochrane Collaboration (Ed.), Cochrane Database of Systematic Reviews. https://doi.org/10.1002/14651858.CD004287.pub3

Daniel, M., & Astruc, D. (2004). Gold nanoparticles: Assembly, supramolecular chemistry, quantum-size-related properties, and applications toward biology, catalysis, and nanotechnology. Chemical Reviews.

Daniel, M. C., & Astruc, D. (2004). Gold nanoparticles: Assembly, supramolecular chemistry, quantum-size-related properties, and applications toward biology, catalysis, and nanotechnology. Chemical Reviews, 104(1), 293–346. https://doi.org/10.1021/cr030698+

D'Arcangelo, C., Di Nardo Di Maio, F., Prosperi, G. D., Conte, E., Baldi, M., & Caputi, S. (2007). A preliminary study of healing of diode laser versus scalpel incisions in rat oral tissue: A comparison of clinical, histological, and immunohistochemical results. Oral

Surgery, Oral Medicine, Oral Pathology, Oral Radiology and Endodontology, 103(6), 764–773. https://doi.org/10.1016/j.tripleo.2006.08.002

Dennis, C., Sethu, S., Nayak, S., Mohan, L., Morsi, Y., & Manivasagam, G. (2016). Suture materials—Current and emerging trends. Journal of Biomedical Materials Research Part A, 104(6), 1544–1559. https://doi.org/10.1002/jbm.a.35683

Dewhirst, M. W., Viglianti, B. L., Lora-Michiels, M., Hanson, M., & Hoopes, P. J. (2003). Basic principles of thermal dosimetry and thermal thresholds for tissue damage from hyperthermia. International Journal of Hyperthermia, 19(3), 267–294. https://doi.org/10.1080/0265673031000119006

Dewi, A. H., Ana, I. D., Wolke, J., & Jansen, J. (2015). Behavior of POP-calcium carbonate hydrogel as bone substitute with controlled release capability: A study in rat. Journal of Biomedical Materials Research Part A, 103(10), 3273–3283. https://doi.org/10.1002/jbm.a.35460

Diab, T., Pritchard, E. M., Uhrig, B. A., Boerckel, J. D., Kaplan, D. L., & Guldberg, R. E. (2012). A silk hydrogel-based delivery system of bone morphogenic protein for the treatment of large bone defects. Journal of the Mechanical Behavior of Biomedical Materials, 11, 123–131. https://doi.org/10.1016/j.jmbbm.2011.11.007

Diller, K. R., Valvano, J. W., & Pearce, J. A. (2000). Bioheat transfer. CRC Handbook of Thermal Engineering, 4, 114–215.

Dong, R. H., Qin, C. C., Qiu, X., Yan, X., Yu, M., Cui, L., … Long, Y. Z. (2015). In situ precision electrospinning as an effective delivery technique for cyanoacrylate medical glue with high efficiency and low toxicity. Nanoscale, 7(46), 19468–19475.

Duarte, A. P., Coelho, J. F., Bordado, J. C., Cidade, M. T., & Gil, M. H. (2012a). Surgical adhesives: Systematic review of the main types and development forecast. Progress in Polymer Science, 37(8), 1031–1050. https://doi.org/10.1016/j.progpolymsci.2011.12.003

Duran, N., Marcato, P. D., De Conti, R., Alves, O. L., Costa, F. T. M., & Brocchi, M. (2010). Potential Use of Silver Nanoparticles on Pathogenic Bacteria, their Toxicity and Possible Mechanisms of Action. Journal of the Brazilian Chemical Society, 21(6), 949–959. https://doi.org/10.1590/S0103-50532010000600002

Edlich, R. F., Rodeheaver, G. T., Thacker, J. G., Lin, K. Y., Drake, D. B., Mason, S. S., … Long III, W. B. (2010). Revolutionary advances in the management of traumatic wounds in the emergency department during the last 40 years: Part I. The Journal of Emergency Medicine, 38(1), 40–50.

Edmiston Jr, C. E., Daoud, F. C., & Leaper, D. (2013). Is there an evidence-based argument for embracing an antimicrobial (triclosan)-coated suture technology to reduce the risk for surgical-site infections?: A meta-analysis. Surgery, 154(1), 89–100.

Eetezadi, S., Ekdawi, S. N., & Allen, C. (2015). The challenges facing block copolymer micelles for cancer therapy: In vivo barriers and clinical translation. Advanced Drug Delivery Reviews, 91, 7–22. https://doi.org/10.1016/j.addr.2014.10.001

Elsolh, B., Zhang, L., & Patel, S. V. (2017). The effect of antibiotic-coated sutures on the incidence of surgical site infections in abdominal closures: A meta-analysis. Journal of Gastrointestinal Surgery, 21(5), 896–903.

Enoch, S., Grey, J. E., & Harding, K. G. (2006). ABC of wound healing—Recent advances and emerging treatments. Bmj-British Medical Journal, 332(7547), 962–965. https://doi.org/10.1136/bmj.332.7547.962

Esposito, G., Rossi, F., Matteini, P., Scerrati, A., Puca, A., Albanese, A., … Pini, R. (2013a). In vivo laser assisted microvascular repair and end-to-end anastomosis by means of indocyanine green-infused chitosan patches: A pilot study. Lasers in Surgery and Medicine, 45(5), 318–325. https://doi.org/10.1002/lsm.22145

Falk-Brynhildsen, K., Söderquist, B., Friberg, Ö., & Nilsson, U. (2014). Bacterial growth and wound infection following saphenous vein harvesting in cardiac surgery: A randomized controlled trial of the impact of microbial skin sealant. European Journal of Clinical Microbiology & Infectious Diseases, 33(11), 1981–1987.

Fang, M., Yuan, J., Peng, C., & Li, Y. (2014). Collagen as a double-edged sword in tumor progression. Tumor Biology, 35(4), 2871–2882. https://doi.org/10.1007/s13277-013-1511-7

Farrell, D., Ptak, K., Panaro, N. J., & Grodzinski, P. (2011). Nanotechnology-Based Cancer Therapeutics-Promise and Challenge-Lessons Learned Through the NCI Alliance for Nanotechnology in Cancer. Pharmaceutical Research, 28(2), 273–278. https://doi.org/10.1007/s11095-010-0214-7

Fleischer, S., & Dvir, T. (2013). Tissue engineering on the nanoscale: Lessons from the heart. Current Opinion in Biotechnology, 24(4), 664–671. https://doi.org/10.1016/j.copbio.2012.10.016

Foyt, D., Johnson, J. P., Kirsch, A. J., Bruce, J. N., & Wazen, J. J. (1996). Dural closure with laser tissue welding. Otolaryngology-Head and Neck Surgery, 115(6), 513–518. https://doi.org/10.1016/S0194-5998(96)70005-0

Frykberg, R. G., & Banks, J. (2015). Challenges in the treatment of chronic wounds. Advances in Wound Care, 4(9), 560–582.

Fuentes, D., Oden, J. T., Diller, K. R., Hazle, J. D., Elliott, A., Shetty, A., & Stafford, R. J. (2009). Computational Modeling and Real-Time Control of Patient-Specific Laser

Treatment of Cancer. Annals of Biomedical Engineering, 37(4), 763–782. https://doi.org/10.1007/s10439-008-9631-8

Garcia, P., Mines, M. J., Bower, K. S., Hill, J., Menon, J., Tremblay, E., & Smith, B. (2009a). Robotic laser tissue welding of sclera using chitosan films. Lasers in Surgery and Medicine, 41(1), 59–67. https://doi.org/10.1002/lsm.20727

Gayen, T., & Katz, A. (2003). Near-infrared laser welding of aortic and skin tissues and microscopic investigation of welding efficacy. Biomedical ….

Ghadiri, M., Chrzanowski, W., & Rohanizadeh, R. (2015). Biomedical applications of cationic clay minerals. Rsc Advances, 5(37), 29467–29481. https://doi.org/10.1039/c4ra16945j

Gobin, A. M., O'Neal, D. P., Watkins, D. M., Halas, N. J., Drezek, R. A., & West, J. L. (2005a). Near infrared laser-tissue welding using nanoshells as an exogenous absorber. Lasers in Surgery and Medicine, 37(2), 123–129. https://doi.org/10.1002/lsm.20206

Gobin, A. M., O'neal, D. P., Watkins, D. M., Halas, N. J., Drezek, R. A., & West, J. L. (2005). Near infrared laser-tissue welding using nanoshells as an exogenous absorber. Lasers in Surgery and Medicine: The Official Journal of the American Society for Laser Medicine and Surgery, 37(2), 123–129.

Guo, C., N. Hall, G., B. Addison, J., & L. Yarger, J. (2015). Gold nanoparticle-doped silk film as biocompatible SERS substrate. RSC Advances, 5(3), 1937–1942. https://doi.org/10.1039/C4RA11051J

Guo, D., Xie, G., & Luo, J. (2014). Mechanical properties of nanoparticles: Basics and applications. Journal of Physics D-Applied Physics, 47(1), 013001. https://doi.org/10.1088/0022-3727/47/1/013001

Gurtner, G. C., Werner, S., Barrandon, Y., & Longaker, M. T. (2008). Wound repair and regeneration. Nature, 453(7193), 314–321. https://doi.org/10.1038/nature07039

Gurusamy, K. S., Toon, C. D., Allen, V. B., & Davidson, B. R. (2014). Continuous versus interrupted skin sutures for non-obstetric surgery. Cochrane Database of Systematic Reviews, (2).

Hajipour, M. J., Fromm, K. M., Ashkarran, A. A., Jimenez de Aberasturi, D., Ruiz de Larramendi, I., Rojo, T., … Mahmoudi, M. (2012). Antibacterial properties of nanoparticles. Trends in Biotechnology, 30(10), 499–511. https://doi.org/10.1016/j.tibtech.2012.06.004

Hall, W. A. (2015). Vancomycin powder in spine surgery: Still a work in progress. World Neurosurgery, 6(83), 1051–1052.

Hayman, M. L. (2009). The emerging product and patent landscape for nanosilver-containing medical devices. Nanotech. L. & Bus., (6), 148.

He, W., Frueh, J., Hu, N., Liu, L., Gai, M., & He, Q. (2016). Guidable Thermophoretic Janus Micromotors Containing Gold Nanocolorifiers for Infrared Laser Assisted Tissue Welding. Advanced Science, 3(12), 1600206. https://doi.org/10.1002/advs.201600206

He, W., Frueh, J., Shao, J., Gai, M., Hu, N., & He, Q. (2016). Guidable GNR-Fe3O4-PEM@SiO2 composite particles containing near infrared active nanocalorifiers for laser assisted tissue welding. Colloids and Surfaces A-Physicochemical and Engineering Aspects, 511, 73–81. https://doi.org/10.1016/j.colsurfa.2016.09.052

Henriques, F. (1947). Studies of Thermal Injury .5. The Predictability and the Significance of Thermally Induced Rate Processes Leading to Irreversible Epidermal Injury. Archives of Pathology, 43(5), 489–502.

Hida, K., Yamaguchi, S., Seki, T., Yano, S., Akino, M., Terasaka, S., … Iwasaki, Y. (2006). Nonsuture dural repair using polyglycolic acid mesh and fibrin glue: Clinical application to spinal surgery. Surgical Neurology, 65(2), 136–142. https://doi.org/10.1016/j.surneu.2005.07.059

Hirsch, L. R., Gobin, A. M., Lowery, A. R., Tam, F., Drezek, R. A., Halas, N. J., & West, J. L. (2006). Metal Nanoshells. Annals of Biomedical Engineering, 34(1), 15–22. https://doi.org/10.1007/s10439-005-9001-8

Hoffman, G. T., Byrd, B. D., Soller, E. C., Heintzelman, D. L., & McNally-Heintzelman, K. M. (2003a). Alternative chromophores for use in light-activated surgical adhesives: Optimization of parameters for tensile strength and thermal damage profile. 174–181. International Society for Optics and Photonics.

Hopley, E. L., Salmasi, S., Kalaskar, D. M., & Seifalian, A. M. (2014). Carbon nanotubes leading the way forward in new generation 3D tissue engineering. Biotechnology Advances, 32(5), 1000–1014. https://doi.org/10.1016/j.biotechadv.2014.05.003

Horan, R., Toponarski, I., Boepple, H., Weitzel, P., Richmond, J., & Altman, G. (2009). Design and Characterization of a Scaffold for Anterior Cruciate Ligament Engineering. Journal of Knee Surgery, 22(01), 82–92. https://doi.org/10.1055/s-0030-1247730

Hu, D., Zhang, J., Gao, G., Sheng, Z., Cui, H., & Cai, L. (2016). Indocyanine Green-Loaded Polydopamine-Reduced Graphene Oxide Nanocomposites with Amplifying Photoacoustic and Photothermal Effects for Cancer Theranostics. Theranostics, 6(7), 1043–1052. https://doi.org/10.7150/thno.14566

Hu, L., Lu, Z., Wang, B., Cao, J., Ma, X., Tian, Z., … others. (2011). Closure of skin incisions by laser-welding with a combination of two near-infrared diode lasers:

Preliminary study for determination of optimal parameters. Journal of Biomedical Optics, 16(3), 038001–038001.

Hu, M. S., Maan, Z. N., Wu, J.-C., Rennert, R. C., Hong, W. X., Lai, T. S., … Lorenz, H. P. (2014). Tissue Engineering and Regenerative Repair in Wound Healing. Annals of Biomedical Engineering, 42(7), 1494–1507. https://doi.org/10.1007/s10439-014-1010-z

Hu, X., Kaplan, D., & Cebe, P. (2006). Determining Beta-Sheet Crystallinity in Fibrous Proteins by Thermal Analysis and Infrared Spectroscopy. Macromolecules, 39(18), 6161–6170. https://doi.org/10.1021/ma0610109

Huang, H.-C., Koria, P., Parker, S. M., Selby, L., Megeed, Z., & Rege, K. (2008). Optically Responsive Gold Nanorod-Polypeptide Assemblies. Langmuir, 24(24), 14139–14144. https://doi.org/10.1021/la802842k

Huang, H.-C., Nanda, A., & Rege, K. (2012a). Investigation of Phase Separation Behavior and Formation of Plasmonic Nanocomposites from Polypeptide-Gold Nanorod Nanoassemblies. Langmuir, 28(16), 6645–6655. https://doi.org/10.1021/la203340y

Huang, H.-C., Rege, K., & Heys, J. J. (2010a). Spatiotemporal Temperature Distribution and Cancer Cell Death in Response to Extracellular Hyperthermia Induced by Gold Nanorods. ACS Nano, 4(5), 2892–2900. https://doi.org/10.1021/nn901884d

Huang, H.-C., Walker, C. R., Nanda, A., & Rege, K. (2013a). Laser Welding of Ruptured Intestinal Tissue Using Plasmonic Polypeptide Nanocomposite Solders. ACS Nano, 7(4), 2988–2998. https://doi.org/10.1021/nn303202k

Huang, X., Jain, P. K., El-Sayed, I. H., & El-Sayed, M. A. (2008). Plasmonic photothermal therapy (PPTT) using gold nanoparticles. Lasers in Medical Science, 23(3), 217–228. https://doi.org/10.1007/s10103-007-0470-x

Huh, J. W., Kim, H. R., & Kim, Y. J. (2010). Anastomotic leakage after laparoscopic resection of rectal cancer: The impact of fibrin glue. The American Journal of Surgery, 199(4), 435–441. https://doi.org/10.1016/j.amjsurg.2009.01.018

Hyman, N., Manchester, T. L., Osler, T., Burns, B., & Cataldo, P. A. (2007). Anastomotic leaks after intestinal anastomosis—It's later than you think. Annals of Surgery, 245(2), 254–258. https://doi.org/10.1097/01.sla.0000225083.27182.85

Ikossi-O'Connor, M. G., Ambrus, J. L., & Rao, U. (1983). The role of fibrin adhesive in vascular surgery. Journal of Surgical Oncology, 23(3), 151–152.

Islam, M. S., Ahmed, M. F., & Rahman, S. R. (2013). Incidence of Methicillin Resistant Staphylococcus aureus in Burn Patients Admitted to Burn Unit, Dhaka Medical College Hospital, Bangladesh. https://doi.org/10.4236/aim.2013.36066

Jacques, SL, & Prahl, S. (1987). Modeling optical and thermal distributions in tissue during laser irradiation. Lasers in Surgery and Medicine.

Jacques, Sl, & Prahl, S. (1987). Modeling Optical and Thermal Distributions in Tissue During Laser Irradiation. Lasers in Surgery and Medicine, 6(6), 494–503. https://doi.org/10.1002/lsm.1900060604

Jain, K., & Gorisch, W. (1979). Repair of small blood vessels with the Neodymium-YAG laser: A preliminary report. Surgery.

Jaiswal, M., Koul, V., & Dinda, A. K. (2016). In vitro and in vivo investigational studies of a nanocomposite-hydrogel-based dressing with a silver-coated chitosan wafer for full-thickness skin wounds. Journal of Applied Polymer Science, 133(21), 43472. https://doi.org/10.1002/app.43472

Jauffred, L., Taheri, S. M.-R., Schmitt, R., Linke, H., & Oddershede, L. B. (2015). Optical Trapping of Gold Nanoparticles in Air. Nano Letters, 15(7), 4713–4719. https://doi.org/10.1021/acs.nanolett.5b01562

Jeon, E. Y., Hwang, B. H., Yang, Y. J., Kim, B. J., Choi, B.-H., Jung, G. Y., & Cha, H. J. (2015). Rapidly light-activated surgical protein glue inspired by mussel adhesion and insect structural crosslinking. Biomaterials, 67, 11–19.

Jin, R., Cao, Y., Mirkin, C. A., Kelly, K. L., Schatz, G. C., & Zheng, J. G. (2001). Photoinduced conversion of silver nanospheres to nanoprisms. Science, 294(5548), 1901–1903.

Kang, Y. O., Jung, J.-Y., Cho, D., Kwon, O. H., Cheon, J. Y., & Park, W. H. (2016). Antimicrobial Silver Chloride Nanoparticles Stabilized with Chitosan Oligomer for the Healing of Burns. Materials, 9(4), 215. https://doi.org/10.3390/ma9040215

Karamzadeh, A. M., Wong, B. J. F., Crumley, R. L., & Ahuja, G. (2004). Lasers in pediatric airway surgery: Current and future clinical applications. Lasers in Surgery and Medicine, 35(2), 128–134. https://doi.org/10.1002/lsm.20058

Kharlamov, A. N., & Gabinsky, J. L. (2012). Plasmonic Photothermic and Stem Cell Therapy of Atherosclerotic Plaque As a Novel Nanotool for Angioplasty and Artery Remodeling. Rejuvenation Research, 15(2), 222–230. https://doi.org/10.1089/rej.2011.1305

Kim, B. M., Jacques, S. L., Rastegar, S., Thomsen, S., & Motamedi, M. (1996). Nonlinear finite-element analysis of the role of dynamic changes in blood perfusion and optical properties in laser coagulation of tissue. Ieee Journal of Selected Topics in Quantum Electronics, 2(4), 922–933. https://doi.org/10.1109/2944.577317

Kim, T., & Hyeon, T. (2014). Applications of inorganic nanoparticles as therapeutic agents. Nanotechnology, 25(1), 012001. https://doi.org/10.1088/0957-4484/25/1/012001

Kirsch, A., Duckett, J., & Snyder, H. (1997). Skin flap closure by dermal laser soldering: A wound healing model for sutureless hypospadias repair. Urology.

Kirsch, A. J., Miller, M. I., Hensle, T. W., Chang, D. T., Shabsigh, R., Olsson, C. A., & Connor, J. P. (1995). Laser tissue soldering in urinary tract reconstruction: First human experience. Urology, 46(2), 261–266. https://doi.org/10.1016/S0090-4295(99)80206-4

Kojima, R., Aubel, D., & Fussenegger, M. (2015). Novel theranostic agents for next-generation personalized medicine: Small molecules, nanoparticles, and engineered mammalian cells. Current Opinion in Chemical Biology, 28, 29–38. https://doi.org/10.1016/j.cbpa.2015.05.021

Komatsu, F., Mori, R., & Uchio, Y. (2006). Optimum surgical suture material and methods to obtain high tensile strength at knots: Problems of conventional knots and the reinforcement effect of adhesive agent. Journal of Orthopaedic Science, 11(1), 70–74. https://doi.org/10.1007/s00776-005-0973-x

Koski, K. J., Akhenblit, P., McKiernan, K., & Yarger, J. L. (2013). Non-invasive determination of the complete elastic moduli of spider silks. Nature Materials, 12(3), 262–267. https://doi.org/10.1038/NMAT3549

Koutsopoulos, S. (2012). Molecular fabrications of smart nanobiomaterials and applications in personalized medicine. Advanced Drug Delivery Reviews, 64(13), 1459–1476. https://doi.org/10.1016/j.addr.2012.08.002

Krishnan, R., MacNeil, S. D., & Malvankar-Mehta, M. S. (2016). Comparing sutures versus staples for skin closure after orthopaedic surgery: Systematic review and meta-analysis. Bmj Open, 6(1), e009257. https://doi.org/10.1136/bmjopen-2015-009257

Lauto, A., Mawad, D., Barton, M., Gupta, A., Piller, S. C., & Hook, J. (2010). Photochemical tissue bonding with chitosan adhesive films. Biomed Eng Online, 9, 47.

Lauto, A., Mawad, D., & Foster, L. J. R. (2008a). Adhesive biomaterials for tissue reconstruction. Journal of Chemical Technology & Biotechnology, 83(4), 464–472. https://doi.org/10.1002/jctb.1771

Lemans, J. V., Wijdicks, S. P., Boot, W., Govaert, G. A., Houwert, R. M., Öner, F. C., & Kruyt, M. C. (2019). Intrawound treatment for prevention of surgical site infections in instrumented spinal surgery: A systematic comparative effectiveness review and meta-analysis. Global Spine Journal, 9(2), 219–230.

Lepock, J. R. (2003). Cellular effects of hyperthermia: Relevance to the minimum dose for thermal damage. International Journal of Hyperthermia, 19(3), 252–266. https://doi.org/10.1080/0265673031000065042

Levi-Polyachenko, N., Jacob, R., Day, C., & Kuthirummal, N. (2016). Chitosan wound dressing with hexagonal silver nanoparticles for hyperthermia and enhanced delivery of small molecules. Colloids and Surfaces B-Biointerfaces, 142, 315–324. https://doi.org/10.1016/j.colsurfb.2016.02.038

Levis, H. J., Menzel-Severing, J., Drake, R. A. L., & Daniels, J. T. (2013). Plastic Compressed Collagen Constructs for Ocular Cell Culture and Transplantation: A New and Improved Technique of Confined Fluid Loss. Current Eye Research, 38(1), 41–52. https://doi.org/10.3109/02713683.2012.725799

Lewinski, N., Colvin, V., & Drezek, R. (2008). Cytotoxicity of nanoparticles. Small, 4(1), 26–49. https://doi.org/10.1002/smll.200700595

Li, C., Protsenko, D. E., Zemek, A., Chae, Y.-S., & Wong, B. (2007). Analysis of Nd:YAG laser-mediated thermal damage in rabbit nasal septal cartilage. Lasers in Surgery and Medicine, 39(5), 451–457. https://doi.org/10.1002/lsm.20514

Liang, D., Lu, Z., Yang, H., Gao, J., & Chen, R. (2016). Novel Asymmetric Wettable AgNPs/Chitosan Wound Dressing: In Vitro and In Vivo Evaluation. Acs Applied Materials & Interfaces, 8(6), 3958–3968. https://doi.org/10.1021/acsami.5b11160

Libutti, S., Oz, M., Forde, K., & Auteri, J. (1990). Canine colonic anastomoses reinforced with dye-enhanced fibrinogen and a diode laser. Surgical ….

Liu, K.-C., & Wang, J.-C. (2014). Analysis of thermal damage to laser irradiated tissue based on the dual-phase-lag model. International Journal of Heat and Mass Transfer, 70, 621–628. https://doi.org/10.1016/j.ijheatmasstransfer.2013.11.044

Liu, R., Liu, H. H., Ji, Z., Chang, C. H., Xia, T., Nel, A. E., & Cohen, Y. (2015). Evaluation of Toxicity Ranking for Metal Oxide Nanoparticles via an in Vitro Dosimetry Model. Acs Nano, 9(9), 9303–9313. https://doi.org/10.1021/acsnano.5b04420

Liu, Y., Meng, H., Konst, S., Sarmiento, R., Rajachar, R., & Lee, B. P. (2014). Injectable Dopamine-Modified Poly(ethylene glycol) Nanocomposite Hydrogel with Enhanced Adhesive Property and Bioactivity. Acs Applied Materials & Interfaces, 6(19), 16982–16992. https://doi.org/10.1021/am504566v

Lloyd, J., Marque, M. 3rd, & Kacprowicz, R. (2007). Closure Techniques. Emerg. Med. Clin. N. Am., (25), 73–81.

Lobik, L., Ravid, A., & NISSENKORN, I. (1999). Bladder welding in rats using controlled temperature CO_2 laser system. The Journal of ….

Lu, Q., Hu, X., Wang, X., Kluge, J. A., Lu, S., Cebe, P., & Kaplan, D. L. (2010). Water-insoluble silk films with silk I structure. Acta Biomaterialia, 6(4), 1380–1387. https://doi.org/10.1016/j.actbio.2009.10.041

Lumsden, A. B., & Heyman, E. R. (2006). Prospective randomized study evaluating an absorbable cyanoacrylate for use in vascular reconstructions. Journal of Vascular Surgery, 44(5), 1002-1009.e1. https://doi.org/10.1016/j.jvs.2006.06.039

Mackey, M. A., Ali, M. R. K., Austin, L. A., Near, R. D., & El-Sayed, M. A. (2014). The Most Effective Gold Nanorod Size for Plasmonic Photothermal Therapy: Theory and In Vitro Experiments. The Journal of Physical Chemistry B, 118(5), 1319–1326. https://doi.org/10.1021/jp409298f

Mandal, A., Sekar, S., Chandrasekaran, N., Mukherjee, A., & Sastry, T. P. (2015). Synthesis, characterization and evaluation of collagen scaffolds crosslinked with aminosilane functionalized silver nanoparticles: In vitro and in vivo studies. Journal of Materials Chemistry B, 3(15), 3032–3043. https://doi.org/10.1039/c4tb02124j

Martin, E. T., Kaye, K. S., Knott, C., Nguyen, H., Santarossa, M., Evans, R., … Jaber, L. (2016). Diabetes and risk of surgical site infection: A systematic review and meta-analysis. Infection Control & Hospital Epidemiology, 37(1), 88–99.

Mattei, T. A., & Rehman, A. A. (2014). Technological Developments and Future Perspectives on Graphene-Based Metamaterials: A Primer for Neurosurgeons. Neurosurgery, 74(5), 499–516. https://doi.org/10.1227/NEU.0000000000000302

Matteini, P., Ratto, F., Rossi, F., & Pini, R. (2010, February). <title>Biofilms of chitosan-gold nanorods as a novel composite for the laser welding of biological tissue</title> (A. N. Cartwright & D. V. Nicolau, Eds.). https://doi.org/10.1117/12.840923

Matteini, P, Sbrana, F., Tiribilli, B., & Pini, R. (2009). Atomic force microscopy and transmission electron microscopy analyses of low-temperature laser welding of the cornea. Lasers in Medical Science.

Matteini, Paolo, Cicchi, R., Ratto, F., Kapsokalyvas, D., Rossi, F., de Angelis, M., … Pini, R. (2012a). Thermal Transitions of Fibrillar Collagen Unveiled by Second-Harmonic Generation Microscopy of Corneal Stroma. Biophysical Journal, 103(6), 1179–1187. https://doi.org/10.1016/j.bpj.2012.07.055

Matteini, Paolo, Ratto, F., Rossi, F., Centi, S., Dei, L., & Pini, R. (2010). Chitosan films doped with gold nanorods as laser-activatable hybrid bioadhesives. Advanced Materials, 22(38), 4313–4316.

Matteini, Paolo, Ratto, F., Rossi, F., Cicchi, R., Stringari, C., Kapsokalyvas, D., … Pini, R. (2009a). Photothermally-induced disordered patterns of corneal collagen revealed by SHG imaging. Optics Express, 17(6), 4868–4878.

Matteini, Paolo, Ratto, F., Rossi, F., & Pini, R. (2012a). Emerging concepts of laser-activated nanoparticles for tissue bonding. Journal of Biomedical Optics, 17(1), 0107011–0107019.

Matteini, Paolo, Ratto, F., Rossi, F., Rossi, G., Esposito, G., Puca, A., … Pini, R. (2010). In vivo carotid artery closure by laser activation of hyaluronan-embedded gold nanorods. Journal of Biomedical Optics, 15(4), 041508. https://doi.org/10.1117/1.3449574

Matteini, Paolo, Rossi, F., Menabuoni, L., & Pini, R. (2007a). Microscopic characterization of collagen modifications induced by low-temperature diode-laser welding of corneal tissue. Lasers in Surgery and Medicine, 39(7), 597–604. https://doi.org/10.1002/lsm.20532

Matteini, Paolo, Sbrana, F., Tiribilli, B., & Pini, R. (2009). Atomic force microscopy and transmission electron microscopy analyses of low-temperature laser welding of the cornea. Lasers in Medical Science, 24(4), 667–671. https://doi.org/10.1007/s10103-008-0617-4

Matusiewicz, H. (2014). Potential release of in vivo trace metals from metallic medical implants in the human body: From ions to nanoparticles - A systematic analytical review. Acta Biomaterialia, 10(6), 2379–2403. https://doi.org/10.1016/j.actbio.2014.02.027

Meddahi-Pelle, A., Legrand, A., Marcellan, A., Louedec, L., Letourneur, D., & Leibler, L. (2014). Organ Repair, Hemostasis, and In Vivo Bonding of Medical Devices by Aqueous Solutions of Nanoparticles. Angewandte Chemie-International Edition, 53(25), 6369–6373. https://doi.org/10.1002/anie.201401043

Menaa, F., Abdelghani, A., & Menaa, B. (2015). Graphene nanomaterials as biocompatible and conductive scaffolds for stem cells: Impact for tissue engineering and regenerative medicine. Journal of Tissue Engineering and Regenerative Medicine, 9(12), 1321–1338. https://doi.org/10.1002/term.1910

Mercer, C., Minich, P., & Pauli, B. (1987). Sutureless bowel anastomosis using Nd: YAG laser. Lasers in Surgery and Medicine.

Millesi, H. (1981). Peripheral nerve injuries. Nerve sutures and nerve grafting. Scandinavian Journal of Plastic and Reconstructive ….

Millstone, J. E., Hurst, S. J., Metraux, G. S., Cutler, J. I., & Mirkin, C. A. (2009). Colloidal gold and silver triangular nanoprisms. Small, 5(6), 646–664.

Misof, K., Rapp, G., & Fratzl, P. (1997). A new molecular model for collagen elasticity based on synchrotron X-ray scattering evidence. Biophysical Journal, 72(3), 1376.

Morigi, V., Tocchio, A., Bellavite Pellegrini, C., Sakamoto, J. H., Arnone, M., & Tasciotti, E. (2012). Nanotechnology in Medicine: From Inception to Market Domination. Journal of Drug Delivery, 2012, 1–7. https://doi.org/10.1155/2012/389485

Murray, K., & Ho, C. (2002). The influence of pulmonary staple line reinforcement on air leaks. CHEST ….

Murray, L. W., Su, L., Kopchok, G. E., & White, R. A. (1989a). Crosslinking of extracellular matrix proteins: A preliminary report on a possible mechanism of argon laser welding. Lasers in Surgery and Medicine, 9(5), 490–496. https://doi.org/10.1002/lsm.1900090512

Mushaben, M., Urie, R., Flake, T., Jaffe, M., Rege, K., & Heys, J. (2018). Spatiotemporal modeling of laser tissue soldering using photothermal nanocomposites. Lasers in Surgery and Medicine, 50(2), 143–152.

Near, R. D., Hayden, S. C., & El-Sayed, M. A. (2013). Thin to Thick, Short to Long: Spectral Properties of Gold Nanorods by Theoretical Modeling. The Journal of Physical Chemistry C, 117(36), 18653–18656. https://doi.org/10.1021/jp4078344

Ngeow, W. C. (2010). Scar less: A review of methods of scar reduction at sites of peripheral nerve repair. Oral Surgery, Oral Medicine, Oral Pathology, Oral Radiology, and Endodontology, 109(3), 357–366. https://doi.org/10.1016/j.tripleo.2009.06.030

Nikoobakht, Babak, & El-Sayed, M. A. (2003). Preparation and Growth Mechanism of Gold Nanorods (NRs) Using Seed-Mediated Growth Method. Chemistry of Materials, 15(10), 1957–1962. https://doi.org/10.1021/cm020732l

Norman, G., Rabi, Y., Assia, E., & Katzir, A. (2009). In vitro conjunctival incision repair by temperature-controlled laser soldering. Journal of Biomedical Optics, 14(6), 064016. https://doi.org/10.1117/1.3262610

Novoselov, K. S., Geim, A. K., Morozov, S. V., Jiang, D., Zhang, Y., Dubonos, S. V., … Firsov, A. A. (2004). Electric field effect in atomically thin carbon films. Science, 306(5696), 666–669. https://doi.org/10.1126/science.1102896

O'Neill, A. C., Randolph, M. A., Bujold, K. E., Kochevar, I. E., Redmond, R. W., & Winograd, J. M. (2009). Photochemical Sealing Improves Outcome Following Peripheral Neurorrhaphy. Journal of Surgical Research, 151(1), 33–39. https://doi.org/10.1016/j.jss.2008.01.025

O'neill, A. C., Winograd, J. M., Zeballos, J. L., Johnson, T. S., Randolph, M. A., Bujold, K. E., … Redmond, R. W. (2007). Microvascular anastomosis using a photochemical tissue bonding technique. Lasers in Surgery and Medicine: The Official Journal of the American Society for Laser Medicine and Surgery, 39(9), 716–722.

Organization, W. H. (2016). Global guidelines for the prevention of surgical site infection. World Health Organization.

Pabittei, Dara R., de Boon, W., Shafirstein, G., Simonet, M., Bas, A., Balm, R., & Legemate, D. A. (2013). Laser-assisted vessel welding: A review on the current status and future outlook.

Pabittei, Dara R, Heger, M., Beek, J. F., van Tuijl, S., Simonet, M., van der Wal, A. C., … Balm, R. (2011). Optimization of suture-free laser-assisted vessel repair by solder-doped electrospun poly(ε-caprolactone) scaffold. Annals of Biomedical Engineering, 39(1), 223–234. https://doi.org/10.1007/s10439-010-0157-5

Pabittei, Dara R., Heger, M., Simonet, M., van Tuijl, S., van der Wal, A. C., van Bavel, E., & others. (2013). In vitro laser-assisted vascular welding: Optimization of acute and post-hydration welding strength. Sci Technol Adv Mater.

Pabittei, Dara R., Heger, M., van Tuijl, S., Simonet, M., Balm, R., Legemate, D. A., & Bas, A. (2013). End-to-end scaffold-enhanced laser-assisted vascular anastomosis: Ex vivo proof-of-concept in porcine arteries.

Pabittei, Dara Rosmailina. (2013). Optimization of in vitro sutureless laser-assisted vascular anastomosis. Universiteit van Amsterdam [Host].

Panáček, A., Kvítek, L., Prucek, R., Kolář, M., Večeřová, R., Pizúrová, N., … Zbořil, R. (2006). Silver Colloid Nanoparticles: Synthesis, Characterization, and Their Antibacterial Activity. The Journal of Physical Chemistry B, 110(33), 16248–16253. https://doi.org/10.1021/jp063826h

Paquet-Mercier, F., Lefèvre, T., Auger, M., & Pézolet, M. (2012). Evidence by infrared spectroscopy of the presence of two types of β-sheets in major ampullate spider silk and silkworm silk. Soft Matter, 9(1), 208–215. https://doi.org/10.1039/C2SM26657A

Park, I. J. (2010a). Influence of Anastomotic Leakage on Oncological Outcome in Patients with Rectal Cancer. Journal of Gastrointestinal Surgery, 14(7), 1190–1196. https://doi.org/10.1007/s11605-009-1153-7

Pearce, J., & Thomsen, S. (1995). Rate process analysis of thermal damage. In Optical-thermal response of laser-irradiated tissue (pp. 561–606). Springer.

Pecha, R. E., Prindiville, T., Kotfila, R., Ruebner, B., Cheung, A. T., & Trudeau, W. (1998). Gastrointestinal hemorrhage consequent to foreign body reaction to silk sutures: Case series and review. Gastrointestinal Endoscopy, 48(3), 299–301.

Pennes, H. (1948). Analysis of Tissue and Arterial Blood Temperatures in the Resting Human Forearm. Journal of Applied Physiology, 1(2), 93–122.

Perrone, G. S., Leisk, G. G., Lo, T. J., Moreau, J. E., Haas, D. S., Papenburg, B. J., … Kaplan, D. L. (2014). The use of silk-based devices for fracture fixation. Nature Communications, 5(1). https://doi.org/10.1038/ncomms4385

Piaggesi, A., Goretti, C., Mazzurco, S., Tascini, C., Leonildi, A., Rizzo, L., … Del Prato, S. (2010). A randomized controlled trial to examine the efficacy and safety of a new super-oxidized solution for the management of wide postsurgical lesions of the diabetic foot. The International Journal of Lower Extremity Wounds, 9(1), 10–15.

Piper, K. F., Tomlinson, S. B., Santangelo, G., Van Galen, J., DeAndrea-Lazarus, I., Towner, J., … Vates, G. E. (2017). Risk factors for wound complications following spine surgery. Surgical Neurology International, 8.

Poppas, D. P., Stewart, R. B., Massicotte, J. M., Wolga, A. E., Kung, R. T. V., Retik, A. B., & Freeman, M. R. (1996). Temperature-controlled laser photocoagulation of soft tissue: In vivo evaluation using a tissue welding model. Lasers in Surgery and Medicine, 18(4), 335–344. https://doi.org/10.1002/(SICI)1096-9101(1996)18:4<335::AID-LSM2>3.0.CO;2-T

Prabhu, S., & Poulose, E. K. (2012). Silver nanoparticles: Mechanism of antimicrobial action, synthesis, medical applications, and toxicity effects. International Nano Letters, 2(1), 32. https://doi.org/10.1186/2228-5326-2-32

Qin, Z., & Bischof, J. C. (2012). Thermophysical and biological responses of gold nanoparticle laser heating. Chemical Society Reviews, 41(3), 1191–1217. https://doi.org/10.1039/c1cs15184c

Rabi, Y., & Katzir, A. (2010). Temporal heating profile influence on the immediate bond strength following laser tissue soldering. Lasers in Surgery and Medicine, 42(5), 425–432. https://doi.org/10.1002/lsm.20927

Rai, M. K., Deshmukh, S. D., Ingle, A. P., & Gade, A. K. (2012). Silver nanoparticles: The powerful nanoweapon against multidrug-resistant bacteria. Journal of Applied Microbiology, 112(5), 841–852.

Ratto, F., Matteini, P., Rossi, F., Menabuoni, L., Tiwari, N., Kulkarni, S. K., & Pini, R. (2009a). Photothermal effects in connective tissues mediated by laser-activated gold nanorods. Nanomedicine: Nanotechnology, Biology and Medicine, 5(2), 143–151. https://doi.org/10.1016/j.nano.2008.10.002

Ratto, F., Matteini, P., Rossi, F., Pini, R., Tiwari, N., Kulkarni, S. K., & Menabuoni, L. (2008, February). <title>Gold nanorods as exogenous chromophores in the welding of ocular tissues</title> (F. Manns, P. G. Söderberg, A. Ho, B. E. Stuck, & M. Belkin, Eds.). https://doi.org/10.1117/12.763114

151

Reinke, J. M., & Sorg, H. (2012). Wound Repair and Regeneration. European Surgical Research, 49(1), 35–43. https://doi.org/10.1159/000339613

Reller, L. B., Weinstein, M., Jorgensen, J. H., & Ferraro, M. J. (2009). Antimicrobial Susceptibility Testing: A Review of General Principles and Contemporary Practices. Clinical Infectious Diseases, 49(11), 1749–1755. https://doi.org/10.1086/647952

Rittie, L. (2016). Cellular mechanisms of skin repair in humans and other mammals. Journal of Cell Communication and Signaling, 10(2), 103–120. https://doi.org/10.1007/s12079-016-0330-1

Rockwood, D. N., Preda, R. C., Yücel, T., Wang, X., Lovett, M. L., & Kaplan, D. L. (2011). Materials fabrication from Bombyx mori silk fibroin. Nature Protocols, 6(10), 1612–1631. https://doi.org/10.1038/nprot.2011.379

Rose, S., Prevoteau, A., Elziere, P., Hourdet, D., Marcellan, A., & Leibler, L. (2014a). Nanoparticle solutions as adhesives for gels and biological tissues. Nature, 505(7483), 382-+. https://doi.org/10.1038/nature12806

Ross, A. M., Jiang, Z., Bastmeyer, M., & Lahann, J. (2012). Physical Aspects of Cell Culture Substrates: Topography, Roughness, and Elasticity. Small, 8(3), 336–355. https://doi.org/10.1002/smll.201100934

Rossi, F., Pini, R., Menabuoni, L., Mencucci, R., Menchini, U., Ambrosini, S., & Vannelli, G. (2005). Experimental study on the healing process following laser welding of the cornea. Journal of Biomedical Optics, 10(2), 024004. https://doi.org/10.1117/1.1900703

Rossi, Francesca, Matteini, P., Ratto, F., Pini, R., Esposito, G., Albanese, A., … Rossi, G. (2011). Experimental study on laser assisted vascular repair and anastomosis with ICG-infused chitosan films. 1–3. IEEE.

Ruijgrok, P. V., Verhart, N. R., Zijlstra, P., Tchebotareva, A. L., & Orrit, M. (2011). Brownian Fluctuations and Heating of an Optically Aligned Gold Nanorod. Physical Review Letters, 107(3), 037401. https://doi.org/10.1103/PhysRevLett.107.037401

Rylander, M. N., Feng, Y., Bass, J., & Diller, K. R. (2007). Heat shock protein expression and injury optimization for laser therapy design. Lasers in Surgery and Medicine, 39(9), 731–746. https://doi.org/10.1002/lsm.20546

Sadoskas, D., Suder, N. C., & Wukich, D. K. (2016). Perioperative glycemic control and the effect on surgical site infections in diabetic patients undergoing foot and ankle surgery. Foot & Ankle Specialist, 9(1), 24–30.

Sahni, D., Jea, A., Mata, J. A., Marcano, D. C., Sivaganesan, A., Berlin, J. M., … Tour, J. M. (2013). Biocompatibility of pristine graphene for neuronal interface Laboratory investigation. Journal of Neurosurgery-Pediatrics, 11(5), 575–583. https://doi.org/10.3171/2013.1.PEDS12374

Salah, E., Bakr, M., Kamel, H., & Abdel, K. (2010). Patent No. US Patent WO 2010034219 A1.

Savage, H. E., Halder, R. K., Kartazayeu, U., Rosen, R. B., Gayen, T., McCormick, S. A., … Alfano, R. R. (2004). NIR laser tissue welding of in vitro porcine cornea and sclera tissue. Lasers in Surgery and Medicine, 35(4), 293–303. https://doi.org/10.1002/lsm.20094

Savage, Howard E., Halder, R. K., Kartazayeu, U., Rosen, R. B., Gayen, T., McCormick, S. A., … Alfano, R. R. (2004). NIR laser tissue welding of in vitro porcine cornea and sclera tissue. Lasers in Surgery and Medicine, 35(4), 293–303. https://doi.org/10.1002/lsm.20094

Schalow, E. L., & Kirsch, A. J. (2003). Laser tissue soldering: Applications in the genitourinary system. Current Urology Reports, 4(1), 56–59.

Schnueriger, B., Barmparas, G., Branco, B. C., Lustenberger, T., Inaba, K., & Demetriades, D. (2011). Prevention of postoperative peritoneal adhesions: A review of the literature. American Journal of Surgery, 201(1), 111–121. https://doi.org/10.1016/j.amjsurg.2010.02.008

Schober, R., Ulrich, F., Sander, T., Dürselen, H., & Hessel, S. (1986). Laser-induced alteration of collagen substructure allows microsurgical tissue welding. Science (New York, N.Y.), 232(4756), 1421–1422.

Schober, R., Ulrich, F., Sander, T., Durselen, H., & Hessel, S. (1986). Laser-Induced Alteration of Collagen Substructure Allows Microsurgical Tissue Welding. Science, 232(4756), 1421–1422. https://doi.org/10.1126/science.3715454

Schrand, A. M., Stacy, B. M., Payne, S., Dosser, L., & Hussain, S. M. (2011). Fundamental Examination of Nanoparticle Heating Kinetics Upon Near Infrared (NIR) Irradiation. ACS Applied Materials & Interfaces, 3(10), 3971–3980. https://doi.org/10.1021/am2008536

Seiler, C. M., Bruckner, T., Diener, M. K., Papyan, A., Golcher, H., Seidlmayer, C., … Knaebel, H.-P. (2009). Interrupted or continuous slowly absorbable sutures for closure of primary elective midline abdominal incisions: A multicenter randomized trial (INSECT: ISRCTN24023541). Annals of Surgery, 249(4), 576–582.

Shao, J., Xuan, M., Dai, L., Si, T., Li, J., & He, Q. (2015). Near-Infrared-Activated Nanocalorifiers in Microcapsules: Vapor Bubble Generation for In Vivo Enhanced Cancer Therapy. Angewandte Chemie-International Edition, 54(43), 12782–12787. https://doi.org/10.1002/anie.201506115

Sharifi, S., Behzadi, S., Laurent, S., Forrest, M. L., Stroeve, P., & Mahmoudi, M. (2012). Toxicity of nanomaterials. Chemical Society Reviews, 41(6), 2323–2343. https://doi.org/10.1039/C1CS15188F

Sheffy, N., Mintz, Y., Rivkind, A., & Shapira, S. (2006). Terror-Related Injuries: A Comparison of Gunshot Wounds Versus Secondary-Fragments—Induced Injuries from Explosives. Journal of the American College of Surgeons, 203(3), 297–303. https://doi.org/10.1016/j.jamcollsurg.2006.05.010

Shen, F., Zhu, Y., Li, X., Luo, R., Tu, Q., Wang, J., & Huang, N. (2015). Vascular cell responses to ECM produced by smooth muscle cells on TiO2 nanotubes. Applied Surface Science, 349, 589–598. https://doi.org/10.1016/j.apsusc.2015.05.042

Shevach, M., Maoz, B. M., Feiner, R., Shapira, A., & Dvir, T. (2013). Nanoengineering gold particle composite fibers for cardiac tissue engineering. Journal of Materials Chemistry B, 1(39), 5210–5217. https://doi.org/10.1039/c3tb20584c

Shoulders, M. D., & Raines, R. T. (2009a). Collagen Structure and Stability. Annual Review of Biochemistry, 78(1), 929–958. https://doi.org/10.1146/annurev.biochem.77.032207.120833

Shumalinsky, D., & Lobik, L. (2004). Laparoscopic laser soldering for repair of ureteropelvic junction obstruction in the porcine model. Journal of ….

Simhon, D., Halpern, M., Brosh, T., Vasilyev, T., Kariv, N., Argaman, R., … Nevo, Z. (2004, July). <title>In vivo laser soldering of incisions in juvenile pig skins using GaAs or CO<formula><inf><roman>2</roman></inf></formula> lasers and a temperature control system</title> (K. E. Bartels, L. S. Bass, W. T. W. de Riese, K. W. Gregory, H. Hirschberg, A. Katzir, … B. J. Wong, Eds.). https://doi.org/10.1117/12.528948

Singer, A. J., Quinn, J. V., & Hollander, J. E. (2008). The cyanoacrylate topical skin adhesives. American Journal of Emergency Medicine, 26(4), 490–496. https://doi.org/10.1016/j.ajem.2007.05.015

Slade Shantz, J. A., Vernon, J., Morshed, S., Leiter, J., & Stranges, G. (2013). Sutures versus staples for wound closure in orthopaedic surgery: A pilot randomized controlled trial. Patient Safety in Surgery, 7, 6. https://doi.org/10.1186/1754-9493-7-6

Small IV, W., Da Silva, L. B., & Matthews, D. L. (1998). Spectroscopic study of the effect of laser heating on collagen stability: Implications for tissue welding. 276–281. International Society for Optics and Photonics.

Soenen, S. J., Rivera-Gil, P., Montenegro, J.-M., Parak, W. J., De Smedt, S. C., & Braeckmans, K. (2011). Cellular toxicity of inorganic nanoparticles: Common aspects and guidelines for improved nanotoxicity evaluation. Nano Today, 6(5), 446–465. https://doi.org/10.1016/j.nantod.2011.08.001

Solhpour, S., Weldon, E., Foster, T., & Anderson, R. (1994). 'Mechanism of thermal tissue welding (Part 1). Lasers Surg. Med. Suppl.

Sorg, B. S., & Welch, A. J. (2003). Preliminary biocompatibility experiment of polymer films for laser-assisted tissue welding. Lasers in Surgery and Medicine, 32(3), 215–223. https://doi.org/10.1002/lsm.10156

Spector, D., Rabi, Y., Vasserman, I., Hardy, A., Klausner, J., Rabau, M., & Katzir, A. (2009). In vitro large diameter bowel anastomosis using a temperature controlled laser tissue soldering system and albumin stent. Lasers in Surgery and Medicine, 41(7), 504–508. https://doi.org/10.1002/lsm.20799

Spence, G. T., Hartland, G. V., & Smith, B. D. (2013). Activated photothermal heating using croconaine dyes. Chemical Science, 4(11), 4240. https://doi.org/10.1039/c3sc51978c

Sriramoju, V., & Alfano, R. R. (2011a). Management of heat in laser tissue welding using NIR cover window material. Lasers in Surgery and Medicine, 43(10), 991–997. https://doi.org/10.1002/lsm.21143

Sriramoju, V., & Alfano, R. R. (2012a). Laser tissue welding analyzed using fluorescence, Stokes shift spectroscopy, and Huang-Rhys parameter. Journal of Biophotonics, 5(2), 185–193. https://doi.org/10.1002/jbio.201100050

Steinstraesser, L., Wehner, M., Trust, G., Sorkin, M., Bao, D., Hirsch, T., … Jacobsen, F. (2010a). Laser-mediated fixation of collagen-based scaffolds to dermal wounds. Lasers in Surgery and Medicine, 42(2), 141–149. https://doi.org/10.1002/lsm.20901

Sun, L., Yi, S., Wang, Y., Pan, K., Zhong, Q., & Zhang, M. (2014). A bio-inspired approach for in situ synthesis of tunable adhesive. Bioinspiration & Biomimetics, 9(1), 016005. https://doi.org/10.1088/1748-3182/9/1/016005

Tabakoğlu, H. Ö., & Gülsoy, M. (2010). In vivo comparison of near infrared lasers for skin welding. Lasers in Medical Science, 25(3), 411–421. https://doi.org/10.1007/s10103-009-0739-3

Tajirian, A. L., & Goldberg, D. J. (2010a). A review of sutures and other skin closure materials. Journal of Cosmetic and Laser Therapy, 12(6), 296–302. https://doi.org/10.3109/14764172.2010.538413

Tao, H., Kaplan, D. L., & Omenetto, F. G. (2012). Silk Materials—A Road to Sustainable High Technology. Advanced Materials, 24(21), 2824–2837. https://doi.org/10.1002/adma.201104477

Thiesen, B., & Jordan, A. (2008). Clinical applications of magnetic nanoparticles for hyperthermia. International Journal of Hyperthermia, 24(6), 467–474. https://doi.org/10.1080/02656730802104757

Thomsen, S. (1991). Pathologic analysis of photothermal and photomechanical effects of laser–tissue interactions. Photochemistry and Photobiology.

Thurber, A. E., Omenetto, F. G., & Kaplan, D. L. (2015). In Vivo Bioresponses to Silk Proteins. Biomaterials, 71, 145–157. https://doi.org/10.1016/j.biomaterials.2015.08.039

Tucker, C. L., Jones, J. A., Bringhurst, H. N., Copeland, C. G., Addison, J. B., Weber, W. S., … Lewis, R. V. (2014). Mechanical and Physical Properties of Recombinant Spider Silk Films Using Organic and Aqueous Solvents. Biomacromolecules, 15(8), 3158–3170. https://doi.org/10.1021/bm5007823

Urie, R., Flake, T., & Rege, K. (2017). Laser Tissue Welding in Wound Healing and Surgical Repair. In Bioengineering In Wound Healing: A Systems Approach (pp. 303–324). World Scientific.

Urie, R., Guo, C., Ghosh, D., Thelakkaden, M., Wong, V., Lee, J. K., … Rege, K. (2018). Rapid Soft Tissue Approximation and Repair Using Laser-Activated Silk Nanosealants. Advanced Functional Materials, 28(42), 1802874.

Urie, R., Quraishi, S., Jaffe, M., & Rege, K. (2015a). Gold Nanorod-Collagen Nanocomposites as Photothermal Nanosolders for Laser Welding of Ruptured Porcine Intestines. ACS Biomaterials Science & Engineering, 1(9), 805–815. https://doi.org/10.1021/acsbiomaterials.5b00174

Urie, R., & Rege, K. (2015). Nanoscale inorganic scaffolds as therapeutics and delivery vehicles. Current Opinion in Chemical Engineering, 7, 120–128.

Utech, S., & Boccaccini, A. R. (2016). A review of hydrogel-based composites for biomedical applications: Enhancement of hydrogel properties by addition of rigid inorganic fillers. Journal of Materials Science, 51(1), 271–310. https://doi.org/10.1007/s10853-015-9382-5
Vancomycin (Vancocyn, Lyphocin) | The Antimicrobial Index Knowledgebase—TOKU-E. (n.d.). Retrieved September 26, 2019, from http://antibiotics.toku-e.com/antimicrobial_1182_1.html

Voge, C. M., & Stegemann, J. P. (2011). Carbon nanotubes in neural interfacing applications. Journal of Neural Engineering, 8(1), 011001. https://doi.org/10.1088/1741-2560/8/1/011001

Wadia, Y., Xie, H., & Kajitani, M. (2000). Liver repair and hemorrhage control by using laser soldering of liquid albumin in a porcine model. Lasers in Surgery and Medicine, 27(4), 319–328. https://doi.org/10.1002/1096-9101(2000)27:4<319::AID-LSM4>3.0.CO;2-G

Wang, S., Wang, X., Draenert, F. G., Albert, O., Schroeder, H. C., Mailaender, V., … Mueller, W. E. G. (2014). Bioactive and biodegradable silica biomaterial for bone regeneration. Bone, 67, 292–304. https://doi.org/10.1016/j.bone.2014.07.025

Wang, Y.-X. J. (2015). Current status of superparamagnetic iron oxide contrast agents for liver magnetic resonance imaging. World Journal of Gastroenterology, 21(47), 13400–13402. https://doi.org/10.3748/wjg.v21.i47.13400

Weissleder, R. (2001). A clearer vision for in vivo imaging. Nature Publishing Group.

Welch, A. J. (1984). The Thermal Response of Laser Irradiated Tissue. IEEE Journal of Quantum Electronics, 20(12), 1471–1481. https://doi.org/10.1109/JQE.1984.1072339

Wenzel, G. I., Anvari, B., Mazhar, A., Pikkula, B., & Oghalai, J. S. (2007). Laser-induced collagen remodeling and deposition within the basilar membrane of the mouse cochlea. Journal of Biomedical Optics, 12(2), 021007. https://doi.org/10.1117/1.2714286

Whelove, O. E., Cozad, M. J., Lee, B.-D., Sengupta, S., Bachman, S. L., Ramshaw, B. J., & Grant, S. A. (2011). Development and in vitro studies of a polyethylene terephthalate-gold nanoparticle scaffold for improved biocompatibility. Journal of Biomedical Materials Research Part B-Applied Biomaterials, 99B(1), 142–149. https://doi.org/10.1002/jbm.b.31881

Wick, E. C., Shore, A. D., Hirose, K., Ibrahim, A. M., Gearhart, S. L., Efron, J., … Makary, M. A. (2011). Readmission Rates and Cost Following Colorectal Surgery. Diseases of the Colon & Rectum, 54(12), 1475. https://doi.org/10.1097/DCR.0b013e31822ff8f0

Wolf -de Jonge, I. C. D. Y. M., Beek, J. F., & Balm, R. (2004a). 25 Years of Laser Assisted Vascular Anastomosis (LAVA): What Have We Learned? European Journal of Vascular and Endovascular Surgery, 27(5), 466–476. https://doi.org/10.1016/j.ejvs.2004.02.021

Wukich, D. K., McMillen, R. L., Lowery, N. J., & Frykberg, R. G. (2011). Surgical site infections after foot and ankle surgery: A comparison of patients with and without diabetes. Diabetes Care, 34(10), 2211–2213.

Xie, H., Bendre, S. C., Burke, A. P., Gregory, K. W., & Furnary, A. P. (2004). Laser-assisted vascular end to end anastomosis of elastin heterograft to carotid artery with an albumin stent: A preliminary in vivo study. Lasers in Surgery and Medicine, 35(3), 201–205. https://doi.org/10.1002/lsm.20092

Xuan, M., Wu, Z., Shao, J., Dai, L., Si, T., & He, Q. (2016). Near infrared light-powered Janus mesoporous silica nanoparticle motors. Journal of the American Chemical Society, 138(20), 6492–6497.

Yang, P., Yao, M., DeMartelaere, S. L., Redmond, R. W., & Kochevar, I. E. (2012). Light-activated sutureless closure of wounds in thin skin. Lasers in Surgery and Medicine, 44(2), 163–167. https://doi.org/10.1002/lsm.21137

Yang, Y., & Kaufman, L. J. (2009). Rheology and Confocal Reflectance Microscopy as Probes of Mechanical Properties and Structure during Collagen and Collagen/Hyaluronan Self-Assembly. Biophysical Journal, 96(4), 1566–1585. https://doi.org/10.1016/j.bpj.2008.10.063

Ye, D., Zhong, Z., Xu, H., Chang, C., Yang, Z., Wang, Y., … Zhang, L. (2016). Construction of cellulose/nanosilver sponge materials and their antibacterial activities for infected wounds healing. Cellulose, 23(1), 749–763. https://doi.org/10.1007/s10570-015-0851-4

Yee, W., Seluaduray, G., & Hawkins, B. (2016). Characterization of silver nanoparticle-infused tissue adhesive for ophthalmic use. Journal of the Mechanical Behavior of Biomedical Materials, 55, 67–74. https://doi.org/10.1016/j.jmbbm.2015.10.011

Yeung, A. M., Faraj, L. A., McIntosh, O. D., Dhillon, V. K., & Dua, H. S. (2016). Fibrin glue inhibits migration of ocular surface epithelial cells. Eye, 30(10), 1389.

Yucel, T., Lovett, M. L., Giangregorio, R., Coonahan, E., & Kaplan, D. L. (2014). Silk fibroin rods for sustained delivery of breast cancer therapeutics. Biomaterials, 35(30), 8613–8620. https://doi.org/10.1016/j.biomaterials.2014.06.030

Yucel, T., Lovett, M. L., & Keplan, D. L. (2014). Silk-based biomaterials for sustained drug delivery. Journal of Controlled Release, 190, 381–397. https://doi.org/10.1016/j.jconrel.2014.05.059

Zaja-Milatovic, S., & Richmond, A. (2008). CXC chemokines and their receptors: A case for a significant biological role in cutaneous wound healing. Histology and Histopathology, 23(11), 1399–1407.

Zeng, R., Dietzel, W., Witte, F., Hort, N., & Blawert, C. (2008). Progress and challenge for magnesium alloys as biomaterials. Advanced Engineering Materials, 10(8), B3–B14. https://doi.org/10.1002/adem.200800035

Zhang, Q., Li, N., Goebl, J., Lu, Z., & Yin, Y. (2011). A systematic study of the synthesis of silver nanoplates: Is citrate a "magic" reagent? Journal of the American Chemical Society, 133(46), 18931–18939.

Zhang, S., Liu, X., Wang, H., Peng, J., & Wong, K. K. Y. (2014). Silver nanoparticle-coated suture effectively reduces inflammation and improves mechanical strength at intestinal anastomosis in mice. Journal of Pediatric Surgery, 49(4), 606–613. https://doi.org/10.1016/j.jpedsurg.2013.12.012

Zhang, W., Wray, L. S., Rnjak-Kovacina, J., Xu, L., Zou, D., Wang, S., … Jiang, X. (2015). Vascularization of hollow channel-modified porous silk scaffolds with endothelial cells for tissue regeneration. Biomaterials, 56, 68–77. https://doi.org/10.1016/j.biomaterials.2015.03.053

Zhang, X., Reagan, M. R., & Kaplan, D. L. (2009). Electrospun silk biomaterial scaffolds for regenerative medicine. Advanced Drug Delivery Reviews, 61(12), 988–1006. https://doi.org/10.1016/j.addr.2009.07.005

Zhou, J., Chen, J. K., & Zhang, Y. (2009). Dual-phase lag effects on thermal damage to biological tissues caused by laser irradiation. Computers in Biology and Medicine, 39(3), 286–293. https://doi.org/10.1016/j.compbiomed.2009.01.002

Zhou, J., Zhang, Y., & Chen, J. K. (2008). Non-Fourier Heat Conduction Effect on Laser-Induced Thermal Damage in Biological Tissues. Numerical Heat Transfer, Part A: Applications, 54(1), 1–19. https://doi.org/10.1080/10407780802025911

Züger, B. j., Ott, B., Mainil-Varlet, P., Schaffner, Th., Clémence, J.-F., Weber, H. p., & Frenz, M. (2001). Laser solder welding of articular cartilage: Tensile strength and chondrocyte viability. Lasers in Surgery and Medicine, 28(5), 427–434. https://doi.org/10.1002/lsm.1070

APPENDIX I

SUPPORTING INFORMATION FOR CHAPTER TWO
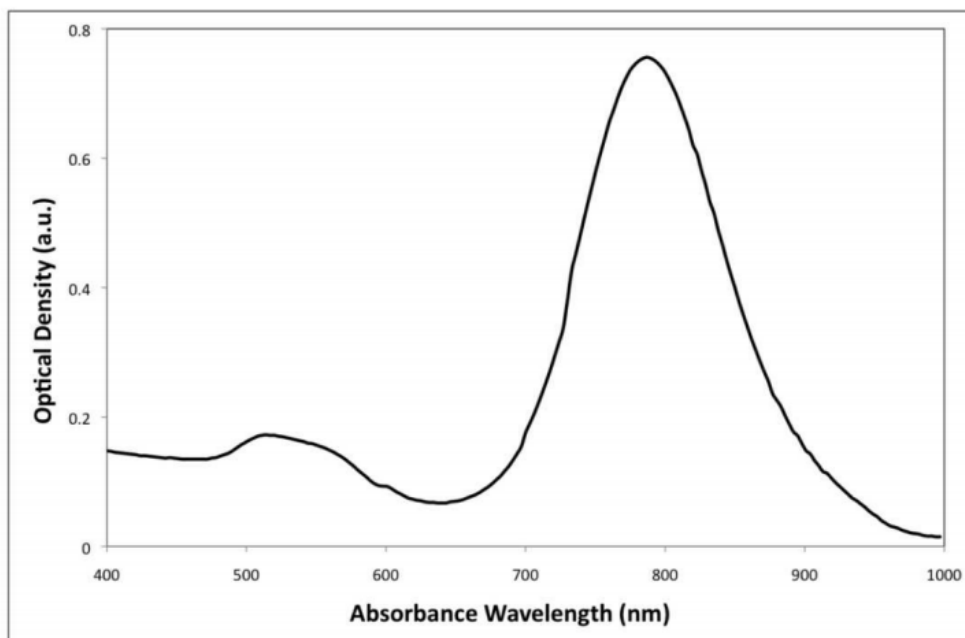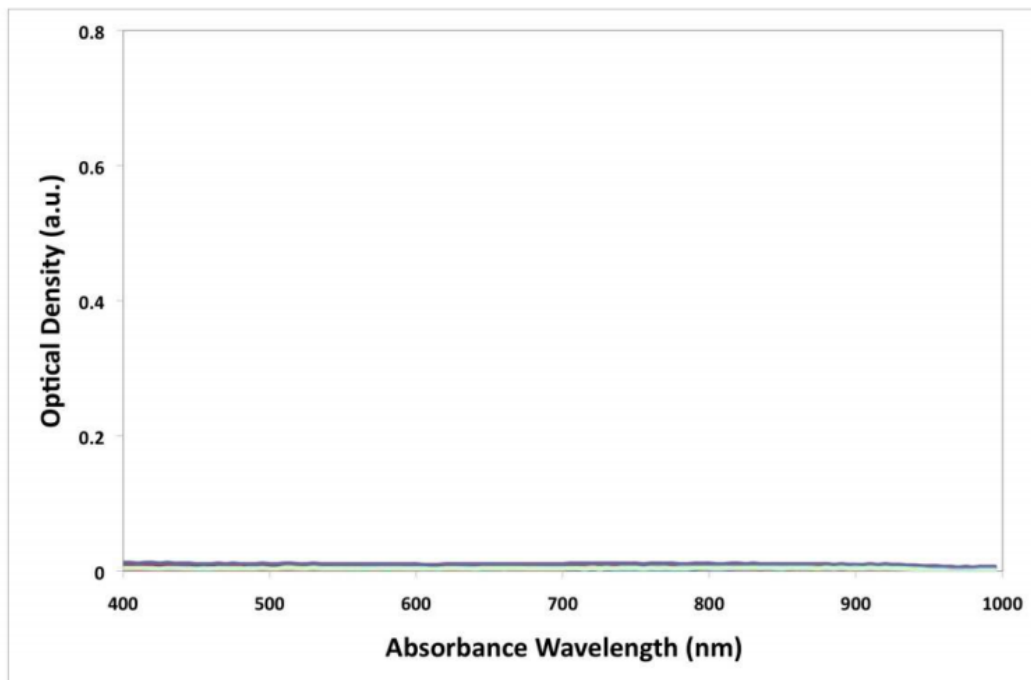
Figure S2.1. Representative absorbance spectrum of gold nanorod dispersions. Gold nanorods tuned to maximum absorbance at 800 nm.
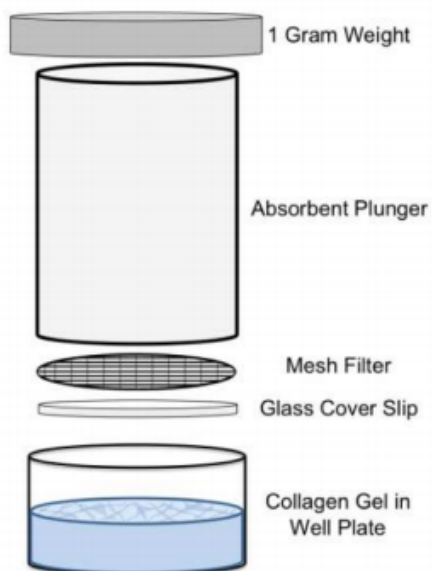
Figure S2.2. Illustration of plastic compression device. An absorbent plunger simultaneously compresses the hydrogels and absorbs excess fluid from the gels.

Figure S2.3. Depiction of leak and burst pressure testing device. Bifurcated tubing from a syringe leads to a digital manometer and a needle. The needle is inserted into clamped intestine and filled with saline solution. Simultaneously, the pressure is recorded when leakage first occurs from the intestine (leak pressure) and at the maximum pressure reached (burst pressure).

Figure S2.4. Representative absorbance spectrum of supernatant in gold nanorod leaching experiments. Gold nanorods tuned to maximum absorbance at 800 nm. As shown, GNR-collagen nanocomposites show no leaching based on lack of absorbance peak at 800 nm
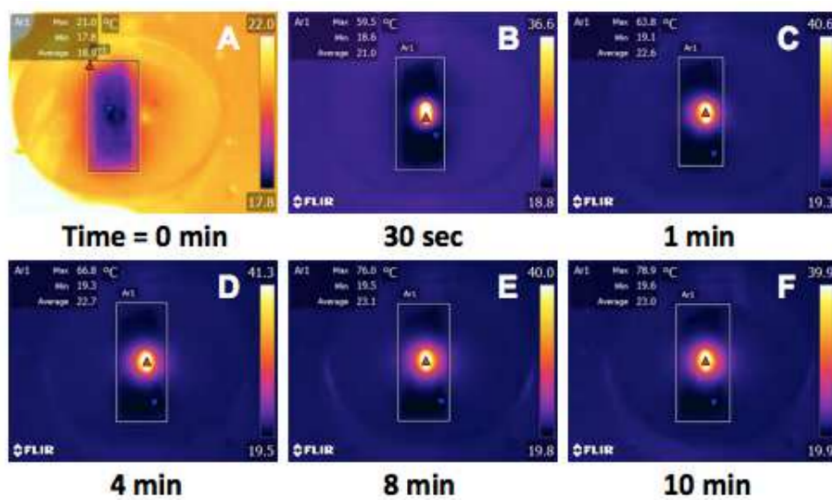
Figure S2.5. Near-infrared images of nanocomposite placed over intact intestine. A-F show temperature profiles of the tissue and nanocomposite surface from 0 to 10 minutes of pulsed wave laser radiation at 2.00 W/cm^2. The blue inverted triangles pinpoint the location

of the minimum temperature, and the red triangles indicate the maximum temperature of the area measured. The rate of increase in temperature greatly decreases over time. These images are representative of n=5 independent experiments at these conditions.
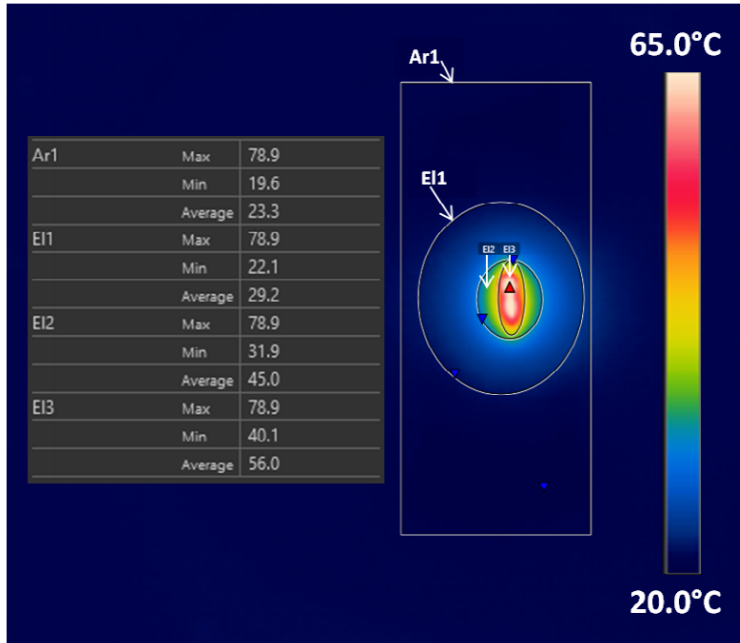
Figure S2.6. Detailed infrared image of nanocomposite placed over intact tissue surface from Figure S5F. This detailed image of Figure S5F was captured at 10 minutes of 2.00 W/cm^2 pulsed wave laser radiation. Area Ar1 represents the area of the tissue (50 mm x 20 mm). El1 indicates the area where the temperature has been significantly raised. El2 highlights the approximate location of the nanocomposite (8 mm diameter), and El3 represents the approximate area of exposure of the laser (2mm x 10 mm). Inverted blue triangles represent the minimum temperature in the enclosed area, and the red triangle indicates the maximum temperature in the enclosed areas. Image has been modified to clarify each region.
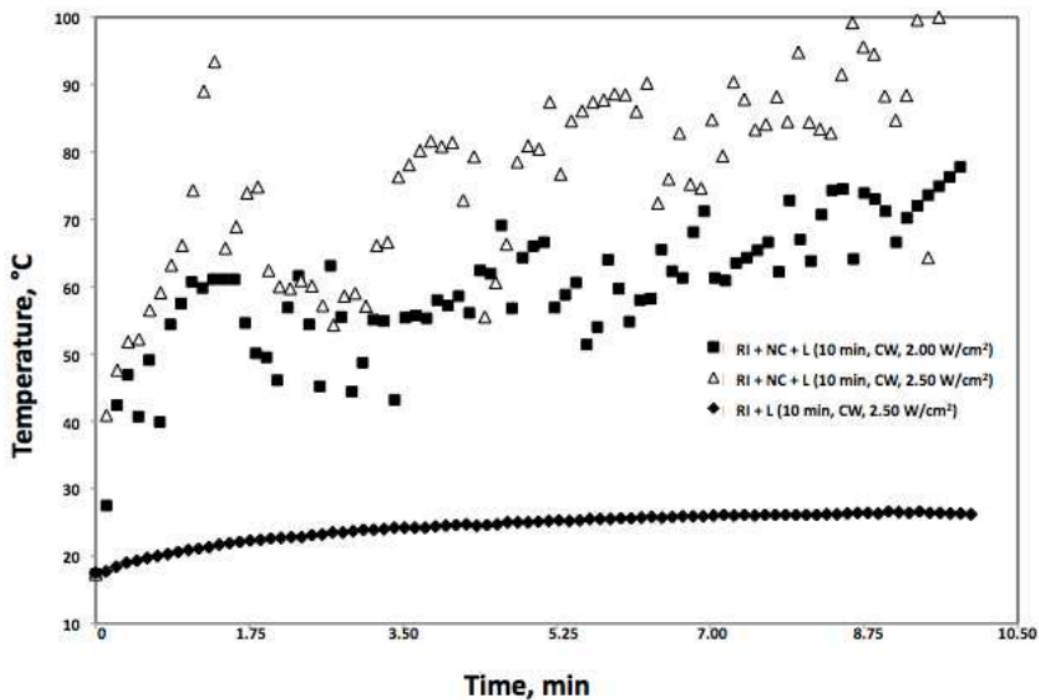
Figure S2.7. Maximum nanocomposite surface temperature during laser tissue welding procedure. Dried nanocomposites (NC) placed over intestinal tissue and irradiated at 2.00 (squares) or 2.50 (triangles) W/cm^2 for 10 minutes were measured for maximum surface temperature using IR images. In addition, the surface temperature profile of ruptured intestine (RI) alone irradiated at 2.50 W/cm^2 in absence of collagen-GNR nanocomposite is shown. Representative curves of n=5 independent experiments.

APPENDIX II

SUPPORTING INFORMATION FOR CHAPTER FOUR

Table 4.1. FTIR band assignment of silk materials.

Wavenumber (cm⁻¹)	Assignment	
	Band	Conformation
1698	Amide I, C=O stretching, C-N stretching	β-sheet
1645	Amide I, C=O stretching, C-N stretching	Amorphous
1622	Amide I, C=O stretching, C-N stretching	β-sheet
1531	Amide II, C=O in-plane bending, C-N stretching, N-H in-plane bending	Amorphous
1512	Amide II, C=O in-plane bending, C-N stretching, N-H in-plane bending	β-sheet
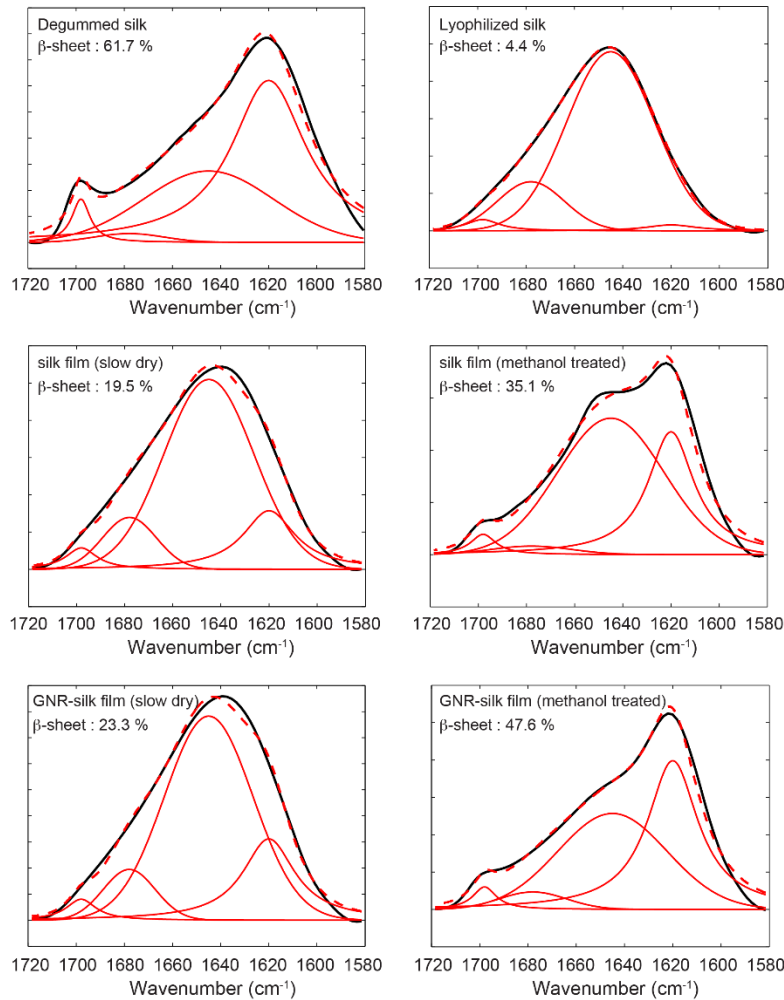
Figure S4.2. Deconvolution of amide I region of FT-IR spectra of silk fibers and silk films. The deconvolution was performed in Matlab with the following peak parameters for different conformations: 1698 cm-1 (Lorentzian, β-sheet), 1678 cm-1 (Gaussian,

amorphous), 1645 cm-1 (Gaussian, amorphous), and 1620 cm-1 (Lorentzian, β-sheet). It has been demonstrated in previous research that fitting with Lorentzian peak for β-sheet conformation and Gaussian peak for amorphous conformation shows best fitting results.[1]
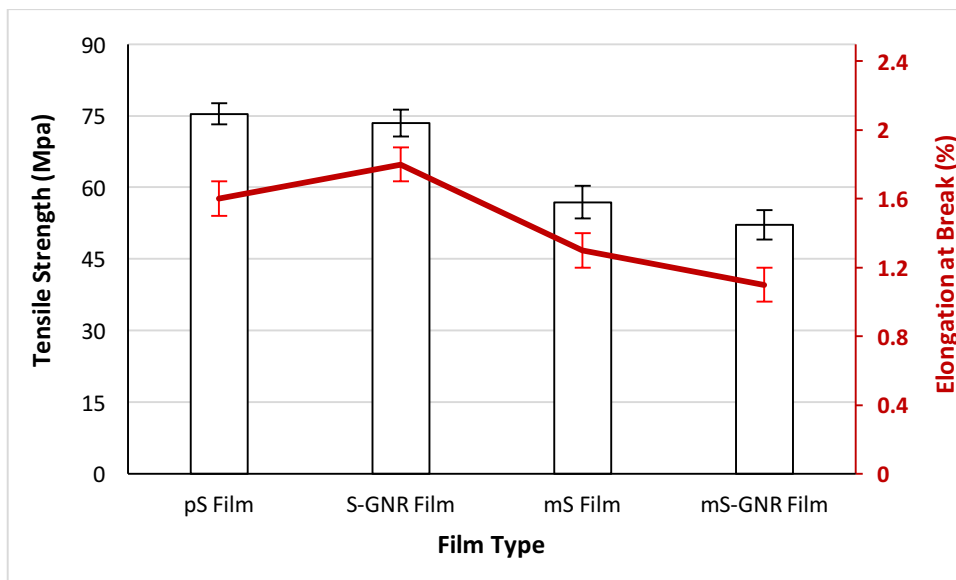

Figure S4.3. Tensile Strength of Silk Films and Elongation at Break.

To measure mechanical strength, the silk films were patched on a paper frame and mounted on an ElectroPuls E3000 (Instron, Norwood, MA). The samples were tested at a crosshead speed of 2 mm/min. Ultimate tensile strength was defined as the maximum stress, and the elongation to failure was the final point before a >10% decrease in load. Untreated films showed greater tensile strength and larger elongation break values than the more brittle methanol-treated films, due to low water content and disordered alignment of secondary conformations from methanol treatment[2].
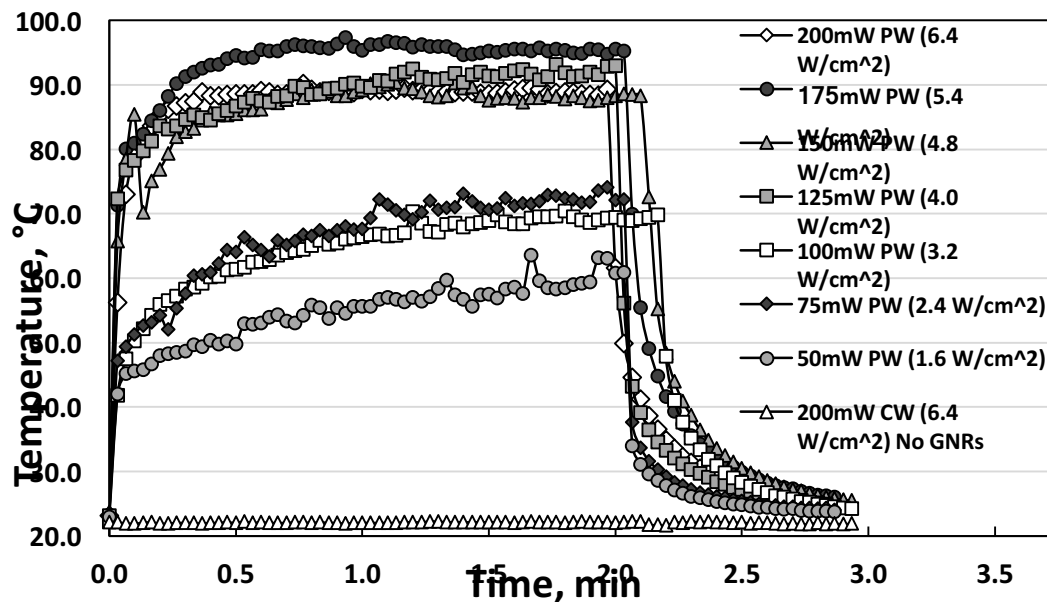
Figure S4.4. Photothermal Response of untreated silk-GNR nanocomposites following irradiation with Pulsed Wave (PW) laser. Silk-GNR nanocomposites (S-GNR) were irradiated for two minutes with a continuous wave (CW) 800 nm laser at power densities ranging from 1.6 to 6.4 W/cm^2. Following approximately two minutes, the laser shutter was closed to allow cooling of the nanocomposites, corresponding with a rapid decrease in surface temperature. The response of silk films without GNRs (PS) to 6.4 W/cm^2 laser is indicated by open triangles. In all cases, the temperature response was determined using images taken by a thermal camera. Curves are representative of n=3 independent experiments.
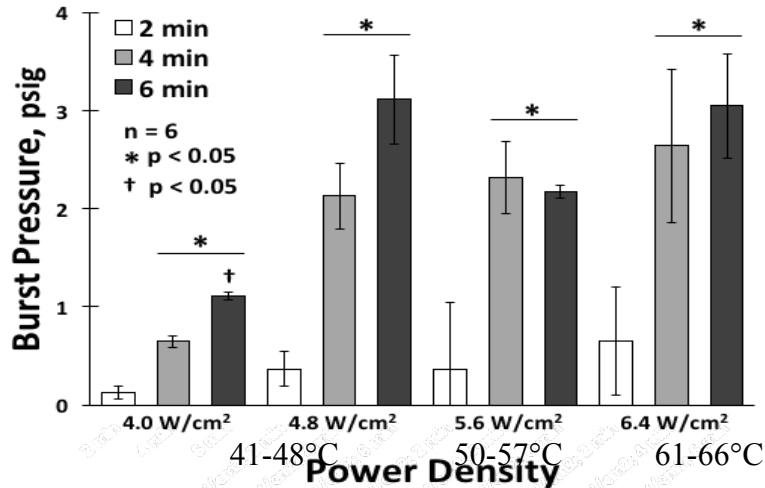
Figure S4.5. Comparison of burst pressure of welded tissue by laser exposure duration and power density. Burst pressure measurements of incised porcine tissue closed by welding at laser treatments or 2, 4, or 6 minutes and power density ranging from 4.0 to 6.4 W/cm^2, where n=6. * indicate that the 4 and 6 min burst pressures are significantly different from the 2 min burst pressure. † indicates that the 6 min burst pressure is significantly different from the 4 min burst pressure.
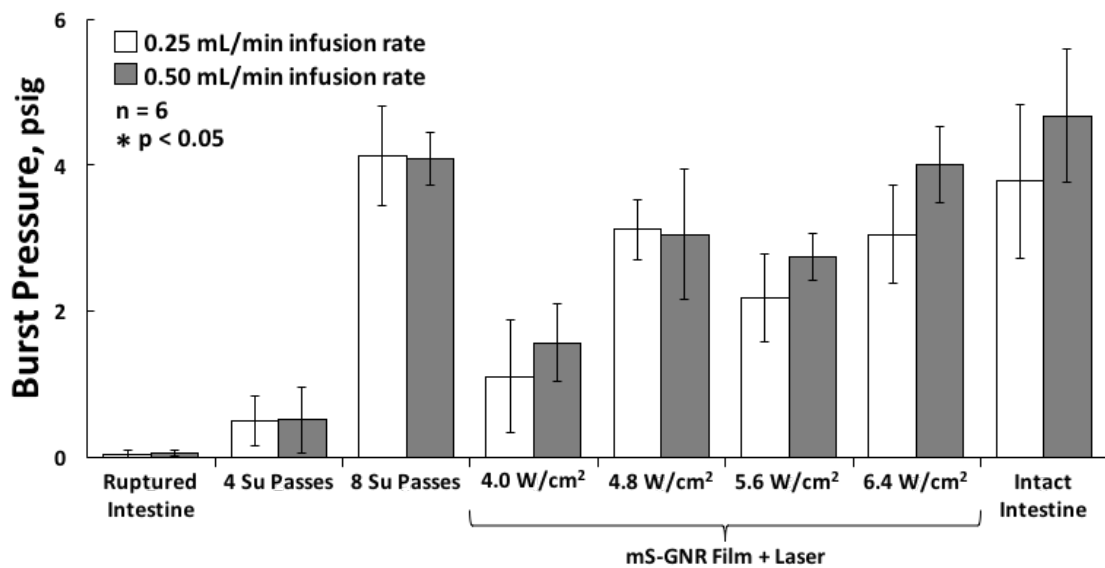
Figure S4.6. Comparison of burst pressure of native and welded tissue at continuous flowrates of 0.25 or 0.5 mL/min where n=6. Porcine cadaver intestine was ruptured. Ruptured samples were then perfused with a dye saline solution or closed via continuous sutures (Su) or laser sealing with mS-GNR films and laser at varying power densities as shown. All laser treatments lasted 6 minutes. For comparison, unruptured (intact) intestine was also perfused until bursting.
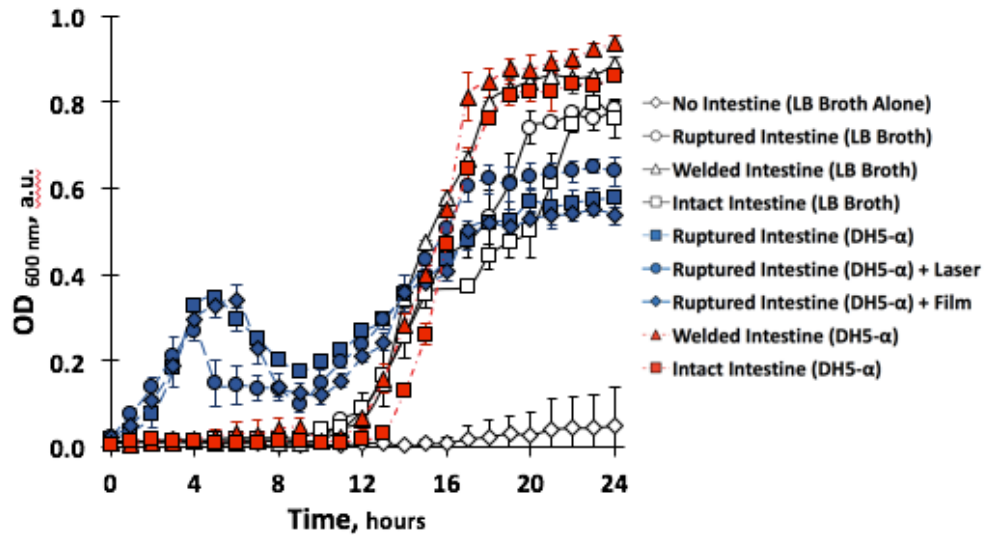

Figure S4.7. Bacterial leakage study over 24 h. After 12 h, bacterial growth is seen even in the case of intact intestine + LB broth (no E.coli added). Please refer main manuscript for details.
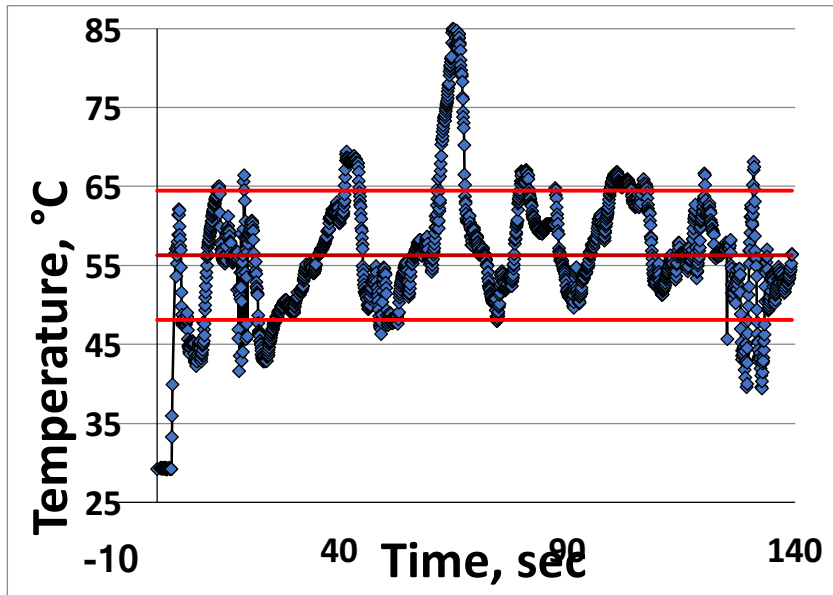
Figure S4.8. Temperature profile following application of laser light along the incision made in the skin of live mice closed with S-GNR nanosealant. The temperature is fairly steady in the window targeted for facilitating tissue sealing and approximation. Please refer main manuscript for details.
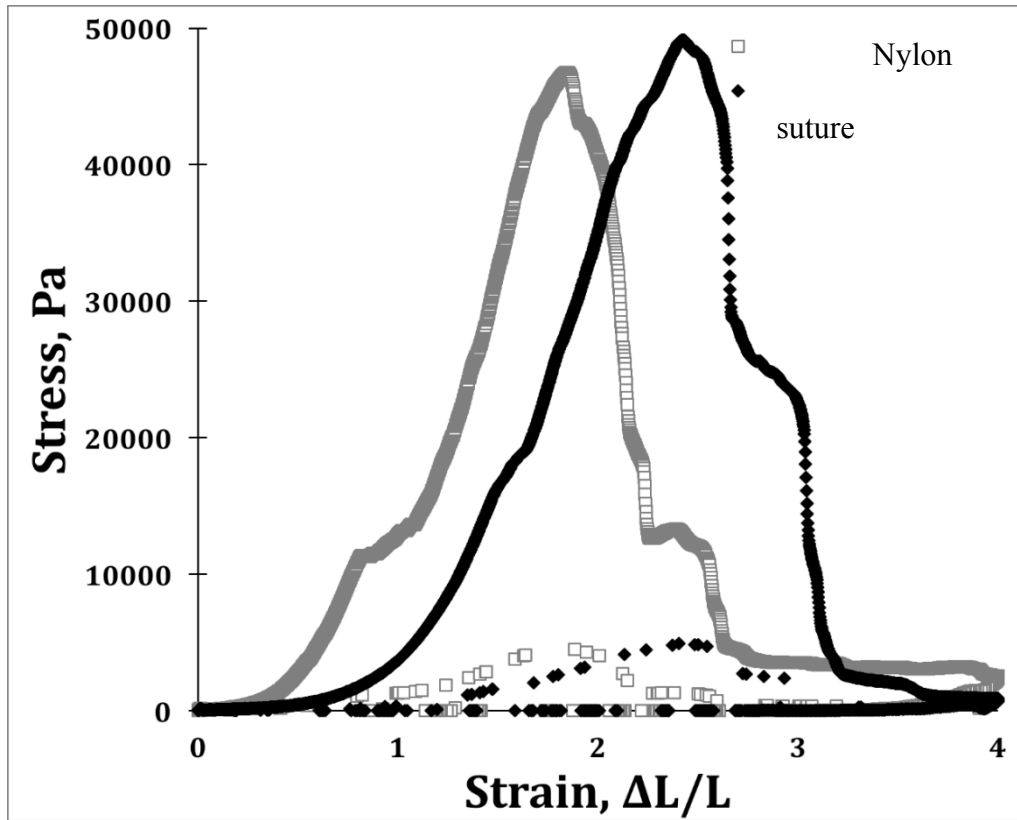
Figure S4.9. Stress-strain curves of skin following approximation with sutures and laser-activated nanosealants. Please refer main manuscript for details.

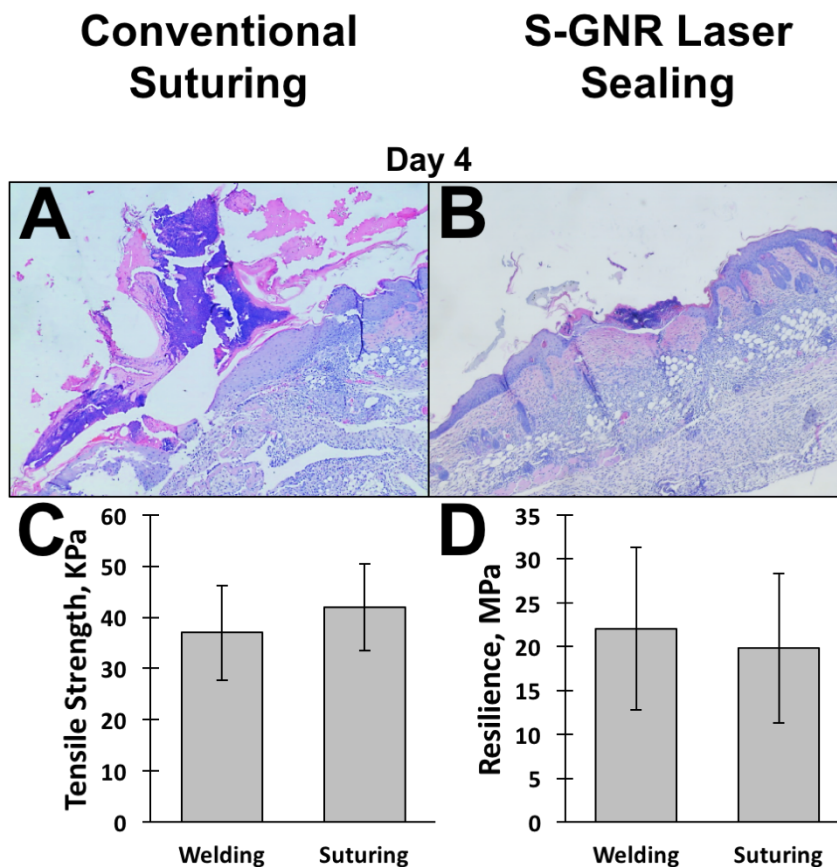**Conventional Suturing** **S-GNR Laser Sealing**

Day 4

Figure S4.10. C57Bl6 Mouse Skin Incision Healing After 4 Days. (A,C) Skin incision closure by commercial silk suture, 4 interrupted knots. (B,D) Incisions are sealed with S-GNR paste and laser at 2 W/cm^2 for 2 min. (A, B) Formalin-fixed tissue sections stained with hematoxylin & eosin. (C) Tensile strength of treated skin incisions two days following surgery. (D) Resilience of treated skin incisions two days following surgery.

REFERENCES

[1]   F. Paquet-Mercier, T. Lefevre, M. Auger, M. Pezolet, *Soft Matter* 2013, 9, 208.

[2]   Q. Lu, X. Hu, X. Wang, J. A. Kluge, S. Lu, P. Cebe, D. L. Kaplan, *Acta biomaterialia* 2010, 6, 1380.